



저작자표시-비영리-변경금지 2.0 대한민국

이용자는 아래의 조건을 따르는 경우에 한하여 자유롭게

- 이 저작물을 복제, 배포, 전송, 전시, 공연 및 방송할 수 있습니다.

다음과 같은 조건을 따라야 합니다:



저작자표시. 귀하는 원저작자를 표시하여야 합니다.



비영리. 귀하는 이 저작물을 영리 목적으로 이용할 수 없습니다.



변경금지. 귀하는 이 저작물을 개작, 변형 또는 가공할 수 없습니다.

- 귀하는, 이 저작물의 재이용이나 배포의 경우, 이 저작물에 적용된 이용허락조건을 명확하게 나타내어야 합니다.
- 저작권자로부터 별도의 허가를 받으면 이러한 조건들은 적용되지 않습니다.

저작권법에 따른 이용자의 권리는 위의 내용에 의하여 영향을 받지 않습니다.

이것은 [이용허락규약\(Legal Code\)](#)을 이해하기 쉽게 요약한 것입니다.

[Disclaimer](#)

공학박사학위논문

Biomimetic scaffold-mediated in situ bone  
remodeling and rapid bone regeneration:  
Whitlockite nanoparticles and biopolymers

골 리모델링 및 급속 골 재생을 위한  
Whitlockite 나노물질과 고분자 기반  
생체모사 지지체에 관한 연구

2018년 2월

서울대학교 대학원  
공과대학 화학생물공학부  
김 환

**Biomimetic scaffold-mediated in situ bone remodeling and rapid bone regeneration: whitlockite nanoparticles and biopolymers**

지도교수 Nathaniel Suk-Yeon Hwang

이 논문을 공과대학 박사학위논문으로 제출함

2018 년 2 월

서울대학교 대학원  
화학생물공학부  
김 환

김환의 박사학위논문을 인준함  
2018 년 2 월

위원장	김 병 수	
부위원장	Nathaniel Suk-Yeon Hwang	
위원	김 병 기	
위원	남 기 태	
위원	신 흥 수	

**Abstract**

**Biomimetic scaffold-mediated in situ  
bone remodeling and rapid bone  
regeneration: whitlockite nanoparticles  
and biopolymers**

**Hwan Drew Kim**

**School of Chemical and Biological Engineering**

**The Graduate School**

**Seoul National University**

Various strategies have been explored to overcome critically sized bone defects via bone tissue engineering approaches that incorporate biomimetic scaffolds. Biomimetic scaffolds may provide a novel platform for phenotypically stable tissue formation and stem cell

differentiation. In recent years, osteoinductive and inorganic biomimetic scaffold materials have been optimized to offer an osteo-friendly microenvironment for the osteogenic commitment of stem cells. Furthermore, scaffold structures with a microarchitecture design similar to native bone tissue are necessary for successful bone tissue regeneration. For this reason, various methods for fabricating three-dimensional porous structures have been developed. Innovative techniques, such as 3D printing methods, are currently being utilized for optimal host stem cell infiltration, vascularization, nutrient transfer, and stem cell differentiation. In the first part of this dissertation, we will review biomimetic materials and fabrication approaches that are currently being utilized for biomimetic scaffold design. For successful bone tissue regeneration, a variety of materials has been investigated to fabricate the optimal scaffolds. A lot of biocompatible and biodegradable polymers have been explored to make bone scaffold frame, and osteoinductive materials such as metal ions, growth factors have been incorporated to bone scaffolds. Furthermore, various techniques have been developed to construct the three dimensional porous bone scaffolds like natural bone tissue. Those traditional strategies have been innovated

for years, and various cell sources optimized for osteogenesis have been applied to bone tissue engineering. In this way, we expected to overcome current challenges and critical-sized bone defects from accidents and diseases.

In the second part of the thesis, we demonstrate that synthetic whitlockite (WH:  $\text{Ca}_{18}\text{Mg}_2(\text{HPO}_4)_2(\text{PO}_4)_{12}$ ) nanoparticles can recapitulate early-stage of bone regeneration through stimulating osteogenic differentiation, prohibiting osteoclastic activity, and transforming into mechanically enhanced hydroxyapatite (HAP)-neo bone tissues by continuous supply of  $\text{PO}_4^{3-}$  and  $\text{Mg}^{2+}$  under physiological conditions. In addition, based on their structural analysis, the dynamic phase transformation from WH into HAP contributed as a key factor for rapid bone regeneration with denser hierarchical neo-bone structure. Our findings suggest a groundbreaking concept of 'living bone minerals' that actively communicate with the surrounding system to induce self-healing, while previous notions about bone minerals have been limited to passive products of cellular mineralization.

In the third part of the thesis, we fabricated methacrylated PEGDA/CS-based hydrogels with varying CS concentration and

investigated them as biomineralizing three-dimensional scaffolds for charged ion binding and depositions. Due to its negative charge from the sulfate group, CS exhibited an osteogenically favorable microenvironment by binding charged ions such as calcium and phosphate. Particularly, ion binding and distribution within negatively charged hydrogel was dependent on CS concentration. Furthermore, CS dependent biomineralizing microenvironment induced osteogenic differentiation of human tonsil-derived mesenchymal stem cells *in vitro*. This PEGDA/CS-based biomineralizing hydrogel platform can be utilized for in situ bone formation in addition to being an investigational tool for *in vivo* bone mineralization and resorption mechanisms.

In the last part of the thesis, our aim is to explore the potential use of human vascular endothelial growth factors (hVEGF) and Whitlockite (WH) for bone tissue engineering. Various strategies have been explored to stimulate a new bone formation. Among these strategies, includes using angiogenic stimulants in combination with inorganic biomaterials. Neovascularization during the neo-bone formation provides nutrients along with bone forming minerals. Therefore, it is crucial to design a bone stimulating microenvironment composed of both

pro-angiogenic and osteogenic factors. In this respect, hVEGF have been shown to promote blood vessel formation and bone formation. In this study, we demonstrated that hVEGF and WH synergistically stimulated osteogenic commitment of mesenchymal stem cells both *in vitro* and *in vivo*.

Biomimetic scaffold-mediated in situ bone remodeling and rapid bone regeneration in this thesis will be useful to understand the mechanism and the role of biomineral and biopolymer in the bone regeneration system. We believe that this study will directly contribute to make more bone-like scaffold or implants and provide inspiration and foundation knowledge to the other various research fields.

**Keywords: Hydrogel, Whitlockite, Hydroxyapatite, Chondroitin Sulfate, Bone Tissue Engineering**

***Student Number: 2014-31087***

# Table of Contents

<b>Abstract.....</b>	<b>i</b>
<b>Table of Contents .....</b>	<b>vi</b>
<b>List of Table.....</b>	<b>xi</b>
<b>List of Figures.....</b>	<b>xii</b>
<b>Chapter 1. The scientific background and research progress .....</b>	<b>1</b>
1.1 Overview.....	1
1.2 Current state of synthetic inorganic materials for bone tissue engineering scaffold.....	7
1.2.1 Hydroxyapatite (HA) .....	8
1.2.2 Beta-tricalcium phosphate ( $\beta$ -TCP) .....	10
1.2.3 Whitlockite.....	14
1.2.4 Bioglass .....	16
1.3 Synthetic scaffolds for bone tissue engineering.....	19
1.3.1 Composite scaffolds based on calcium phosphate synthetic inorganic materials .....	19
1.3.2 Injectable composite hydrogels based on calcium phosphate synthetic organic materials.....	23
1.4 Fabricating method for complex macroporous bone like structure for increased vascularization.....	36
1.4.1 Salt-leaching methods .....	38
1.4.2 Gas-forming methods.....	39

1.4.3 3D-printing methods .....	42
1.4.4 Lyophilization methods.....	46
1.4.5 Electrospinning methods.....	47
1.4.6 Biomimetic scaffold fabrication approaches.....	48
1.5 Combined effects of growth factors and scaffolds design for bone regeneration.....	53
1.6 Cell sources .....	57
1.7 Summary .....	62

**Chapter 2. Biomimetic whitlockite inorganic nanoparticles-mediated in situ remodeling and rapid bone regeneration ..... 63**

2.1 Introduction.....	63
2.2 Materials and methods .....	66
2.2.1 Material preparation.....	66
2.2.2 Scaffold fabrication.....	67
2.2.3 Material characterization.....	68
2.2.4 Crystal morphology reconstruction.....	69
2.2.5 Ion release measurement.....	70
2.2.6 Zeta potential analysis.....	70
2.2.7 Protein adsorption analysis .....	72
2.2.8 Cell culture.....	72
2.2.9 Immunostaining .....	74
2.2.10 Cell viability and proliferation.....	75
2.2.11 Chemical staining.....	75
2.2.12 SiRNA transfection .....	76

2.2.13 Gene expression profile .....	77
2.2.14 Western blot assay.....	82
2.2.15 Scanning electron microscopy .....	83
2.2.16 Scaffold fabrication.....	83
2.2.17 Mechanical properties of scaffolds .....	86
2.2.18 Ethics statement .....	86
2.2.19 Mechanical properties of scaffolds .....	89
2.2.20 Micro-computed tomography (Micro-CT).....	90
2.2.21 Histological assessment and immunostaining analysis.....	91
2.2.22 Nanoindentation analysis .....	91
2.2.23 Fourier-Transform Infrared Spectroscopy (FTIR) analysis	92
2.2.24 Statistical analysis .....	93
2.3 Results.....	93
2.4 Discussion.....	127
2.5 Summary .....	130

**Chapter 3. Chondroitin sulfate-based biom mineralizing hydrogel for bone tissue engineering ..... 133**

3.1 Introduction.....	133
3.2 Materials and methods .....	135
3.2.1 Preparation of methacrylate-chondroitin sulfate.....	135
3.2.2 Preparation of hydrogel by photoencapsulation.....	136
3.2.3 Infrared spectroscopy .....	137
3.2.4 Zeta potential analysis.....	137
3.2.5 Swelling and mechanical properties .....	137

3.2.6 Scanning electron microscopy and calcium accumulation assays .....	138
3.2.7 Fluorescence assay for calcium determination .....	139
3.2.8 Ammonium molybdate assay for phosphate determination .....	140
3.2.9 In vitro apatite forming ability .....	141
3.2.10 Cell-encapsulated hydrogel preparation and viability.....	141
3.2.11 Gene expression analysis .....	143
3.2.12 Ethics statement .....	145
3.2.13 Calvarial defect procedure and in vivo cell-laden hydrogel transplantation.....	145
3.2.14 Micro-CT analysis.....	146
3.2.15 Statistical analysis .....	146
3.3 Results.....	149
3.3.1 Synthesis and characterization of methacrylated chondroitin sulfate hydrogel.....	149
3.3.2 Calcium and phosphate ion deposition on CS-based hydrogel .....	153
3.3.3 In situ formation of calcium phosphate derivatives on the surface of CS-based hydrogels.....	160
3.3.4 In vitro biocompatibility and gene expression profiles of hTMSCs .....	163
3.3.5 In vivo bone tissue regeneration of cell-laden hydrogels...	167
3.4 Discussion.....	169
3.5 Summary .....	174
<b>Chapter 4. Concluding remarks .....</b>	<b>175</b>

4.1 Summary .....	175
4.2 Further suggested research ideas .....	178
<b>Reference.....</b>	<b>180</b>

# List of Tables

**Table 2.1** Mesenchymal gene expression of whitlockite (WH:  $\text{Ca}_{18}\text{Mg}_2(\text{HPO}_4)_2(\text{PO}_4)_{12}$ ) vs. hydroxyapatite (HAP:  $\text{Ca}_{10}(\text{PO}_4)_6(\text{OH})_2$ ) in hTMSC culture with 2D scaffolds ..... **80**

**Table 2.2** Primer sets for human genes used in this study ..... **81**

**Table 3.1** Primer sets for human genes used in this study ..... **144**

# List of Figures

<b>Figure 1.1</b> Different types of inorganic materials and its product form of (a) Hydroxyapatite-based materials .....	<b>5</b>
<b>Figure 1.2</b> Schematic model of mineralized matrix-induced osteogenic differentiation .....	<b>6</b>
<b>Figure 1.3</b> Whitlockite nanoparticle characterization .....	<b>13</b>
<b>Figure 1.4</b> Schematic showing the different preparation methods of injectable hydrogel and various biomimetic strategies that have been explored for bone regeneration .....	<b>28</b>
<b>Figure 1.5</b> Schematic showing the different preparation methods of injectable hydrogel and various biomimetic strategies that have been explored for bone regeneration .....	<b>33</b>
<b>Figure 1.6</b> Schematic diagram showing diffusion of implant-derived $Mg^{2+}$ .....	<b>34</b>
<b>Figure 1.7</b> Fabrication methods for complex macroporous scaffolds .....	<b>41</b>
<b>Figure 1.8</b> Versatility, scalability, and manipulation of 3D-printed HB .....	<b>51</b>
<b>Figure 1.9</b> Different growth factor delivery design for dual or multiple growth factor delivery system for bone regeneration .	<b>52</b>
<b>Figure 2.1</b> WH-embedded hybrid 3D cryogel characterization	<b>85</b>
<b>Figure 2.2</b> Subcutaneous cryogel experiment.....	<b>88</b>
<b>Figure 2.3</b> Synthesis and material characterization of the two major biominerals, whitlockite (WH: $Ca_{18}Mg_2(HPO_4)_2(PO_4)_{12}$ ) and hydroxyapatite (HAP: $Ca_{10}(PO_4)_6(OH)_2$ ) .....	<b>95</b>

<b>Figure 2.4</b> Bright field image and diffraction pattern of a single whitlockite (WH: $\text{Ca}_{18}\text{Mg}_2(\text{HPO}_4)_2(\text{PO}_4)_{12}$ ) nanoparticle, along the $[-1\ 2\ -1]$ zone axis .....	<b>97</b>
<b>Figure 2.5</b> X-ray photoelectron spectroscopy of whitlockite (WH: $\text{Ca}_{18}\text{Mg}_2(\text{HPO}_4)_2(\text{PO}_4)_{12}$ , red line) and hydroxyapatite (HAP: $\text{Ca}_{10}(\text{PO}_4)_6(\text{OH})_2$ , black line).....	<b>98</b>
<b>Figure 2.6</b> Effect of whitlockite (WH: $\text{Ca}_{18}\text{Mg}_2(\text{HPO}_4)_2(\text{PO}_4)_{12}$ ) and hydroxyapatite (HAP: $\text{Ca}_{10}(\text{PO}_4)_6(\text{OH})_2$ ) nanoparticles on the surrounding system, particularly at their near surface .....	<b>101</b>
<b>Figure 2.7</b> Amount of absorbed protein in the whitlockite and hydroxyapatite scaffold .....	<b>102</b>
<b>Figure 2.8</b> Differentiation of human tonsil-derived mesenchymal stem cells (hTMSCs) on WH and HAP discs by the phosphate and magnesium ion effect .....	<b>105</b>
<b>Figure 2.9</b> Additional 2D cylindrical scaffolds analysis.....	<b>107</b>
<b>Figure 2.10</b> Magnesium influence in osteogenic differentiation .....	<b>110</b>
<b>Figure 2.11</b> Inhibitory effect of WH on osteoclastic differentiation by phosphate and magnesium ions .....	<b>115</b>
<b>Figure 2.12</b> Experimental scheme of the effect of $\text{Mg}^{2+}$ , $\text{PO}_4^{4-}$ , WH and HAP on osteoclast differentiation .....	<b>116</b>
<b>Figure 2.13</b> Phase transformation of whitlockite to hydroxyapatite .....	<b>119</b>
<b>Figure 2.14</b> <i>In vivo</i> bone regeneration efficacy of whitlockite (WH: $\text{Ca}_{18}\text{Mg}_2(\text{HPO}_4)_2(\text{PO}_4)_{12}$ ) embedded 3D cryogel implants .....	<b>122</b>
<b>Figure 2.15</b> Simplified schematic <i>in vitro</i> model of effect of whitlockite nanoparticles on MSCs, osteoclast activity, and HAP phase transformation.....	<b>125</b>

<b>Figure 2.16</b> Characterization of human tonsil derived mesenchymal stem cells (hTMSCs).....	<b>126</b>
<b>Figure 3.1</b> Preparation of PEGDA-MeCS hydrogel used for osteogenic differentiation of hTMSCs .....	<b>148</b>
<b>Figure 3.2</b> Characterization of prepared PEGDA-MeCS hydrogels .....	<b>151</b>
<b>Figure 3.3</b> Calcium and Phosphate Ion bound by MeCS Hydrogel.....	<b>152</b>
<b>Figure 3.4</b> Confirmation of accumulated Ca and Phosphate ions .....	<b>155</b>
<b>Figure 3.5</b> In vitro calcium phosphate (CaP) forming ability and differentiation of hTMSCs .....	<b>156</b>
<b>Figure 3.6</b> Detection of accumulated phosphorous element within MeCS-rich hydrogels via EDS elemental mapping.....	<b>157</b>
<b>Figure 3.7</b> Detection of accumulated calcium ions on MeCS hydrogels by Alizarlin’s staining.....	<b>158</b>
<b>Figure 3.8</b> X-ray diffraction pattern of hydroxyapatite accumulated onto the surface of MeCS hydrogel (a), and its calcium/phosphate ratio (b).....	<b>159</b>
<b>Figure 3.9</b> <i>In vitro</i> cell studies on MeCS Hydrogel .....	<b>162</b>
<b>Figure 3.10</b> <i>In vivo</i> hydroxyapatite forming .....	<b>165</b>
<b>Figure 3.11</b> <i>In vivo</i> transplantation and bone regeneration ...	<b>166</b>

# **1. CHAPTER ONE: THE SCIENTIFIC**

## **BACKGROUND AND RESEARCH**

### **PROGRESS**

#### **1.1 Overview**

Bone tissue is one of the most extensive and ubiquitous organs in the human body, and failure of its function is one of the main causes of reduced quality of life [1]. The solution presented by organ transplantation involves profound socioeconomic challenges, mainly concerning the lack of tissue donors, multiple invasive surgeries with extra invasions, and high costs. Roughly two million bone grafting procedures are performed internationally every year on the spine, pelvic bone and other body extremities [2]. However, approximately 50% of the implants, both autogenous and allo-grafts, fail very quickly [3]. The high incidence of bone and joint related disorders and diseases, such as osteoporosis, arthritis, obesity, diabetes, and cancer, causes injury to

orthopedic tissues and affects the health and performance of the human skeleton.

For proper bone regeneration, bone scaffolds need to be rigid enough to support mechanical strength and pressure. In addition, the composition of a scaffold should consist of biocompatible materials that elicit minimal host tissue inflammation. It is also important for such a scaffold to mimic the configuration of natural bone tissue in which progenitor cells commit to an osteogenic lineage in a bone-like microenvironment. Finally, scaffolds should also provide an optimal microenvironment for blood vessel recruitment and inorganic material deposition.

Recently, calcium phosphates have been reported to provide an osteo-friendly environment for mesenchymal stem cells [4-6]. Among various calcium phosphates, hydroxyapatite (HA) is the mineral primarily found in bones and involved in osteoconduction and osteoinduction [7-9]. One of the major limitation of HA in a clinical setting is its low resorption rate *in vivo* coupled with low crack resistance and poor bone stimulation [10]. Thus, researchers have been actively

searching for calcium phosphate-composed materials with improved properties for bone tissue engineering, such as beta-tricalcium phosphate ( $\beta$ -TCP), whitlockite (WH) and bioglass (Figure 1.1).

Bone has complex structures and diverse and dynamic mechanical properties; the elastic moduli of human bone tissue varies between 1 and 20 GPa [11]. To accomplish bone regeneration with physiochemical composition similar to natural bone, artificial bone substitutes should have the necessary structural support elements to meet the mechanical strength of natural bone matrix. Since a porous structure is a distinguishing feature of natural bone tissue, additional scaffold designs that include a micro-pore structure within artificial bone scaffolds could provide an added benefit to seeded cells in terms of favorable growth conditions, host cell migration, and enhanced osteogenic differentiation. From a bone regeneration point of view, it is well understood that sufficient blood vessel formation is required for large bone regeneration. Recent studies have indicated that in addition to their well-known role of supplying oxygen and nutrients to bone, blood vessels may also have a role in determining the area of bone formation as they help in the migration of osteoprogenitor cells, [12, 13]. This close

relationship is mostly referred to as osteogenic-angiogenic coupling. Porous scaffolds play a major role in neovascularization. To create porous scaffolds, a variety of strategies, such as salt leaching, gas foaming and lyophilization, have been utilized to fabricate desired 3D porous structures in biodegradable poly-ester based synthetic biomaterials, such as PLGA/PLLA and polyurethane. In addition, electrospinning and 3D printing are also being exploited to make complex structures. However, the fabrication techniques utilized to construct scaffolds solely depend on material types. For example, the porous structures of amorphous glass scaffolds, glass-ceramic scaffolds, and crystalline ceramic scaffolds can only be obtained through a sintering process [14]. In this report, we will review a fabrication technique for an artificial bone substitute that can generate complex structures and diverse physiochemical mechanical properties similar to those of natural bone.

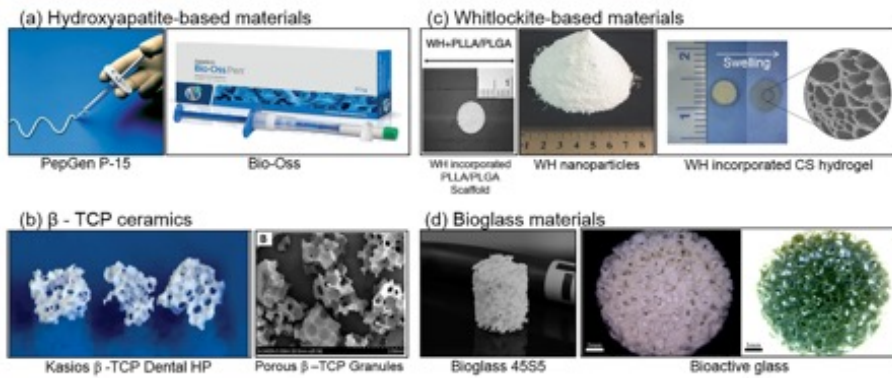


**Figure 1.1** Different types of inorganic materials and its product form of (a) Hydroxyapatite-based materials[15, 16], (b)  $\beta$  - TCP ceramics[17, 18], (c)Whitlockite-based materials[19, 20], and (d) Bioglass materials[21, 22].

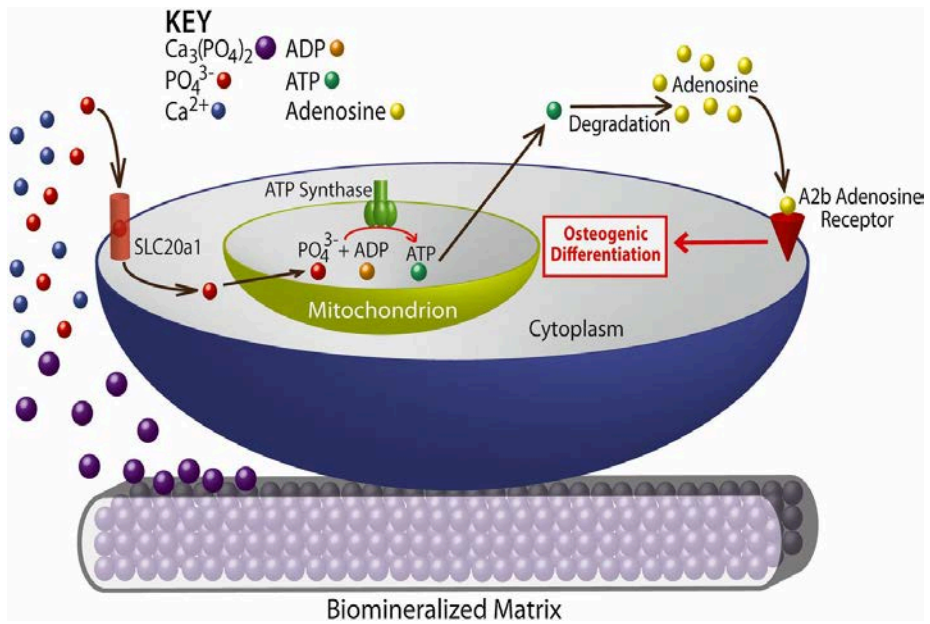


**Figure. 1.2** Schematic model of mineralized matrix-induced osteogenic differentiation [5].

## **1.2 Current state of synthetic inorganic materials for bone tissue engineering scaffolds**

To stimulate the osteogenic differentiation of stem cells, osteoinductive and osteoconductive materials, such as calcium phosphate, have been incorporated into 3D scaffolds. Calcium phosphate is the main component of natural bone tissue and has been demonstrated to stimulate osteogenesis in stem cells and osteoprogenitor cells [23]. In recent years, it was discovered that the phosphate ions released from calcium phosphate derivatives play a key role in inducing osteogenic differentiation in stem cells. Our group has demonstrated that the increased local phosphate ion concentration in bioresorbed calcium phosphate scaffolds accelerates phosphate ion uptake by the cells, which in turn catalyzes the conversion of ADP to ATP within stem cells. ATP, which is at an elevated concentration, is excreted and metabolized into adenosine nucleotides around the cells, talking to the stem cells via autocrine and/or paracrine mechanisms to activate the intracellular adenosine signaling pathway [5]. Elevated intracellular adenosine levels have been associated with nuclear localization through the A2b adenosine receptor, which activates bone-related transcription factors,

such as osteocalcin and osteopontin (Figure 1.2). This effect highlights the importance of the compositional aspect of artificial bone grafts to provide desired biological responses.

### **1.2.1 Hydroxyapatite (HA)**

Among the calcium phosphate family, hydroxyapatite (HA:  $\text{Ca}_{10}(\text{PO}_4)_6(\text{OH})_2$ ) is the main inorganic material that composes most human bones. HA has been used as the main material in bone implants because of its high biocompatibility and capacity to integrate with natural bone tissue [24]. An important characteristic of HA is its stability compared to other calcium phosphates. Thermodynamically, HA is the most stable form of calcium phosphate compounds under physiological conditions, such as temperature, pH, and body fluid composition [23]. HA is naturally found in igneous rocks, metamorphic rocks, phosphate rocks and even in meteorites. However, most naturally existing HA or crystallites with an apatite structure contain various ions and vacancies, which makes them highly defective or poorly crystallized. For experimental use, HA can be easily synthesized by mixing 1 M  $\text{Ca}(\text{OH})_2$

with 0.6 M  $\text{H}_3\text{PO}_4$  in an aqueous system. Dropwise addition of  $\text{H}_3\text{PO}_4$  into the vigorously stirring state of a  $\text{Ca}(\text{OH})_2$  aqueous solution can be effective at minimizing the formation of other heterogeneous phases because the addition of a large amount of  $\text{H}_3\text{PO}_4$  at one time can temporarily induce a strong acidic environment in local regions of the  $\text{Ca}(\text{OH})_2$ - $\text{H}_3\text{PO}_4$  system, which rapidly grows pellets of DCPD or DCPA at the several micrometer scale. However, even when intermediate phases are formed, crystallites in the neutral pH range or those that are placed in a high-temperature environment can result in a fast phase transition toward HA.

Even though HA is one of the most stable forms of calcium phosphate, its application in bone regeneration is currently limited. Sintered hydroxyapatite exists in a hardened form, requiring the surgeon to drill the surgical site around the artificial grafts or to grind the graft to the desired shape. This additional procedure can lead to an increase in bone loss, patient suffering, and surgical time. Since its degradation at biological pH is particularly slow, the stimulating effect of dissolved ions on the surrounding environment is negligible. Furthermore, its mechanical properties are extremely brittle, making it unable to be used

as a load bearing implant. Therefore, to compensate for these drawbacks, mixtures of HA with  $\beta$ -TCP and polymer are currently marketed as synthetic bone products.

### **1.2.2 Beta-tricalcium phosphate ( $\beta$ -TCP)**

Beta-tricalcium phosphate ( $\beta$ -TCP:  $\text{Ca}_3(\text{PO}_4)_2$ ), also a popular calcium phosphate material, is often used due to its good biodegradability, which allows the newly regenerated bone to replace the substance once it is degraded.[25]. Many implants for bone regeneration consist of both HA and  $\beta$ -TCP to benefit from the biodegradability of  $\beta$ -TCP and the high biocompatibility of HA. TCP is available as two different forms: alpha-tricalcium phosphate ( $\alpha$ -TCP,  $\alpha\text{-Ca}_3(\text{PO}_4)_2$ ) and beta-tricalcium phosphate ( $\beta$ -TCP,  $\beta\text{-Ca}_3(\text{PO}_4)_2$  | Ca-to-P molar ratio of 1.5). The types are formed based on temperature modification;  $\alpha$ -TCP is produced at a temperature above  $1125^\circ\text{C}$ , whereas  $\beta$ -TCP is produced at a temperature below  $1125^\circ\text{C}$  [26]. Unlike  $\alpha$ -TCP,  $\beta$ -TCP is thermodynamically stable in a biological system and has a faster biodegradation rate because it is hydrolyzed to HA [26]. The first clinical application of TCP was for

defective bone repair by Albee in 1920, and since 1999, purified  $\beta$ -TCP has been applied in bone tumor surgery [27].

As mentioned above, one of the important features of  $\beta$ -TCP in a biological system is degradation.  $\beta$ -TCP can be degraded more rapidly than HA inside the body because  $\beta$ -TCP has thermodynamically higher solubility than HA [28]. Additionally,  $\beta$ -TCP has a higher resorption rate than HA, which eventually led researchers to develop biphasic calcium phosphate (BCP), a mixture of  $\beta$ -TCP and HA [29]. *Daculsi et al.* implanted BCP macro porous ceramics with different  $\beta$ -TCP / HA mass ratios in osseous defects in dogs and reported that the resorption rate of BCP ceramics increased with an increasing  $\beta$ -TCP / HA mass ratio [30].

*Neo et al.* confirmed that the degradation of  $\beta$ -TCP can be achieved *in vivo* and that dense sintered  $\beta$ -TCP bonds to bone directly, which showed that the bone bonding mechanism of  $\beta$ -TCP is different from that of HA [31]. Additionally,  $\beta$ -TCP has excellent properties for bone marrow stromal cell culture toward osteogenic differentiation [32], and  $\beta$ -TCP with bone morphogenetic protein (BMP) can improve bone regeneration [33]. *Yokozeiki et al.* reported that the micro pores of  $\beta$ -TCP, which are approximately 0.1–0.5 nm in size, had a significant role in

resorption in bones, suggesting that nano-size pores in  $\beta$ -TCP ceramics can control cell-mediated resorption and bone formation [34]. Furthermore, in terms of cell proliferation,  $\beta$ -TCP porous ceramics serve as excellent scaffolds, providing space for cells to attach while the material degrades with bone regeneration [35].

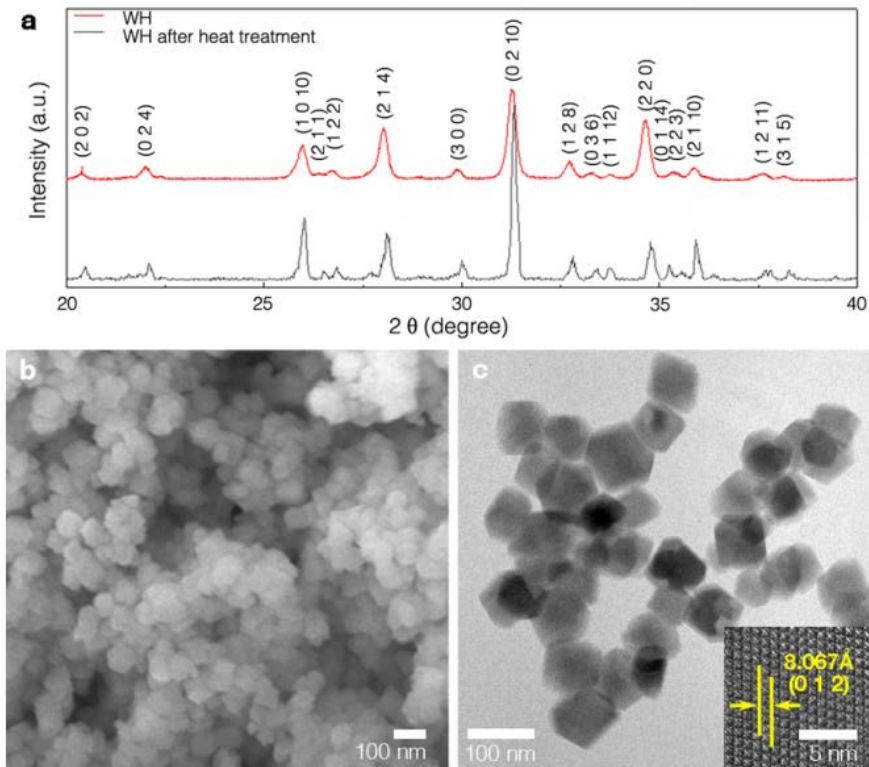


**Figure 1.3** Whitlockite nanoparticle characterization. (a) XRD patterns showing the pure phase of the synthesized whitlockite (WH: red line). WH maintained its pure phase even after being heat-treated at 1450 C for 2 h (gray line). (b) FESEM image of homogeneously formed WH nanoparticles. (c) High-resolution TEM image of rhombohedral shape of WH nanoparticles with approximately 50 nm size. As shown in the bottom right inset, the d-spacing value was measured to be 8.067 Å for the WH nanoparticles, which corresponded to the (0 1 2) plane of WH [27].

### 1.2.3 Whitlockite

$\beta$ -TCP does not exist in the human body, but there is whitlockite (WH:  $\text{Ca}_9\text{Mg}(\text{HPO}_4)(\text{PO}_4)_6$ ), which is one of the calcium phosphate derivatives that has Mg as the 2<sup>nd</sup> cation in its lattice. Although HA is a major inorganic phase, short-range ordered WH phase in an amorphous form also exists in human bone and dentin at an estimated amount of approximately 20 weight percent (%) for bone and 26 to 58 weight percent (%) for dentin based on the amount of Mg. WH can also be detected in human gallstone, teeth, and cartilage [36-39]. The mechanical/degradation properties of WH are more similar to  $\beta$ -TCP than HA. In terms of the cation: anion ratio,  $\beta$ -TCP shows 1.5:1 and WH shows 1.43:1, whereas HA shows 1.67:1. From observation by optical microscopy, individual particles of  $\beta$ -TCP and WH have a rhombohedral morphology [40], but the structure of HA is hexagonal. Therefore, WH has high scientific value as it has the potential to overcome the drawbacks of  $\beta$ -TCP and HA.

WH nanoparticles are generally synthesized in a low-temperature condition. In the presence of Mg ions in calcium phosphate

solution, a partial formation of the WH phase has been reported. To precipitate WH, *Cheng et al.* added 250 ml of a solution containing calcium and magnesium ions into a phosphate solution by the dropwise method [41]. However, these methods suffered from the formation of other heterogeneous phases, such as apatite or amorphous products. Recently, *Jang et al.* devised a new method to synthesize pure WH nanoparticles for the first time [42]. For the stepwise approach, the method itself is very straightforward and environmentally friendly since the process proceeds in an aqueous system without generating any harmful 2<sup>nd</sup> ions, such as sulfuric or nitric acid. According to XRD patterns from previous research, synthesized WH has high purity and an identical crystal structure to Mg-substituted TCP. From Field Emission Scanning Electron Microscopy (FESEM) analysis, WH nanoparticles had a rhombohedral-like shape with a homogeneous size of approximately 50 nm (Figure 1.3). This newly synthesized calcium phosphate exhibited excellent biocompatibility and osteoinductivity, which were comparable to traditional HA. Furthermore, WH incorporated scaffolds showed the highest osteogenic gene expression behavior *in vitro* among HA and  $\beta$ -TCP groups [43].

Furthermore, our group physically incorporated WH nanoparticles into 3D porous polymeric scaffolds, facilitating the osteogenic commitment of MSCs in a mouse cranial defect model. The rapid release of large amounts of calcium, magnesium, and phosphate ions from incorporated WH nanoparticle scaffolds were directly taken up by particular channels of mesenchymal stem cells and monocytes. These ions either facilitated osteo-related gene expression of mesenchymal stem cells to differentiate into bone cells or inhibited osteoclast differentiation in the monocytes. Furthermore, WH and HA concentrations within scaffold played a significant role in controlling stem cell fate and directed the ossification process in cells. These data indicate that the biomineral microenvironment serves an important role in stem cell differentiation [19].

#### **1.2.4 Bioglass**

Bioglass is a material composed of calcium, phosphate, and silicon. This material has been known to be biocompatible and osteoinductive because it facilitates enhanced cell migration and differentiation. Bioglass

integrates with native bone tissue by producing a calcium phosphate layer that can form a chemical bond to native bone. *Piattelli et al.* confirmed that bioglass particles enhanced both the proliferation and osteo-commitment of cells [44]. Newly regenerated bone was found near bioglass particles and located in the central part of a bone defect in rabbit tibia. *Yang et al.* constructed a chitosan/bioglass three-dimensional (3D) porous scaffold by needle-coating and dip-coating with bioglass [45]. They demonstrated that chitosan/bioglass 3D porous scaffolds exhibited good biocompatibility, high cell proliferation rates and potential for bone tissue engineering.

Bioglass is a form of bioactive ceramic that enhances osteo-regeneration and is widely used in implants and scaffolds [46]. The first form of bioglass, which was later named 45S5, is composed of 45% SiO<sub>2</sub>, 24.5% Na<sub>2</sub>O, 24.5% CaO, and 6% P<sub>2</sub>O<sub>5</sub> and was invented by professor Larry Hench [47]. Implantation of bioglass in rats for six weeks showed the formation of a strong bond between implanted bioglass and natural bone [46, 47]. After the invention of bioglass, researchers began to question the bond strength and its mechanism. *Piotrowski et al.* tested the mechanical strength of the bond between bioglass and bone in

monkeys and found that the bond between bioglass and bone was three-fourth as strong as host bone [48].

The overall mechanism of bioglass degradation involves ion release and surface reaction. The first mechanism step is the exchange between sodium ions in bioglass and hydrogen ions from the environment, causing the breakdown of Si-O-Si bonds to form Si-OH bonds on the surface of the bioglass. After formation of Si-OH bonds, Si-OH bonds condensate and re-polymerize into a SiO<sub>2</sub> layer on the bioglass surface. Then, calcium and phosphate ions move to the top of the newly formed SiO<sub>2</sub> layer to form an amorphous calcium phosphate layer, which then crystallizes into a hydroxyapatite crystal. The hydroxyapatite crystal formed on the surface assists with the adsorption of biological moieties from hosts [49, 50].

Two fabrication techniques for synthesizing bioglass are traditional melting methods and sol-gel techniques [51]. The traditional melting method generates bioglass by melting oxides at high temperature in a platinum container and cooling in a graphite mold, whereas the sol-gel method produces bioglass by sintering silica gel at approximately 600 degrees Celsius [46]. Currently, the sol-gel technique is widely used to

produce bioglass over traditional melting methods. The major disadvantages of using the traditional melting method over the sol-gel technique are as follows: 1) difficulty maintaining high purity of the substance due to high temperature, 2) possible contamination during grinding, 3) compositional limitation due to the high viscosity of silicate melts after melting at high temperatures, and 4) high production costs due to using high temperatures [51, 52]. Due to the osteoinductive and bioactivity of bioglass, several studies were published modifying the composition of bioglass to enhance its bioactivity and osteogenic differentiation capabilities, such as modifications with copper [53], strontium [54], titanium [55], and boron [56].

### **1.3 Synthetic scaffolds for bone tissue engineering**

#### **1.3.1 Composite scaffolds based on calcium phosphate synthetic inorganic materials**

Currently, there are many different methods for preparing synthetic bone scaffolds. Porosity, mechanical strength, and biocompatibility are fundamentally important parameters to be considered when preparing

bone scaffolds. Large porous materials for scaffolds improve the infiltration of cells and proteins. The mechanical strength of the materials will protect them from external force or intervention. Since materials are implanted to a defect area, biocompatibility is required. Most researchers are focused on various calcium phosphates as bone scaffolds and the use of bioactive molecules to enhance the cellular integrity of the graft. Current research directions in the field of synthetic bone scaffolds are biocompatible bone scaffolds, ceramic bone scaffolds, bioactive bone scaffolds, growth factor encapsulation systems for enhancing bone formation and polymeric bone defect fillers.

For biocompatible bone scaffolds, *Erbe et al.* developed a material with biopolymer and inorganic material [57, 58]. This development integrates the benefits of inorganic shaped bodies with different porosities with biopolymers like collagen. Different amounts of calcium phosphates, such as hydroxyapatite (HA), beta-tricalcium phosphate ( $\beta$ -TCP) and other calcium phosphate families, have all been incorporated to match the biocompatibility, structure, and strength of natural bone. The role of pore size and porosity in promoting the revascularization, healing, and remodeling of bone has been recognized

as a critical property of bone grafting materials. Moreover, *Hwang et al.* incorporated hydroxyapatite (HA) into PLLA-PLGA scaffolds and showed that the ossification of human embryonic stem cell-derived mesenchymal stem cells was controlled by these scaffolds [59]. *Kim et al.* developed PLGA-PLA based mesh scaffolds coated with extracellular matrix (ECM) [60].

For ceramic bone scaffolds, biodegradable polymers (PCL) were used with calcium phosphate to enhance bone grafts for tissue engineering applications [61-63]. The polymer can also be used for the delivery of various agents (proteins or growth factors) through the porous ceramic matrix, and moreover, it improves the implant's mechanical properties *in vivo*. For bioactive bone grafts, *Nyemscek and Kikuchi et al.* developed biocompatible bone grafts made of resorbable calcium phosphate, collagen, and bioactive glass [64, 65]. A biocompatible, re-absorbable, homogeneous blend of calcium phosphate scaffolds with various pore sizes was developed. The graft mimicked native bone's osteoinduction by adding bioactive glasses. They examined different types of bioactive glasses, including glass-ceramics, crystalline phase materials, and a mixture of acrylic polymerizable species. The aim of using bioactive

glass was to react instantly when the glass came in contact with physiologic fluid, such as blood and serum. Reactions between the surrounding physiologic fluid and bioactive glass led to bond formation through the formation of an apatite layer on the graft surface.

*Levenberg et al.* fabricated scaffolds consisting of poly(L-lactic acid) (PLLA) and poly(lactic-co-glycolide) (PLGA) polymer scaffolds [66]. PLLA was able to provide mechanical strength to support 3D structure, whereas PLGA was able to be degraded quickly. They confirmed that this 3D scaffold contributed to specific tissue formation for human embryonic stem cells. *Yoshimoto et al.* fabricated electrospun PCL scaffolds that were able to support mineralized tissue and showed the possibility of their clinical applications in bone defects [67]. PCL-based scaffolds with surface modification could be used for tissue engineering. *Shao et al.* conjugated specific peptides onto the surface of PCL electrospun mesh scaffolds, which exhibited increased cell adhesion and cell expansion [68]. These results suggested potential tissue engineering applications, including bone tissue engineering to stimulate tissue regeneration via surface modification. Furthermore, PCL was applied as a coating material for the surface modification of metal

scaffolds. The fast degradation rate of several metals has limited the application of bone tissue engineering scaffolds. Magnesium coated PCL and bioactive glass (BG) showed enhanced bioactivity, mechanical properties and degradation resistance [69]. Since these rates are crucial factors in bone regeneration, mixtures of magnesium coated PCL and bioactive glass scaffolds are promising candidates for bone regeneration.

*Villa et al.* developed a collagen (Col)-HA scaffold by co-precipitation and freeze casting, which showed that Col-HA scaffolds are suitable for bone formation and exhibit good attachment to the host [70]. Col-HA scaffolds were implanted along with mesenchymal stem cells into a critical-sized calvarial defect and showed promise as a well-defined system for cell delivery and bone tissue regeneration. However, synthesized HA does not degrade in the body because of its high crystallinity and stability.

### **1.3.2      Injectable composite hydrogels based on calcium phosphate synthetic organic materials**

Hydrogels are water-swollen hydrophilic polymeric networks that can be formed from crosslinking macromers, polymerization of monomers or self-assembly of small molecules [71, 72]. The physicochemical properties of the hydrogel, such as its water content, viscoelasticity and matrix stiffness, can be fine-tuned by controlling the crosslinking chemistry, which decides the fate of stem cells cultured on it; for example, stiffer hydrogels promote osteogenic differentiation [73, 74]. In addition, chemical modification of the polymeric backbone enables tethering of biological cues to integrate into the hydrogel, mimicking the extracellular matrix (ECM) of tissues and thus aiding cell adhesion, migration and proliferation [75]. As an outcome, works have shown the creation of a niche that presents biological cues to cells in a spatiotemporal manner. However, there has been a recent paradigm shift to focusing on injectable hydrogels because pre-formed hydrogels face problems with improper adaptation to the defect margin and surgical implantation issues, as in the case of deep tissue defects in which improper defect filling leads to poor vascularization; therefore, these scaffolds fail in the sole purpose of improved tissue regeneration [72, 76, 77].

Injectable hydrogels can be prepared by *in situ* physical and chemical crosslinking. In depth descriptions of these preparation methods have been discussed earlier [71, 78]. A new class of shear thinning hydrogels have prepared in which pre-formed hydrogels are injected in the defect site by injection (applying shear stress) and quickly regain the original viscosity and stiffness afterwards [76, 79, 80]. Recently, various hydrogels have been prepared using the aforementioned synthesis route with better moldability and 3D interconnected pores for bone regeneration (Figure 1.4). *Matsuno et al* [81] developed an injectable 3D alginate hydrogel with  $\beta$ -TCP beads that induces gelation. MSCs were cultured in the hydrogel, and subcutaneous implantation of the hydrogel with stem cells favored osteogenic differentiation.  $\beta$ -TCP beads and mechanical stiffness would have been favorable for stem cells differentiation to an osteogenic lineage. *Dessi et al.* developed thermosensitive injectable chitosan hydrogels containing  $\beta$ -glycerophosphate, which is responsible for thermal gelation. The addition of  $\beta$ -TCP improved the physical strength of the hydrogel [81]. *Dhivya et al.* developed zinc doped chitosan thermosensitive hydrogels. nHAp was added to reinforce the hydrogel. The prepared system showed

a gelation time of 10 mins, and the incorporation of nHAp enhanced osteogenic differentiation and bone formation *in vivo* [82]. Furthermore, to add a biological cue to the hydrogel network, *Burdick et al.* prepared injectable photocrosslinked RGD tethered PEG to the hydrogel. The density and cell area of the osteoblasts were greatly enhanced in the RGD modified hydrogel in comparison to the unmodified hydrogel [83]. Cytoskeletal organization was seen only in the RGD tethered system. The tethered system also enhanced mineralized matrix formation and showed that the addition of cell adhesive peptide is desirable for bone regeneration. Furthermore, to increase strength and biomimetic bone architecture, *Fu et al.* prepared three-component thermo-gelling hydrogels composed of PEG-PCL-PEG block copolymer, collagen and nHA. The system resulted in an interconnected porous hydrogel network with the pore size of 40  $\mu\text{m}$ , which could possibly aid cell migration. *In vivo* studies in rabbit cranial defects showed that the prepared hydrogel system showed enhanced bone formation compared to the control [84]. Incidentally, it was not a full through cranial defect model, so further studies in full through cranial defects need be studied to ascertain the benefits of the system. *Thorpe et al.* studied a laponite crosslinked

pNIPAM-DMAc copolymer that was incorporated with nHAp. The developed system was able to differentiate MSC into an osteogenic lineage without the presence of osteogenic inducers and growth factors [85]. A combination of nHAp and nanoclay was able to induce osteogenesis, holding possible potential for cost-effective translation.

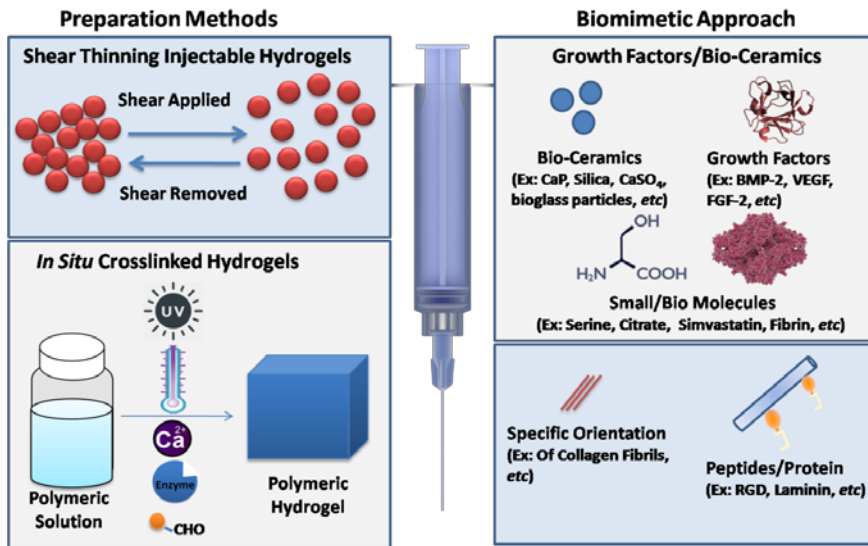


**Figure 1.4** Schematic showing the different preparation methods of injectable hydrogel and various biomimetic strategies that have been explored for bone regeneration.

*Xie et al.* developed citrate based adhesive injectable bone scaffolds [86] because citrate was found to be indispensable for the formation and regulation of nanocrystalline apatite platelets in bone. Incidentally, it is understood that citrate anion bridges between bone apatite helps to separate crystals rather than forming a large block of hydroxyapatite in bone [87]. The setting time for the system was found to be 2-4 minutes, and the citrate released from the system helped in bone formation. A comminuted radial fracture model in rabbits was used as an *in vivo* model. It was shown that the prepared material enhanced bone formation, flexural strength and neo-vascularization. Many studies have been carried out by incorporating growth factors, which are cell instruction molecules, in the injectable hydrogel system [88-92]. The incorporation of ceramic material helps to better control delivery of the GF or drug [93-96]. Incorporation of the drug/GF in the system can be achieved in the following ways: 1) adsorb the drug/GF in the ceramic material and incorporate it in the hydrogel, 2) incorporate the drug/GF in the hydrogel and then incorporate ceramic materials in the system and 3) mix the drug/GF in the hydrogel/ceramic composite.

*In situ* hydrogels require the injection of a liquid precursor in the defect site, and it is possible that this precursor could leak into the neighboring defect site or become diluted in the physiological fluid, which affects hydrogel gel formation in terms of its gelation time and elastic strength [80, 97]. To overcome this challenge, researchers have focused on shear thinning hydrogels, as they can more rapidly recover or self-heal after injection in comparison to *in situ* forming gels. Wang *et al.* studied the shear thinning behavior of colloidal gelatin nano and microparticles. Nano structured colloidal gelatin gels showed higher recovery (>80% in 5 minutes), whereas micro particulates showed less than 10% recovery at same time point. This phenomenon could be attributed to the fact that the nanoparticles had a higher surface area to volume ratio, leading to and increased number of electrostatic interactions and thereby higher crosslinking density. They also showed near the zero order release kinetics of BMP-2 encapsulated in nano colloidal gel [98]. Arun Kumar *et al.* developed injectable shear thinning chitin-PCL/nHAp hydrogels for bone regeneration. Incorporation of nHAp in the hydrogel resulted in early osteogenesis with enhanced expression of osteoid matrix proteins, such as osteocalcin and osteopontin [99]. To enhance vascularization,

fibrin nanoparticles (FBN) were incorporated in the hydrogel network [100-102]. Incidentally, the incorporation of FBN changed the morphology of calcium sulfate crystals from a needle-like to hexagonal morphology with an aspect ratio of nearly one. Further studies are required to study the role of crystal morphology on bone regeneration; nevertheless, the prepared hydrogel system showed enhanced cell adhesion and angiogenesis, which is one step closer to osteo-angiogenic coupling in bone regeneration [103]. Furthermore, *Vishnu Priya et al.* developed injectable shear thinning chitin/poly (butylene succinate) hydrogels containing FBN and magnesium doped bioactive glass. Magnesium ions and FBN showed enhanced vascularization behavior in an aortic ring assay. The incorporation of bioglass helped in osteogenic differentiation, even when osteogenic supplements were not added [104]. These systems hold potential for better bone regeneration, which needs to be ascertained under *in vivo* conditions. *Dennis et al.* developed biomimetic shear thinning hydrogels by incorporating micron-sized native bone ECM in hyaluronic acid (HA)-HAp colloidal hydrogels (Figure 1.5). The incorporation of ECM particles in the hydrogel enhanced its recovery and storage modulus, representing a synergetic

behavior between ECM and the HA-HAp composite. Initial *in vitro* cell viability assays showed that the prepared hydrogel system supported cell proliferation [105]. *Miri et al.* developed a gel aspiration-ejection technique for the preparation of aligned dense fibrillar collagen hydrogels. Second harmonic imaging shows that the alignment of the collagen fibrils is closely similar to bone architecture. 45S5 bioglass was incorporated in the hydrogel system for osteoinductivity. The BG incorporated system showed enhanced neo-angiogenesis, cell migration and mineralization compared to the control gel when it was subcutaneously injected [106].

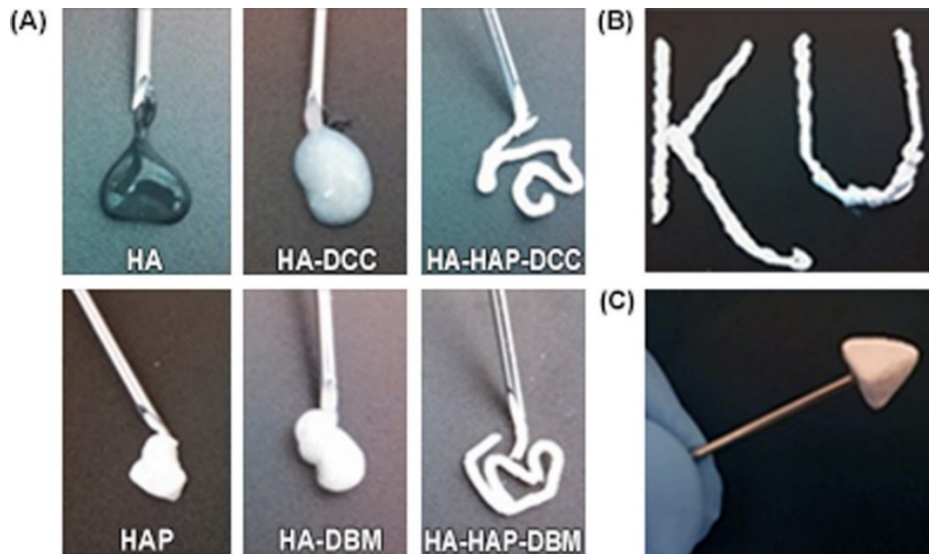


**Figure 1.5** (A) All tested HA-ECM and HA-HAP-ECM fluids could readily be loaded into 1 mL syringes and subsequently be extruded through 18-gauge needles. Colloidal gel formulations containing ECM microparticles could be shaped (B) during extrusion and (C) maintained form following handling. HA-HAP-DBM ( $\Phi_{\text{DBM}} = 0.15$ ) was shown above in images (B) and (C). HA, hyaluronic acid; HAP, hydroxyapatite; ECM, extracellular matrix; DCC, decellularized cartilage; DBM, demineralized bone matrix. <sup>[27]</sup>

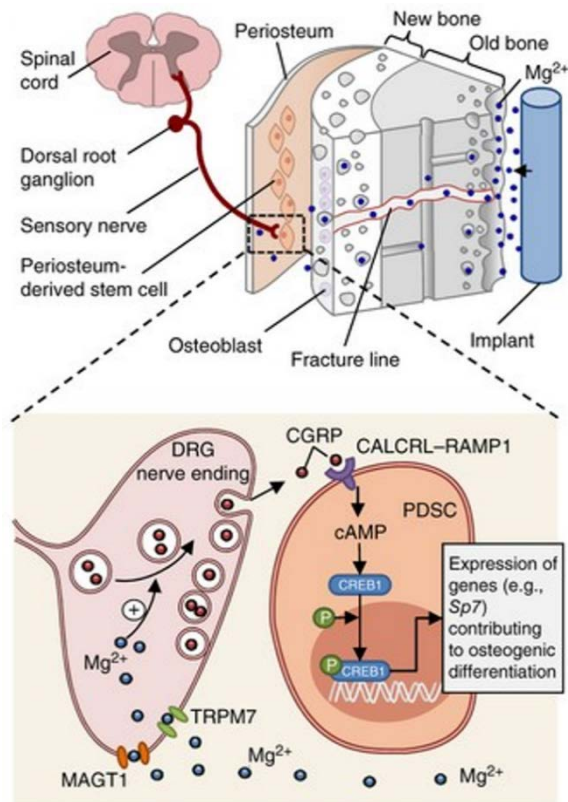


**Figure 1.6** Schematic diagram showing diffusion of implant-derived  $Mg^{2+}$  across the bone toward the periosteum that is innervated by DRG sensory neurons and enriched with PDSCs undergoing osteogenic differentiation into new bone (top). Inset (shown enlarged at bottom), the released  $Mg^{2+}$  enters DRG neurons via  $Mg^{2+}$  transporters or channels (i.e., MAGT1 and TRPM7) and promotes CGRP-vesicles accumulation and exocytosis. The DRG-released CGRP, in turn, activates the CGRP receptor (consisting of CALCRL and RAMP1) in PDSCs, which triggers phosphorylation of CREB1 via cAMP and promotes the expression of genes contributing to osteogenic differentiation. Reproduced with permission.<sup>[80]</sup> Copyright 2016, Nature Publishing Group.

In addition to ceramics apart from calcium phosphates, several metal-based ions have been shown to have osteoinductivity for bone tissue regeneration. Magnesium (Mg) based implants were investigated for orthopedic biomaterials because they have mechanical properties similar to native bone, biodegradability, and biocompatibility [107]. *Yoshizawa et al.* optimized the concentrations of Mg ions in culture medium for human bone marrow stromal cells and hypothesized the intracellular magnesium associated signaling pathway [108]. They confirmed that 10 mM Mg ion maximally stimulated the expression of osteogenic transcription factors. In particular, the role of Mg ions has been recently shown to have a very important role in bone homeostasis. Local Mg ions in the periosteal region in bone tissue can stimulate the dorsal root ganglia (DRG) that innervate bone tissues. This elevated Mg ion concentration from bone grafts can be taken up by the somatic end of DRG and causes the release of calcitonin gene-related polypeptide-a (CGRP) in both the peripheral cortex of the femur and the ipsilateral DRG, which directly act on the periosteum-derived stem cells (PDSCs) that line the periphery of bone tissues (Figure 1.6). CGRP binding to the

CGRP-receptor on PDSCs activate bone-related transcription factors, such as *CREB 1* and *Sp7* [109].

The current strategy for preparing hydrogels is to mimic the ECM of the tissue and thereby result in enhanced bone formation. Increased spatiotemporal control upon cellular cues would be next step in the future of tissue regeneration. The dynamic nature of the tissue has to be mimicked, and reversible chemical crosslinking without modifying bulk hydrogel properties can be incorporated in the system. Another directional change can be designing hydrogels with respect to the bone healing cascade. Further research on these aspects would have an effective outcome in bone regeneration.

#### **1.4 Fabricating method for complex macroscoporous bone like structure for increased vascularization**

Porosity and pore size are very important parameters in designing scaffolds for bone regeneration. Scaffolds also serve as osteoconductive material, as bone regeneration occurs from already existing bone walls. The porosity requirement for regeneration was studied by *Kuboki et al.*

using porous and solid HAp particles with BMP-2 in a rat ectopic model. Solid particles did not elicit bone formation, whereas porous particles helped in bone formation [110]. Furthermore, there are many reports that show that there is a porosity requirement for bone formation [111-113]. Pore size is an important parameter, as pores help in cell infiltration and new vascularization. It is understood that macro porosity (>50  $\mu\text{m}$ ) is necessary for cell infiltration for bone ingrowth, and Xiao *et al.* studied the relation between pore size and angiogenesis. Different disk shaped  $\beta$ -TCP plates with 100-, 120-, and 150- $\mu\text{m}$  interconnected pores containing samples were used for the study. Scaffolds with a 150- $\mu\text{m}$  pore size showed considerably increased vascularization in comparison to other two pore sizes. The authors showed that 150- $\mu\text{m}$  pore size scaffolds enhanced new vascularization through the PI3K/Akt pathway [114]. Similarly, interconnected pore sizes were required as they were the gateway/pathway for blood vessel invasion. This phenomenon was studied by *Mastrogiacomo et al.*, who showed that pore interconnectivity affected osteoconductivity and new blood vessel formation [115]. All these studies show the importance of porosity and pore size distribution in scaffolds. Porosity can be incorporated in scaffolds through salt

leaching, gas foaming, freeze-drying, and electrospinning. Recently, with the advent of 3D printing, pore size and density can be controlled more precisely.

#### **1.4.1 Salt-leaching method**

Pore sizes of scaffolds are easily controllable using a salt leaching technique. Porogens, such as wax, salt, and sugars, are used to construct pores of scaffolds during the salt leaching process. The desired size of small salt particles is poured into the mold, then it is filled with the porogen. Finally, the polymer solution is added to the mold filled with salt and porogen. The pores of scaffolds are constructed as the salt crystals leach away using water from evaporation of the solvent [116]. The structural characteristics of scaffolds made by the salt leaching method are high porosities and pore sizes of approximately 500 micrometers. *Nasrabadi et al.* prepared starch/cellulose scaffolds in various conditions, such as 100/0, 95/5, 90/10, and 85/15, through the salt leaching technique [117]. Porosities of scaffolds increased as the concentrations of salts and celluloses increased. Nevertheless, the

compressive modulus decreased while the concentration of cellulose in the fabricated scaffolds increased.

## 1.4.2 Gas-forming methods

Unlike fabrication techniques used by organic solvents, the gas foaming technique uses high-pressure carbon dioxide to manufacture the scaffolds [118]. This technique not only provides a porous structure but also does not require the removal of residues of organic solvents that may damage cells [119]. The structure of a scaffold can be controlled by the amount of gas in the polymer. At high-pressure conditions, the polymer solution is saturated with inert gas. However, dissolved gas molecules in this condition are unstable, and as a result, gas molecules in the polymer solution soon amalgamate as they separate from the polymer solution, leaving pores on the scaffold [120]. *Nazarov et al.* used the gas foaming technique to fabricate three-dimensional scaffolds (Figure 1.7). They used hexane gas, which can permeate throughout  $\text{NH}_4\text{HCO}_3$ /silk scaffolds and does not cause shrinkage or swelling in scaffolds. The porosities of the 10:1  $\text{NH}_4\text{HCO}_3$ /silk (wt %) and 20:1  $\text{NH}_4\text{HCO}_3$ /silk

(wt %) scaffolds are  $87\pm 2.0\%$  and  $97\pm 1.0\%$ , respectively [121]. The compressive modulus of the 10:1 and 20:1 scaffolds were measured to be  $900\pm 94$  KPa and  $1000\pm 75$  kPa, respectively. *Nam et al.* used poly(L-lactic acid) and different concentrations of ammonium bicarbonate gas to construct scaffolds through the gas foaming process [122]. The porosities of the 10:1  $\text{NH}_4\text{HCO}_3/\text{PLLA}$  (wt %) and 10:1  $\text{NH}_4\text{HCO}_3/\text{PLLA}$  (wt %) scaffolds, which were previously wetted by ethanol before the gas foaming technique, and the 20:1  $\text{NH}_4\text{HCO}_3/\text{PLLA}$  (wt %) and 10:1  $\text{NH}_4\text{HCO}_3/\text{PLLA}$  (wt %) scaffolds with high salt size were measured by gross weight and volume and found to be 90.36%, 92.04%, 95.12%, and 93.52%, respectively. Porosities of 6:1 and 10:1 scaffolds and ethanol treated 10:1, 20:1, and 10:1 scaffolds with different salt size ranges were measured by mercury intrusion porosimetry as 86.60%, 88.73%, 89.89%, 93.49%, and 91.15%, respectively. The compression modulus of the 10:1  $\text{NH}_4\text{HCO}_3/\text{PLLA}$  and 20:1  $\text{NH}_4\text{HCO}_3/\text{PLLA}$  scaffolds were  $242.3\pm 32.5$  and  $65.8\pm 5.4$  kPa, respectively.

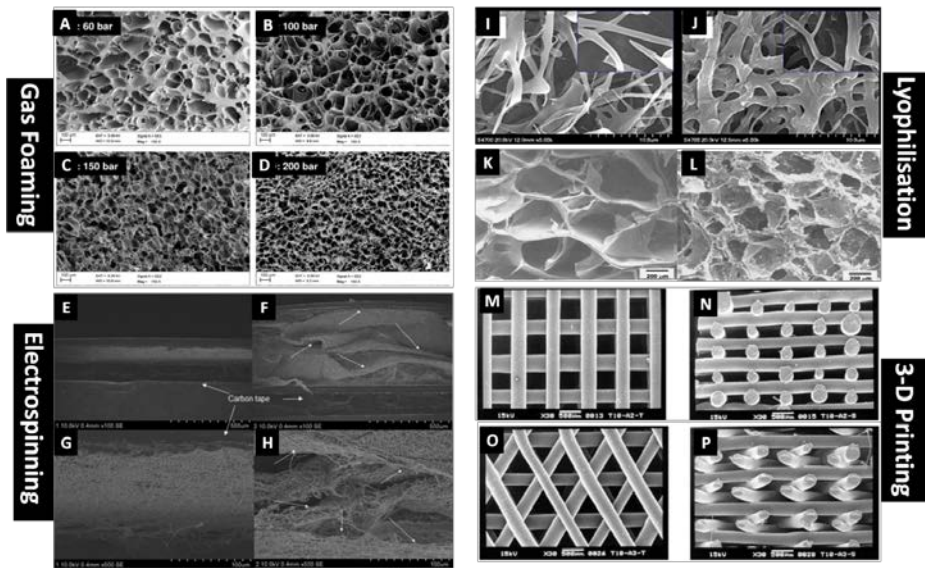


**Figure 1.7 Fabrication methods for complex macroporous scaffolds.** From (A) to (D) shows the SEM images of a scaffold fabricated with gas foaming technique. The image is taken along the foaming direction and foam specimens prepared at pressures (A) 60, (B) 100, (C) 150, and (D) 200 bar.<sup>[96]</sup> All other conditions held constant T  $\frac{1}{4}$  40C, ST  $\frac{1}{4}$  30 min, and VT  $\frac{1}{4}$  12 min. From (E) to (H) shows the SEM images of electrospun mat. (E) and (G) shows the pristine PCL electrospun sheet, whereas (F) and (H) shows sodium borohydride treated PCL electrospun sheet to yield a 3D scaffold.<sup>[113]</sup> Image (I) to (L) are the SEM images of scaffolds fabricated by lyophilization technique. Hyaluronic acid before (I) and after (J) EDC crosslinking.<sup>[109]</sup> Gelatin scaffolds with (L) and without (K) Hap nanoparticles.<sup>[111]</sup> Images from (M) to (P) shows SEM images of 3-D printed PCL scaffolds with different alignment. (M) and (O) are the top view of the scaffold and its respective side view are shown in (N) and (P).<sup>[106]</sup>

### 1.4.3 3D-printing methods

With recent advancements in technology, rapid prototyping is a new technique for fabricating scaffolds. The rapid prototyping technique, also known as the solid free-form technique, is controlled by computer [123]. The rapid prototyping technique uses CAD software and constructs scaffolds by stacking up layers. The advantage of this technique is structural variation of the scaffolds. *Miller et al.* printed 3D filament networks of biocompatible carbohydrate glasses as a template containing engineered tissue with living cells in order to create cylindrical networks that mimic ECM with vascular architecture and allow blood perfusion under high-pressure flow, providing another route for vascularization strategies. Furthermore, the rapid prototyping technique can control the mechanical properties of scaffolds by mixing different types of materials. Mixing different types of materials can not only improve mechanical strength but also add another function, such as drug delivery. *Kang et al.* created 3D hybrid scaffolds with a combination of hydrogels (as a cell based drug delivery system) and 3D framework scaffolds (to enhance their mechanical properties) in order to show the clinical applicability of releasing dopamine from 3D hybrid scaffolds encapsulating dopamine-

secreting cells [124]. Nevertheless, the precision and accuracy of scaffolds produced via a rapid prototyping technique are a major concern due to internal stress generated during the fabrication process [125]. Three rapid prototyping based techniques are 3D printing, selective laser sintering, and fused deposition modeling [126].

Nowadays, 3D printing technique is widely used in bone tissue engineering field. Advantages of using 3D printing to manufacture scaffolds are customized sizes and shapes and minimizing volume usage [127-129] (Figure 1.8). The 3D dataset, which is obtainable from CAD software, is essential for fabricating scaffolds using 3D printing technique. Since this technique uses the layer by layer system to build scaffolds, 3D dataset needs to be converted into 2D data [130]. *Kantaros et al.* used P430 ABS model materials to fabricate scaffolds using PTC Pro Engineer™ CAD/ CAM software [131]. The average porosities of scaffolds using 3D printing method are 82%. *Kao et al.* coated polydopamine, which is effective in regulating cell adhesion, cell growth, and differentiation, onto the 3D printed poly (lactic acid) scaffold and examined osteogenic differentiation in cells [133].

Selective laser sintering is another type of rapid prototyping technique. Selective laser sintering uses a laser beam to sinter powdered materials. This technique, like other rapid prototyping techniques, fabricates scaffolds in layer by layer method [134]. During selective laser sintering process, laser selectively scans over the surface of powdered materials and raises the temperature of the beam to the melting point of powdered materials, sintering powdered particles [135]. At the end of layering, the new powdered material is deposited on top of the sintered materials [136]. *Ferretti et al.* used selective laser sintering technique to manufacture PCL scaffolds [137]. The operating system of selective laser sintering was fifty Celsius degree of powder bed temperature, fifty Celsius degree lateral feed pistons temperature, 12 W laser power, and 0.1 millimeters layer of thickness. The porosity of fabricated scaffold was founded to be 47.66%, and compression strength to be 3.6 MPa. *Du et al.* used various intensities of laser beams to build PCL, 10% HA/PCL, and 20% HA/PCL scaffolds [138]. The average porosities range of PCL, 10% HA/PCL, and 20% HA/PCL are from 65.0% to 70.4%. In addition, porosity differences among three different types of scaffolds were negligible. Nevertheless, compressive modulus was decreased as the

concentration of HA was increased. The compressive modulus of PCL scaffold was determined to be the highest, 3.1 MPa, while compressive modulus of 20% HA/PCL scaffold was the lowest, 1.6 MPa. Fused deposition modeling is more tractable than other rapid prototyping techniques, and does not require solvents [139]. Fused deposition modeling technique manipulates an extruder to eject thermoplastic filament materials and laying semi-molten polymer on a platform in layers [140]. The next layer of semi-molten polymer is deposited when a base platform is lowered at the end of each layer phase.

In this process, designed scaffold is fabricated. *Zein et al.* used the fused deposition modeling technique to fabricate PCL, Polycaprolactone. The range of scaffold diameter was from 260 micrometers to 370 micrometers, the range of scaffold pore sizes was founded to be from 160 micrometers to 700 micrometers. Furthermore, the range of porosity was 48-77%. The mechanical property of scaffolds, which were fabricated through fused deposition modeling technique, was similar to the mechanical property of conventional scaffolds. *Kalita et al.* used both polymer and ceramic to build polymer-ceramic scaffolds by fused deposition modeling technique [141]. Average channel sizes of polymer-

ceramic scaffolds were 160 micrometers. Measuring mechanical properties of scaffolds, *Kalita et al.* found that scaffolds with the porosity of thirty-six percent had the highest compression strength.

#### **1.4.4 Lyophilization methods**

The lyophilization technique uses the sublimation process of the solvent to design scaffolds. A polymer is dissolved in a solvent at a desired concentration. Then, the desired concentration of a solution is frozen and freeze dried. The porosities of scaffolds can be controlled via the rate of freezing [142]. The characteristics of freeze-dried scaffolds are 1) high porosity and 2) interconnectivity. Furthermore, scaffolds constructed through a lyophilization process have three-dimensional porosity [14]. *Cuadros et al.* prepared scaffolds using a lyophilization method and stated that the average porosity of calcium alginate/gelatin scaffolds was  $97.26\pm 0.18\%$  and the average Young's modulus was  $4054.4\pm 194$  KPa. [143]. *Kim et al.* used the freeze-drying method to construct hydroxyapatite/gelatin foams. The average porosities of gelatin, 10% HA/gelatin, and 30% HA/gelatin foam were  $89.8\pm 1.8$ ,  $87.5\pm 2.2$ , and

84.6±2.5%, respectively [144]. As the concentration of hydroxyapatite increased, the porosities of gelatin foams decreased. The elastic modulus of dried gelatin, 10% HA/gelatin, and 30% HA/gelatin foam were 0.86±0.19 MPa, 2.28±0.10 MPa, and 4.01±0.39 MPa, respectively.

### **1.4.5 Electrospinning methods**

The electrospinning technique uses high electrical force to construct nanofibers. Since interactions between the polymer solution and electrical force are key to the electrospinning system, an electrical field is generated by connecting one electrode to the polymer solution and connecting another electrode to a collector screen. The polymer droplets at the tip of the pipette elongate to form a Taylor cone, which is a conical shape, as electrostatic force increases, and when the electrostatic force of the polymer solution exceeds the surface tension of the polymer droplets, charged polymer solution extrudes from the pipette [145]. The solvent of the polymer is evaporated as it moves to the ground collector in a whipping movement. The structural benefits of nanofibrous scaffolds manufactured by the electrospinning technique are high porosity and a

large surface area to volume ratio, which resembles natural extracellular matrix [146]. *Yang et al.* manufactured menthol/PLLA nanofiber scaffolds using an electrospinning technique and the porosities of the scaffolds were found to be greater than 95% [147]. Interestingly, as the concentration of menthol in the scaffolds increased, the surface areas of the scaffolds decreased and the porosities of the scaffolds increased. The mechanical strengths of 10%, 15%, and 20% menthol/PLLA (wt %) scaffolds were measured as  $73.04 \pm 0.43$ ,  $60.43 \pm 0.99$ , and  $54.86 \pm 0.87$  kPa, respectively. As concentration of HA increased, the elastic modulus increased. Scaffolds fabricated through electrospinning techniques can also help regenerate skin layers. *Chong et al.* made electrospun PCL/gelatin nanofibrous scaffolds for skin healing. Electrospun PCL/gelatin scaffolds have a diameter of  $470 \pm 120$  nm and a porosity from approximately 62% to 75% [148].

#### **1.4.6 Biomimetic scaffold fabrication approaches**

In addition to designing scaffolds with ceramic materials, researchers have focused on designing biomimetic surfaces to mineralize the

scaffolds and dictate osteogenic differentiation of stem cells. In natural bone, carbonated apatite gets deposited on collagen I fibrils, forming a nanocrystalline anisotropic fibril [149]. Many anionic proteins in the bone matrix serve as initiators and inhibitors for carbonated apatite and control the deposition [150]. Taking cues from nature, researchers focused on incorporating anionic groups in the polymeric network. *Tanahashi et al.* studied six different types of functional groups (-CH<sub>3</sub>, -PO<sub>4</sub>H<sub>2</sub>, -COOH, -CONH<sub>2</sub>, -OH, and -NH<sub>2</sub>) on self-assembled monolayers of alkane thiols and found that the -PO<sub>4</sub>H<sub>2</sub> and -COOH groups were the most powerful at inducing mineralization. Negatively charged species were more potent at inducing mineralization. The neutral methyl group did not show any mineralization. It can be understood that the apatite formation is calcium ion induced complexation as the positively charged species showed less mineralization when compared to the negative counterparts [151]. *Benoit et al.* demonstrated this effect in a 3D environment by tethering different groups in a PEG hydrogel system and found that the added phosphate group regulated stem cells to an osteoblastic lineage, as OPN secretion increased with an increasing concentration of the phosphate group [152]. Similarly, *Deepthi et al.*

modified the surface of the polymer using plasma treatment. Electrospun scaffolds were plasma treated using nitrogen and argon gases, and new functional groups were introduced onto the electrospun membrane. This modification has positively affected osteogenic differentiation with increased ALP activity and biomineralization as studied by alizarin red staining [153]. Recently, *Kim et al.* showed a sulfated group is osteogenically favorable. Chondroitin sulfate (CS)/PEG hydrogels showed that increasing concentrations of CS increased mineralization and favored osteogenic differentiation. Furthermore, 10% CS incorporated PEG hydrogels showed enhanced bone formation in a cranial defect model [154]. These studies indicate that surface functionalization has an effect on stem cell behavior and that it can be positively tuned by osteogenic differentiation.

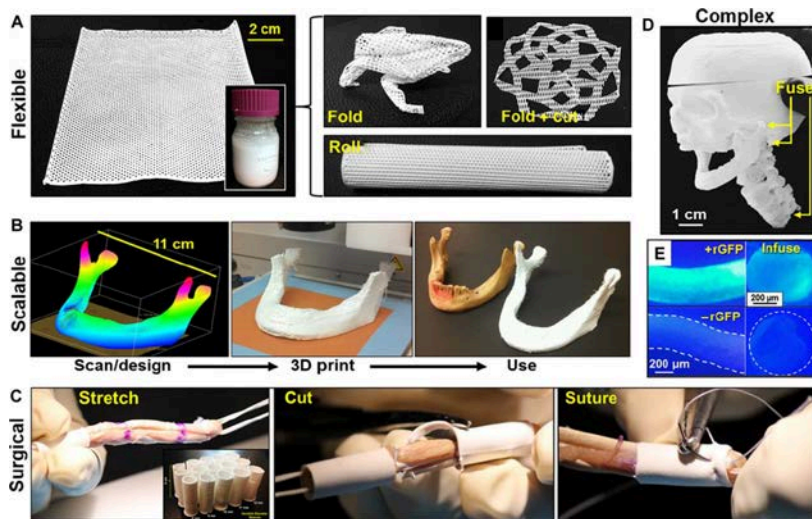


**Figure 1.8** Versatility, scalability, and manipulation of 3D-printed HB. (A) Easy to synthesize volumes (~100 ml shown) of liquid-based HB inks (inset) can be 3D-printed into a variety of structures: 3D-printed 12 × 12-cm HAPLGA sheet comprising three layers, which can be manipulated in a variety of ways, including rolling, folding, and cutting. Origami methods may be used to create complex folded structures, whereas kirigami methods can produce complex structures from strategic folding and cutting. (B) Full-scale, anatomically correct parts, such as a human mandible, comprising >250 layers, can be designed, 3D-printed from HAPLGA, and washed to rapidly produce a ready-to-implant object. Final image shows 3D-printed mandible next to an adult cadaveric human mandible. (C) Photograph series illustrating that custom-sized HAPLGA sleeves can be snugly stretched around, cut, and sutured to a soft tissue, such as human cadaveric tendon, facilitating arthroscopic ACL repair and replacement surgery. (D) Independently 3D-printed HAPLGA miniature-scale versions of a human skull, skull cap, mandible, and upper thoracic seamlessly fused together to create highly complex structures by using HB ink applied to points of contact. (E) Black light-illuminated optical photographs of the outside and internal cross sections of HAPLGA fiber with (top) and without (bottom) incorporated recombinant green fluorescent protein (rGFP).<sup>[96]</sup>

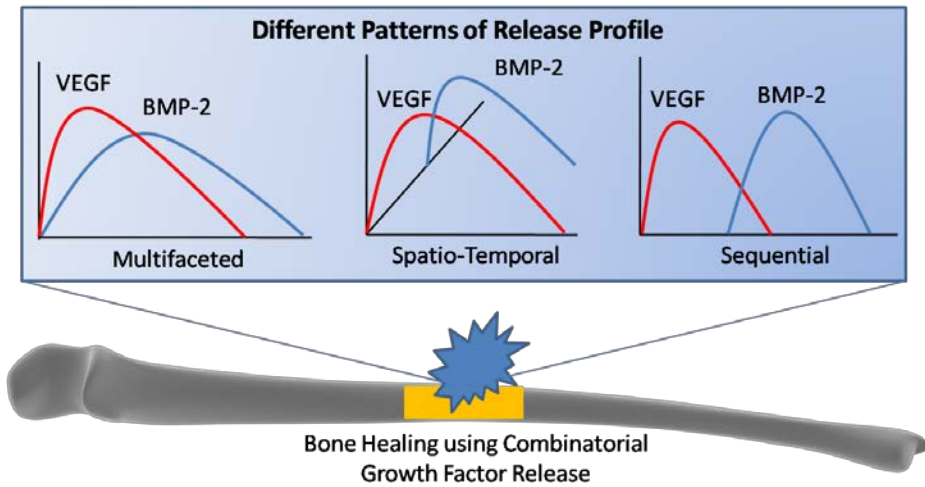


**Figure 1.9** Different growth factor delivery design for dual or multiple growth factor delivery system for bone regeneration. BMP-2 and VEGF given as an example for dual growth factor delivery and it is not limited to them.

## **1.5 Combined effects of growth factors and scaffolds design for bone regeneration**

A multi-functional delivery system or multi-growth factor delivery is more promising than other alternatives because tissue regeneration is a complex process, orchestrating many biological cues at appropriate concentrations and times (Figure 1.9). Looking at bone tissue repair at a molecular level, it is a tightly regulated process by the expression of various bioactive factors [155]. Right after injury, there is a profound increase in pro-inflammatory cytokines and growth factors, such as interleukin (IL)-1, IL-6, tumor necrosis factor (TNF)- $\alpha$ , platelet derived growth factor (PDGF), and TGF- $\beta$ . After the inflammatory phase, other growth factors for matrix secretion, such as BMP, IGF, TGF- $\beta$ , and VEGF, are secreted [155-157]. Even though VEGF may not play a direct role in osteogenesis, it is required during the cartilage mineralization phase and in neo-angiogenesis [158]. Although the tissue repair is not fully elucidated, with the available knowledge, researchers have focused on dual or multiple factor delivery, and tuning the delivery rate to match the natural cascade in tissue would be a promising biomimetic approach.

One of the most widely used growth factors in bone tissue engineering is the bone morphogenetic protein (BMP) family, which regulates the osteogenic differentiation of mesenchymal stem cells via the SMAD signaling pathway [159-161]. In particular, *Oest et al.* fabricated poly(L-lactide-co-D, L-lactide) scaffolds with BMP-2 and TGF- $\beta$ 3 and implanted the scaffolds into an 8-mm rat segmental defect model [162]. They confirmed that the group of scaffolds with BMP-2 and TGF- $\beta$ 3 showed enhanced bone formation compared to the control group. Recently, the combination of biodegradable polymer scaffold, calcium phosphate compounds and growth factors related to bone formation was utilized to regenerate bone tissue effectively in an *in vivo* model [163, 164]. In particular, the sustained release of growth factors in polymer scaffolds is currently the key point of this research [60, 165]. The effects of BMP on the osteogenic commitment of stem cell depends on the cell size, shape, cytoskeletal tension mediated through integrin-ECM interactions, and growth conditions. We previously demonstrated that the effect of BMP on stem cells diverges depending on whether the cells are in 2D vs 3D [166].

*Subbiah et al.* developed osteogenic and angiogenic growth factors that deliver microcapsules and studied bone formation in a rat calvarial defect. Combinatorial delivery of VEGF (3  $\mu$ g) and BMP-2 (3  $\mu$ g) resulted in enhanced bone formation and vasculature [167]. *Cao et al.* developed BMP2 and VEGF loaded sulfated chitosan nanoparticles embedded in gelatin sponge for rabbit femur bone regeneration. There was profound enhancement in bone regeneration in combinational therapy compared to BMP-2 alone [168]. *Park et al.* developed a 3D printed scaffold containing VEGF and BMP-2 for spatiotemporal release. They fine-tuned the delivery system in such a way that BMP-2 is released slowly and VEGF is released rapidly. Additionally, BMP-2 was loaded in the periphery of the scaffold, where contact with the existing bone was high, and VEGF was loaded in the middle part of the scaffold, where hypoxia was expected to happen, thereby controlling the delivery of GFs spatio-temporally. The scaffolds were implanted subcutaneously in a mouse model and assessed for blood vessel and bone formation. Even in the large implanted scaffold, blood formation was seen in the middle to periphery of the scaffold [169]. For a better understanding of these results, the study must be conducted in orthotropic models. *Kempen et*

*al.* developed a composite scaffold for the sequential release of VEGF and BMP-2 for bone regeneration. The authors claim to mimic the natural bone healing cascade in which VEGF is highly expressed in the starting phase and BMP-2 is required in the latter stage of bone healing. An *in vivo* orthotropic model did not show enhanced bone healing with dual growth factors when compared to BMP-2 alone, even though the subcutaneous model showed benefits [170]. This result was possible as they used a high dose of BMP-2 (9.2  $\mu\text{g}$ ) per defect to see any beneficial effects. Similarly, *Young et al* [171] and *Patel et al* [172] did not find enhanced bone formation for BMP-2/VEGF dual GF delivery in comparison to BMP-2 alone. Hence, it is necessary to select appropriate GFs and doses, the experimental duration of the study, and the delivery method to assess the benefits of dual GF delivery.

Moreover, *Lu et al.* utilized bone formation enhancing technology using solid material and various growth factors with platelet rich plasma (PRP) [158]. PRP is known as a growth factor that contains a number of autologous thrombocytes that increase bone regeneration. Additionally, growth factors that are produced by platelets are crucial during granulation. For example, platelet derived growth factor (PDGF)

promotes the induction of osteoblastic precursors. In addition, transforming growth factor  $\beta$ -1 (TGF- $\beta$ 1) promotes cellular proliferation and collagen synthesis by osteoblast precursors. These factors cooperate with each other to stimulate osteogenesis inside our body. Recently, PRP hydrogels have been used in maxillofacial surgery bone grafting procedures by adhesion with cancellous bone particles in oral surgery [173]. Therefore, it is important to apply scaffold designs that elicit the desired growth factor effects.

## **1.6 Cell sources**

After designing a biocompatible porous structure in three dimensions, a selection of appropriate cell sources is another essential factor. Criteria for identifying reliable cell sources include non-immunogenicity, feasible cell expansion, and appropriate protein expression at defect sites [174]. There is enormous potential in stem cells due to their high proliferation capability, self-renewal and multi-lineage differentiation for bone tissue engineering [175]. Embryonic stem cells (ES) or induced pluripotent stem cells (iPSCs) can give rise to three germ layers: the

ectoderm, endoderm, and mesoderm. The ease of expanding cell numbers from pluripotent cells is one of the merits of many applications, yet researchers are still struggling to differentiate these cells into a homogenous population expressing valid protein patterns without acquiring tumorigenic characteristics. In this sense, mesenchymal stem cells (MSCs) are more suitable progenitor cells for tissue repair than other stem cells. MSCs isolated from patients can expand and differentiate into skin, bone, cartilage, muscle, tendon, ligament, adipose and connective tissues [176]. Among several places to derive MSCs, the most enriched source of MSCs is bone marrow. *Friedenstein et al.* discovered for the first time that clonogenic fibroblast precursor cells (CFU-F), or MSCs, could be isolated from white bone marrow and give rise to bone- and cartilage-like colonies [177]. However, the heterogeneity of bone marrow requires several steps to isolate MSCs from other cells, such as endothelial cells and hematopoietic stem cells. Methods for isolating MSCs range from simple aspiration or density-gradient centrifugation [178] to specific marker selection. *Gronthoset al.* reduced heterogeneity by isolating cells expressing STRO-1, a trypsin-resistant cell surface marker, and showed that these selected populations

exhibited adherent, high growth potential and CFU-F characteristics that eventually differentiated into fibroblastic, adipogenic, myogenic and osteogenic lineages [179]. In particular, STRO-1 selected populations that underwent osteogenic differentiation possessed alkaline phosphatase, leading to mineralization of tissue both *in vitro* and *in vivo* [180]. Leukocyte-cell adhesion molecule reacting with surface antigen SB-10 acts as a cell adhesion molecule during osteogenesis but is terminated after mesenchymal differentiation [181]. There is still controversy about identifying MSCs from various sources, but the minimum criteria of MSCs are defined as follows: (1) having an adherent-plastic culture *in vitro*; (2) expressing CD105, CD73, and CD90; (3) lacking CD11b, CD14, CD34, and CD45; and (4) differentiating into osteoblasts, chondrocytes and adipocytes [182]. Along with their differentiation potential, MSCs can expand *in vitro* without losing their multipotent characteristic, even after several passages [183]. Since the number of MSCs acquired from a donor is approximately 100,000 nucleated cells per donation [184], the expandable ability of MSCs is beneficial in complementing a low number of endogenous progenitor cells for clinical implantation.

Depending on microenvironment conditions, MSCs can commit to a specific mesenchymal lineage. To direct MSCs into an osteogenic lineage, MSCs in *in vitro* monolayer culture are incubated in a combination of dexamethasone (Dex),  $\beta$ -glycerophosphate ( $\beta$ -GP), and ascorbic acid (AA). Along the osteogenic pathway, osteoprogenitor cells require glucocorticoids for proliferation and differentiation. Dex is a synthetic glucocorticoid that stimulates the proliferation capacity of osteoprogenitor cells and produces daughter osteoprogenitor cells to continuously express bone nodule and phenotype in physiological conditions [185].  $\beta$ -GP induces mineralization by being rapidly hydrolyzed by alkaline phosphatase (ALP), resulting in an increased number of local phosphate ions [186]. In mineralized conditions, Dex activates to form calcium phosphate deposition, which can be detected by alizarin red staining and von Kossa staining [187]. Without  $\beta$ -GP, osteoprogenitor cells have enhanced proliferation rates and present higher ALP activity, but they lack further osteogenic differentiation and exhibit incomplete expression of the osteoblast phenotype [187]. AA is involved in collagen synthesis by reducing the iron prosthetic group of hydroxylase and accumulating bone extracellular matrix from collagen

synthesis, eventually influencing high ALP activity and mineralization [188]. In culture conditions, AA is stable in the form of ascorbic acid 2-phosphate, upregulating gene expressions related to the cell cycle, mitosis and collagen synthesis [189]. The synergistic effect of Dex,  $\beta$ -GP, and AA enables MSCs to differentiate into an osteogenic lineage, proliferate into osteoblasts and embed terminally differentiated osteoprogenitor cells in a mineralized matrix. To enhance osteogenesis upon using Dex,  $\beta$ -GP, and AA, several growth factors can be utilized to optimize the process of bone maturation and mineralization. For example, in the early stage of osteogenesis, vascular endothelial growth factor (VEGF) and insulin-like growth factor-1 (IGF-1) play a role in cell proliferation, whereas fibroblast growth factor basic (FGF-2) and bone morphogenetic protein-2 (BMP-2) are expressed in the later stage of osteogenesis, cell differentiation and the maturation stage [190]. Additionally, transforming growth factor- $\beta$ 1 (TGF- $\beta$ 1), one of three TGF- $\beta$  isoforms, is known to manage bone formation by both synthesizing and degrading bone matrix components, including collagen type I [191].

## **1.7 Summary**

In bone tissue engineering, it is important to create microenvironments for cells to differentiate into complete bone tissue. For successful bone tissue regeneration, a variety of materials has been investigated to fabricate optimal scaffolds. Many biocompatible and biodegradable polymers have been explored to make bone scaffold frames, and osteoinductive materials, such as metal ions and growth factors, have been incorporated into bone scaffolds. Furthermore, various techniques have been developed to construct the 3D porous bone scaffolds similar to natural bone tissue. These traditional strategies have been innovated for years, and various cell sources optimized for osteogenesis have been applied to bone tissue engineering. In this way, we expect to overcome current challenges and critical-sized bone defects from accidents and diseases.

## **2 CHAPTER TWO: BIOMIMETIC**

### **WHITLOCKITE INORGANIC**

### **NANOPARTICLES-MEDIATED IN SITU**

### **REMODELING AND RAPID BONE**

### **REGENERATION**

#### **2.1 Introduction**

Natural hard tissues continuously maintain a healthy state throughout life by self-regenerating their micro-damaged parts through a bone remodeling process [192-200]. At the initiation of bone remodeling process, osteoclast precursors migrate from blood vessels to the bone by chemorepulsion [192, 193]. Then, osteoclasts form a sealing zone with ruffled borders and inorganic minerals are degraded by protons supplied through H<sup>+</sup>-transporting adenosine triphosphate (H<sup>+</sup>-ATPase) [194, 200, 201]. In addition, organic bone matrices are further resorbed by proteinase, such as cathepsin K, in an acidic pH condition [195, 202, 203]. Recent evidences showed that these resorption processes are necessary

for successful bone formation as resorbed components along with activated osteoclasts sequentially drive endogenous stem cells functions, where activated stem cells ultimately contribute to a new bone tissue [196-199].

Recently, synthetic matrices emulating the physiochemical properties of bone tissues are being developed to control stem cell fate. Biomaterials containing calcium phosphate moieties, such as hydroxyapatite (HAP:  $\text{Ca}_{10}(\text{PO}_4)_6(\text{OH})_2$ ), have been shown to induce osteogenic differentiation of stem/progenitor cells and bone tissue formation. However, the participation of inorganic minerals during the bone regeneration and remodeling processes has not been fully elucidated. During the bone remodeling process, the acidic environment created by osteoclasts mobilizes pre-existing minerals that have a similar phase with HAP.[194, 200] HAP gets resorbed as the local pH inside the sealing zone of osteoclasts and macrophages is approximately 3~4.5 [194, 201]. Recent evidences suggest that one of the main components of inorganic phase of bone is whitlockite (WH:  $\text{Ca}_{18}\text{Mg}_2(\text{HPO}_4)_2(\text{PO}_4)_{12}$ ). Even though WH a relatively rare mineral in nature, it is the second most abundant mineral in human bone with

approximately upto 20 wt%, and it is particular found in bone with elevated dynamic loading [204]. Whitlockite is a mineral with an unusual form of calcium phosphate with unknown biological role. Based on its physiochemical properties, WH has unusual form of calcium phosphate and it is very different than its synthetic analogue  $\beta$ -tricalcium phosphate ( $\beta$ -Ca<sub>3</sub>(PO<sub>4</sub>)<sub>2</sub>) [205, 206]. Furthermore, unlike HAP, WH is relative stable in acidic condition. The increased detection of short micro-ranged WH in bone under increased loading along with its acidic stability suggests that it may act as an inorganic template composition for further mineralization. In addition, elevated composition of WH in adolescent's bone suggest that it may be actively involved in bone remodeling process [207, 208].

Here, we investigated the role of WH on bone remodeling and formation. WH nanoparticles were synthesized, and we demonstrate that the synthetic WH can recapitulate early-stage bone regeneration *via* elevated extracellular PO<sub>4</sub><sup>3-</sup> and Mg<sup>2+</sup> concentration as well as inhibition of osteoclastic differentiation. Furthermore, our studies showed that WH participates in bone formation *via* increased affinity with extracellular proteins. Finally, we demonstrated that the WH

containing scaffold platform could stimulate through phase transformation *in vivo* bone formation. The multidisciplinary approach conducted in this study provided an organized methodology to find biological functionalities of WH and introduced a useful clinical application.

## **2.2 Materials and methods**

### **2.2.1 Material preparation**

To synthesize whitlockite (WH:  $\text{Ca}_{18}\text{Mg}_2(\text{HPO}_4)_2(\text{PO}_4)_{12}$ ) nanoparticles, 0.37 M calcium hydroxide ( $\text{Ca}(\text{OH})_2$ , 99.0%, High Purity Chemical, Japan) and 0.13 M magnesium hydroxide ( $\text{Mg}(\text{OH})_2$ , 95.0%, Junsei Chemical Co., Japan) were initially mixed in distilled water at 80 °C. While vigorously stirring, 0.5 M phosphoric acid ( $\text{H}_3\text{PO}_4$ , 85.0%, Junsei Chemical Co., Japan) was added into the  $\text{Ca}(\text{OH})_2$  and  $\text{Mg}(\text{OH})_2$  mixed solution with a speed of 12.5 ml/min using a distal burette (Metrohm 876, Dosimat Plus). After two days of sufficient aging, the precipitant was collected with a filter press method using a 0.22- $\mu\text{m}$  membrane (Durapore<sup>®</sup> membrane filters, Millipore) and freeze-

dried. In addition, to grow the size of the WH nanoparticle, WH was synthesized with a similar process as described above while the temperature was constantly maintained at 65 °C. After two months of the aging process to induce a sufficient size, enlarged WH particles up to 200 nm were collected. To synthesize hydroxyapatite (HAP:  $\text{Ca}_{10}(\text{PO}_4)_6(\text{OH})_2$ ) nanoparticles, 0.3 M  $\text{H}_3\text{PO}_4$  was added into 0.5 M  $\text{Ca}(\text{OH})_2$  with a speed of 12.5 ml/min, while applying sonication during the entire process to induce a complete reaction between starting materials. HAP was also collected with a filter press method and freeze-dried.

### **2.2.2 Scaffold fabrication**

A cylindrical ceramic pellet was made in a metal mold after applying two tons of pressure for three seconds. WH and HAP pellets were sintered at 700 °C for 2 hours with a 5 °C/min heating rate. To make similar surface roughness levels, ceramic pellets were polished by 220 grit SiC sandpaper. After the fabrication process, ceramic pellets were washed in

distilled water several times with sonication to remove any residual impurities.

### **2.2.3 Material characterization**

The crystal phase of the material was confirmed by X-ray diffraction (XRD, New D8 Advance, Bruker) with monochromatic Cu K $\alpha$  radiation ( $\lambda=1.5405$  Å). Morphologies of nanoparticles were observed by field emission scanning electron microscopy (FESEM, SUPRA 55VP, Carl Zeiss) after platinum coating with a sputter (Sputter Coater, BAL-TEC/SCD 005). To obtain a bright field image and diffraction pattern of WH, 200 nm sized WH nanoparticles were fully dispersed in ethanol and loaded on a 100-mesh TEM copper grid (FCF-100-cu, Electron Microscopy Sciences). Enlarged WH particles were used for TEM analysis because nanoparticles with small sizes were vulnerable to beam damage. Additionally, it was easier to separate single nanoparticles as the size of the particles became larger. Three-dimensional images of a single particle of WH were obtained by field emission transmission electron microscope (FE-TEM, JEM-2200FS, JEOL). To analyze the

surface chemistry of WH, X-ray photoelectron spectroscopy (XPS, PHI 5000 VersaProbe™, ULVAC-PHI) was utilized. CasaXPS software (version 2.3.16, Casa Software Ltd) was used to calibrate XPS spectra based on the C 1s peak (284.8 eV) as a charge reference. To calculate the element composition, background lines of peaks were obtained by Shirley's method and Relative Sensitivity Factors (RSF) of Ca<sub>2s</sub> (0.47), Mg<sub>2s</sub> (0.2) and P<sub>2s</sub> (0.29) were referred to the previous literature [209]. The surface roughness of the ceramic pellet was measured by Atomic Force Microscopy (Multimode 8, Bruker), using a high sensitivity silicon nanoprobe tip (RTESPA, Bruker). To analyze the crystal phase of the bone mineral, which was newly precipitated in a chondroitin sulfate (CS) gel implant during the *in vivo* test, flower-like bone minerals were separated with a focused ion beam (Helios Nano Lab 600, FEI) and placed on a TEM copper grid. Bright field images and diffraction patterns of new bone mineral were analyzed by High Resolution TEM (Tecnai F20, FEI).

## **2.2.4 Crystal morphology reconstruction**

The crystal habit of WH was simulated by a crystal morphology-building program WinXMorph™ (Version 1.54) [210, 211]. The atomic arrangement of WH surrounded by {012} planes was drawn using the CrystalMaker program (CrystalMaker Software Ltd., Oxford, England), based on the previously reported crystal structure of WH [212].

### **2.2.5 Ion release measurement**

Before measuring the ion release level of nanoparticles, both WH and HAP were vigorously washed in distilled water five times to remove resident ions at the surface. After drying, 1 wt% of WH (n=4) and HAP (n=4) aqueous solutions were aged on the shaker for one day and till four week at room temperature. To collect filtrate, solutions were first centrifuged at 4,000 rpm for 30 min and also filtered through a syringe membrane with 200 nm sized pores (Acrodisc®). Amounts of Ca, Mg and P ions in filtrates were measured with an inductively coupled plasma atomic emission spectrometer (ICP-AES, OPTIMA 8300, Perkin-Elmer, USA) with argon plasma.

## **2.2.6 Zeta potential analysis**

Human tonsil-derived mesenchymal stem cells (hTMSCs) were isolated from patients with informed consent at Ewha Womans University Medical Center, Seoul, Korea. hTMSCs were maintained in Dulbecco's modified Eagle's medium (11995, Gibco, Grand Island, NY) with 10% FBS (US1520, Biowest, Nuaille, France), 100 units/mL penicillin-streptomycin (15140, Gibco, Grand Island, NY) and 100 units/mL antibiotic-antimycotic (15240-062, Gibco, Grand Island, NY) at 37 °C with 5% CO<sub>2</sub>. For differentiation, we have used 1% of dexamethasone (Sigma), 1% of 2-Phospho-L-ascorbic acid trisodium salt (Sigma), and glycerophosphate disodium salt hydrate (Sigma). Raw 264.7 cells were purchased from the Korean Cell Line Bank (KCLB), Seoul, Korea. Raw 264.7 were maintained in Dulbecco's modified Eagle's medium (11995, Gibco, Grand Island, NY) with 10% FBS (US1520, Biowest, Nuaille, France), 100 units/mL penicillin-streptomycin (15140, Gibco, Grand Island, NY). For differentiation, we have used in Essential Medium Eagle Alpha modified medium ( $\alpha$ -MEM; Gibco, Grand Island, NY) supplemented with

penicillin and streptomycin, and cultured with or without 100 ng/mL of recombinant mouse RANKL (Abcam, USA).

### **2.2.7 Protein adsorption analysis**

Protein adsorption was measured by incubation in a solution containing 1 and 0.1 mg/ml of Bovine Serum Albumin (BSA, New England Biolabs Inc.) and PureCol<sup>®</sup> (Advanced Matrix), which was constantly rotated to ensure good mixing. Upto two hours of incubation at 4°C allowed sorting of WH or HAP cylindrical scaffolds from the BSA and type I collagen solution (PureCol<sup>®</sup>, Bovine Collagen, Advanced BioMatrix, Inc., USA). Repeating the above steps at least five times ensured that there was protein remaining. After rinsing, the adsorbed proteins were removed by addition of 1% SDS (Bio Rad<sup>□</sup>, USA) from the powder or cylindrical scaffolds. The amount of various proteins adsorbed on scaffolds was quantified by a modified Bradford protein assay using Bio-rad Assay kit<sup>®</sup> by Infinite<sup>®</sup> 200 Pro microreader (Tecan<sup>™</sup>, USA).

## 2.2.8 Cell culture

Human tonsil-derived mesenchymal stem cells (hTMSCs) were isolated from patients with informed consent at Ewha Womans University Medical Center, Seoul, Korea. hTMSCs were maintained in Dulbecco's modified Eagle's medium (11995, Gibco, Grand Island, NY) with 10% FBS (US1520, Biowest, Nuaille, France), 100 units/mL penicillin-streptomycin (15140, Gibco, Grand Island, NY) and 100 units/mL antibiotic-antimycotic (15240-062, Gibco, Grand Island, NY) at 37 °C with 5% CO<sub>2</sub>. For differentiation, we have used 1% of dexamethasone (Sigma), 1% of 2-Phospho-L-ascorbic acid trisodium salt (Sigma), and glycerophosphate disodium salt hydrate (Sigma). Raw 264.7 cells were purchased from the Korean Cell Line Bank (KCLB), Seoul, Korea. Raw 264.7 were maintained in Dulbecco's modified Eagle's medium (11995, Gibco, Grand Island, NY) with 10% FBS (US1520, Biowest, Nuaille, France), 100 units/mL penicillin-streptomycin (15140, Gibco, Grand Island, NY). For differentiation, we have used in Essential Medium Eagle Alpha modified medium ( $\alpha$ -MEM; Gibco, Grand Island, NY) supplemented with

penicillin and streptomycin, and cultured with or without 100 ng/mL of recombinant mouse RANKL (Abcam<sup>□</sup>, USA).

### **2.2.9 Immunostaining**

Immunofluorescence staining was performed following standard protocol. Cells were fixed with 4% paraformaldehyde (6506-4405, Daejung, Korea) for 15 minutes. After washing with PBS, the samples were permeabilized with 0.1% Triton-X100 (X100, Sigma-Aldrich, MO, USA) in PBS for 15 minutes. For cell adhesion and morphology analysis, cells were stained with Alexa Fluor<sup>®</sup> 488 or 594 Phalloidin (Invitrogen<sup>™</sup>, Carlsbad, CA, USA), which was diluted in PBS at a 1:100 ratios for 1.5 hours. After actin staining, DAPI (D9542, Sigma-Aldrich; St. Louis, MO, USA) was diluted in PBS at a 1:200 ratio and was treated for 10 minutes. For confirmation of collagen deposition, cells were primarily stained with collagen type I antibody (1:200, Fitzgerald) for 2 h. Samples were then incubated with secondary antibody against rabbit (1:500, Jackson Immuno Research) for 2 h. Samples were then imaged

with confocal laser scanning microscopy (Zeiss) and images were analyzed using ImageJ software (NIH, USA)

### **2.2.10 Cell viability and proliferation**

A LIVE/DEAD<sup>®</sup> cell viability kit (Invitrogen<sup>™</sup>, USA) was utilized to determine cell viability. Growth medium with 2  $\mu$ l calcein AM (component A) and 1  $\mu$ l ethidium homodimer-1 (component B) was used to treat samples and cells were incubated for 30 minutes for Live/Dead detection. To test the cell proliferation rate, a click-iT EdU Flow Cytometry Assay Kits (Invitrogen<sup>™</sup>, USA) was used according to the manufacturer's instructions. The cells on the HAP and WH cylindrical scaffolds were incubated with 0.18% EdU (5-methynyl-2'-deoxyuridine) for four hours. After cell fixation with 4% paraformaldehyde (6506-4405, Daejung, Korea) for 15 minutes, 1X Click-iT saponin-based permeabilization and wash reagent was added to the samples. Click-iT reaction cocktails were added to the samples for 30 minutes. The samples were washed with 1X- Click-iT saponin-based permeabilization

and wash reagent. To label total cell nuclei, DAPI staining was conducted after EdU staining.

### **2.2.11 Chemical staining**

Cells were fixed with a fixative solution (40  $\mu$ L citrate stock solution, Sigma-Aldrich, 1.96 mL distilled water and 3 mL acetone) for 1 min and washed with distilled water and stained for alkaline phosphatase (ALP; Sigma-Aldrich, USA) as previously described [213, 214]. In brief, a diazonium salt solution was prepared by dissolving 0.24 mg of Fast Blue RR Salt (Sigma-Aldrich, USA) in 1 mL of distilled water and adding 40  $\mu$ L of Naphthol AS-MX Phosphate solution (Sigma-Aldrich, USA). Cells were stained with a diazonium salt solution for 1 hour and washed twice with distilled water. For Alizarin Red S (ARS; Sigma-Aldrich, USA) staining, 20 mg of ARS was dissolved in 1 mL of distilled water and the pH was adjusted to 4.1~4.2 with ammonium hydroxide ( $\text{NH}_4\text{OH}$ ;  $\text{H}_5\text{NO}$ ; Daejung, Korea). Fixed cells were stained with ARS solution for 20 min and washed with distilled water twice. For tartrate-resistant acid phosphatase (TRAP) staining, we have used acid

phosphatase, leukocyte (TRAP) kit (Sigma, USA) according to manufacturer's protocol.

### **2.2.12 SiRNA transfection**

siRNA duplex targeted *SLC20a1*, *MagT1* and siRNA with scrambled sequences (medium GC contents) were synthesized by Shanghai GenePharma Co., Ltd (China). The volume of siRNA (3  $\mu$ l) was optimized and transient transfection was performed using a Lipofectamine 2000 (Invitrogen<sup>TM</sup>, USA) according to the manufacturer's protocol.

### **2.2.13 Gene expression profile**

Total RNAs were extracted from the cell-laden 2D cylindrical scaffolds (n=3) with Trizol (Trizol<sup>®</sup>, Life technology, USA), and reverse-transcribed into cDNA using the SuperScript Synthesis System (Invitrogen<sup>TM</sup>, USA). Real-time PCR reactions were performed using SYBR Green PCR Master-mix and human mesenchymal stem cell PCR

arrays (96 genes, SuperArray Bioscience) according to the manufacturer's instructions with the ABI StepOnePlus™ real-time PCR system (Applied Biosystems, USA). cDNA samples (2 µl for a total volume of 20 µl per reaction, 25 µl for arrays) were analyzed for the genes of interest (*B2M*, *HPRT1*, *RPL13A*, *GAPDH*, *ACTB* and *HGDC* for an array) where *GAPDH* was used as a reference gene. The level of expression of each target gene was then calculated as  $-2^{\Delta\Delta C_t}$ .<sup>[215]</sup> Each sample was repeated at least three times for the gene of interest. The PCR primers are listed in Table 2.1 and 2.2.

<b>Gene Over-Expressed in</b>			
<b>WH vs HAP Group</b>			
<b>Gene Symbol</b>	<b>Fold Regulation</b>		
		<i>ITGAX</i>	35.578
<i>ABCB1</i>	6.1441	<i>MCAM</i>	52.7221
<i>ACTA2</i>	10.4378	<i>MMP2</i>	2.0417
<i>ALCAM</i>	27.8669	<i>NGFR</i>	2.2433
<i>ANPEP</i>	15.2329	<i>NOTCH1</i>	10.954
<i>BDNF</i>	19.2253	<i>NT5E</i>	5.6999
<i>BMP2</i>	19.6467	<i>NUDT6</i>	10.9383
<i>BMP7</i>	2.0534	<i>PDGFRB</i>	16.8227
<i>CASP3</i>	21.4552	<i>PTK2</i>	3.9269
<i>CD44</i>	94.4453	<i>RHOA</i>	11.0036
<i>COL1A1</i>	9.8041	<i>RUNX2</i>	77.7535
<i>CSF3</i>	51.707	<i>SLC17A5</i>	53.6799
<i>EGF</i>	4.0479	<i>SMAD4</i>	2.172
<i>ENG</i>	13.5595	<i>SMURF1</i>	4.8473
<i>FGF10</i>	16.4019	<i>SMURF2</i>	75.6585
<i>FGF2</i>	2.4784	<i>TGFB1</i>	6.6546
<i>FUT1</i>	3.2701	<i>TGFB3</i>	16.7713
<i>FZD9</i>	7.6693	<i>TNF</i>	5.7489
<i>GDF15</i>	32.0154	<i>VCAM1</i>	5.3742
<i>GDF5</i>	9.7968	<i>VEGFA</i>	2.154
<i>GDF7</i>	136.2605	<i>VIM</i>	102.8144
<i>GTF3A</i>	2.1848	<i>VWF</i>	4.4891
<i>HAT1</i>	2.6676	<i>ACTB</i>	214.1029
<i>HDAC1</i>	8.5933	<i>B2M</i>	4.0619

<i>HNF1A</i>	4.4825	<i>GAPDH</i>	7.953
<i>IGF1</i>	2.0638	<i>HPRT1</i>	6.098
<i>IL6</i>	6.9442	<i>RPLP0</i>	58.5813
<b>Gene Under-Expressed in</b>			
<b>WH vs HAP Group</b>			
<b>Gene Symbol</b>	<b>Fold Regulation</b>	<i>KITLG</i>	-5.5113
<i>BMP4</i>	-5.3865	<i>NES</i>	-2.5797
<i>IL1B</i>	-2.288	<i>POU5F1</i>	-2.4157
<i>INS</i>	-3.0087	<i>PROM1</i>	-2.689
<i>ITGB1</i>	-2.7162	<i>TERT</i>	-4.4442
<i>KDR</i>	-22.3218	<i>THY1</i>	-30.277

**Table 2.1** Mesenchymal gene expression of whitlockite (WH:  $\text{Ca}_{18}\text{Mg}_2(\text{HPO}_4)_2(\text{PO}_4)_{12}$ ) vs. hydroxyapatite (HAP:  $\text{Ca}_{10}(\text{PO}_4)_6(\text{OH})_2$ ) in hTMSC culture with 2D scaffolds. A total of 96 genes were tested with a SA bioscience Human Mesenchymal Stem Cell Array Kit and 12 genes were used as housekeeping genes.

<b>Gene</b>	<b>Primer 5'-3'</b>
<i>GAPDH</i>	F: CGC TCT CTG CTC CTC CTG TT R: CCA TGG TGT CTG AGC GAT GT
<i>ALP</i>	F: ACG TGG CTA AGA ATG TCA TC R: CTG GTA GGC GAT GTC CTT A
<i>Col 1</i>	F: GTC ACC CAC CGA CCA AGA AAC C R: AAG TCC AGG CTG TCC AGG GAT G
<i>OCN</i>	F: GCC TTT GTG TCC AAG C R: GGA CCC CAC ATC CAT AG
<i>RunX2</i>	F: ACT GGG CCC TTT TTC AGA R: GCG GAA GCA TTC TGG AA
<i>TRAP</i>	F: GCT GGA AAC CAT GAT CAC CT R: GCG GAA AGG TGG TAT CTC AA
<i>Cathepsin K</i>	F: CTT CCA ATA CGT GCA GCA GA R: CCT CTG CAT TTA GCT GCC TT
<i>NFTc1</i>	F: TGG AGA AGC AGA GCA CAG AC R: TCG GTT TCT TCT CCT CTG GA

**Table 2.2** Primer sets for human genes used in this study. *GAPDH* was used as a housekeeping gene. [Alkaline phosphatase (*ALP*), type 1 collagen (*Col 1*), osteocalcin (*OCN*), Runt-related transcription factor 2 (*RunX2*), *TRAP*, *Cathepsin K*, and *NFTc1*]

### **2.2.14 Western blot assay**

Hydrophobic protein lysates were collected with a Mem-PER Plus Membrane Protein Extraction Kit (89842, Pierce Chemical Co., USA) from T-MSC cells. Electrophoresis was carried out in a 10% SDS-polyacrylamide gel to detect  $\beta$ -actin and phosphate (*SLC20a1*) transporter by loading 40  $\mu$ g of the total protein per lane. Proteins were transferred to a nitrocellulose membrane by iBlot (Invitrogen<sup>TM</sup>, USA) and blocked by 5% Bovine Serum Albumin (#9998, Cell Signaling, USA) or 5% nonfat milk (#9999, Cell Signaling, USA) in 1x PBS-T (pH 7.5 with 0.1% Tween-20) for antibodies to  $\beta$ -actin and *SLC20a1*, correspondingly. As a loading control, the immune-blotted proteins were bound to a primary mouse monoclonal anti-  $\beta$ -actin antibody (#6276, Abcam<sup>□</sup>, USA) diluted in 1:5,000 at RT for two hours. To

detect primary antibody binding, an HRP-conjugated secondary goat anti-mouse antibody (170-5047, Bio Rad<sup>□</sup>, USA) was applied in a 1:17,500 dilution for one hour. For detection of SLC20a1, a membrane was incubated with rabbit monoclonal anti-SLC20a1 antibody (ab177147, RabMab, USA) diluted in a 1:1,000 ratio under gentle agitation at 4 °C overnight. Then, an anti-rabbit IgG HRP-linked antibody (#7074, Cell Signaling, USA) in a 1:2,000 dilution was applied at RT for 1 hr. Visualization of proteins was preceded by incubating the membrane in a 1:1 ratio of a luminol/enhancer solution from an Immun-Star<sup>TM</sup> HRP Substrate kit (170-5040, Bio-rad<sup>□</sup>, USA).

### **2.2.15 Scanning electron microscopy**

Samples were rinsed with cold distilled water and dehydrated with a ranked series of cold ethanol for dehydration, and samples were then incubated with 50% ethanol and 50% hexamethyldisilazane (HMDS) for five minutes and substituted with 100% HMDS for 10 transactions. Prior to SEM imaging, cryogels were coated with platinum for 100

seconds at 20 mA. Field emission SEM images were obtained with a JEOL 6700 (JEOL, Ltd, JAPAN) instrument.

### **2.2.16 Scaffold fabrication**

Previously described methods were applied to synthesize MeCS from chondroitin sulfate (CS; Sigma-Aldrich). The MeCS was purified by dialysis against distilled water for 48 hours and then put in deionized water for 24 hours, frozen and lyophilized. The PEGDA-MeCS was synthesized by mixing MeCS at 20% (w/v) and PEGDA oligomers at 20% (w/v) in deionized water to prepare a solution of 10% w/v) at room temperature. 0.1 grams of Whitlockite (WH) and Hydroxyapatite (HAP) were appended to the polymer solution and vortexed for particle dispersion. A thermo-initiator (ammonium persulfate; APS, Sigma-Aldrich) and accelerator (Tetramethylethylenediamine; TEMED, Sigma-Aldrich) were used as crosslinking agents for polymerization, and later at a certain point of time; cryogels were frozen by liquid nitrogen and lyophilized for later usage (Figure. 2.1).

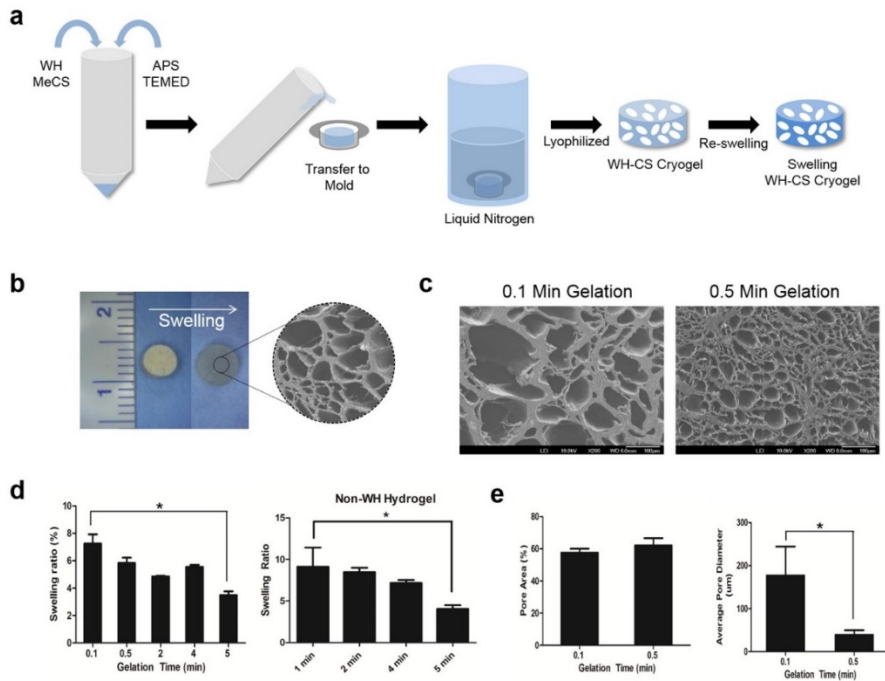


**Figure. 2.1** WH-embedded hybrid 3D cryogel characterization. **a**, Schematic illustrations of synthesis CS-based cryogel with WH. **b**, Gross images of dried and swelling cryogel. **c**, FESEM images of cryogel's pores depended on the time of gelation (0.1 min and 0.5 min). **d**, Swelling ratio vs. gelation times graph for WH-embedded or non-WH cryogels. **e**, Pore area and diameter vs. gelation times graph for WH-embedded cryogels.

### **2.2.17 Mechanical properties of scaffolds**

Cryogels were swollen and weighted in the equilibrium-swollen state. The gels were lyophilized to remove water and the dry weight was measured. The swelling ratio,  $Q$ , was calculated from the mass swelling ratio equation [216]. For mechanical characterization, hydrogels were dissolved in PBS for 24 hours and a compressive modulus was quantified from the linear region of the stress-strain curve using Instron<sup>®</sup> Model 5966 (Instron Corporation, MA, USA) with a 10 kN load cell. For the rheological assays, a strain-controlled rotational rheometer determined the elastic property of cryogels (TA, ARES). Cryogels were prepared in 25 mm diameter and 1 mm height. For frequency sweep measurement, the strain was kept at 0.1 % and the frequency was varied from  $10^{-1}$  to  $10^2$  rad/s.

### **2.2.18 Ethics statement**

All experiments were maintained and cared in accordance with the Guide for the Care and Use of Laboratory Animals by the Seoul National University. All operations were performed under Zoletil 50 (Virbac)

and Rompun<sup>®</sup>inj (Bayer) anesthesia, and all endeavors were established to minimize animal suffering.

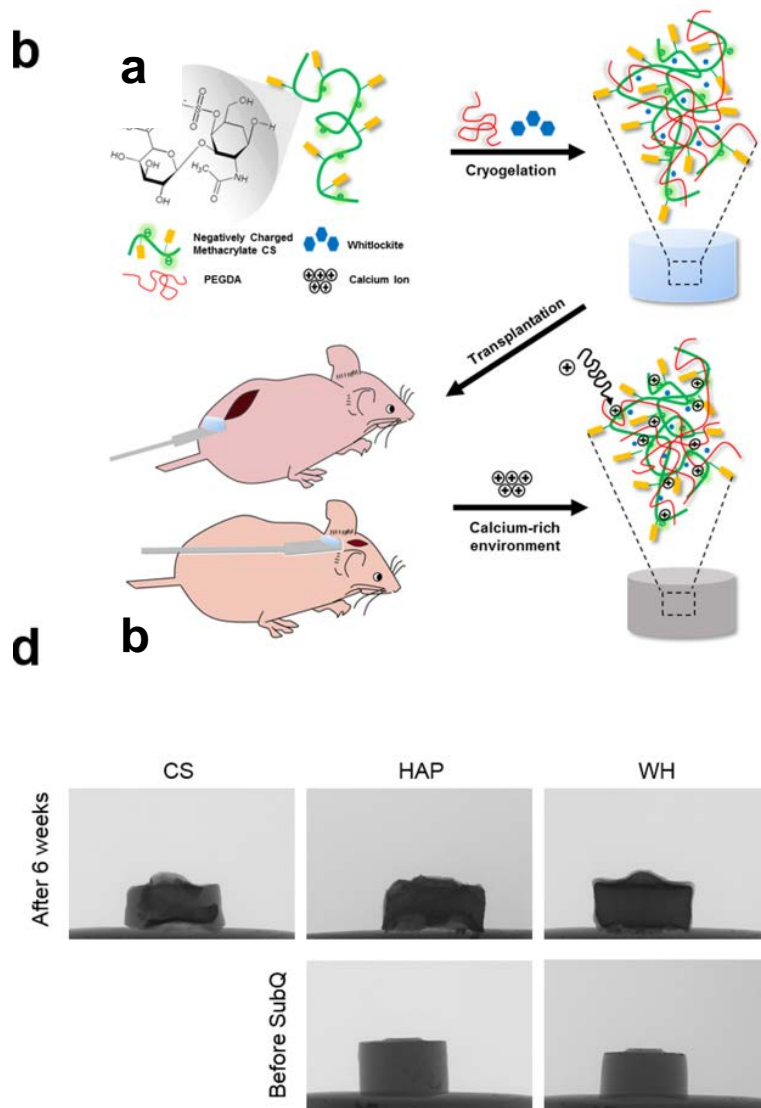


**Figure 2.2** Subcutaneous cryogel experiment. (a) Brief scheme of *in vivo* experiment. (b) 2D images of micro-CT analysis.

### **2.2.19 Surgical procedures**

Thirty female Balb-C nude mice were used for the animal experiments. All mice were handled regularly for at least one week prior to surgery and were individually housed in cages in climate-controlled rooms at 22°C with 50% humidity and 12 h light/dark cycles. Surgical procedures were performed under semi-sterile conditions with animals under anesthesia induced by the intraperitoneal injection of Zoletil 50 and Rompun<sup>®</sup>inj. For subcutaneous injection, an incision was made over the scalp between the backbone, and a disk-shaped cryogel was transplanted. Animals were ultimately sacrificed by CO<sub>2</sub> gas injection at six weeks post-operation. For the calvarial defect, a sagittal incision was created over the scalp from the nasal bone to the middle sagittal crest, and the periosteum was bluntly dissected. Using a punch, a 4 mm diameter pit defect was made with a drill, which was constantly cooled with sterile PBS. The calvarial cylindrical was then carefully removed. Animals were assigned into four groups: 1) left empty as a negative control (Sham), 2) filled with CS cryogel (CS), 3) filled with HAP embedded CS cryogel (HAP), or 4) filled with WH embedded CS cryogel (WH). The skin was sutured with 6-0 Vicryl, and the animals

were monitored following standard post-operative animal care protocols. Animals were ultimately sacrificed by CO<sub>2</sub> gas injection at two months post-surgery. For proliferation test, DNA amount of each group was quantified using Quant-iT™ Picogreen dsDNA assay Kit (Invitrogen™) according to the manufacturer's instruction. A brief scheme of animal study is presented in Figure 2.2a

### **2.2.20 Micro-computed tomography (Micro-CT)**

Micro-CT analysis was used to quantify the volume of bone formation within the cryogel and defect (Fig. 2.2.b). The tomography of fixed cryogels in the surgical sites and calvarial bone specimens were performed using SkyScan 1172 (SkyScan, Belgium) at 59 kV, 167  $\mu$ A, and an exposure time of 40 ms through a non-filter. The X-ray projections were obtained in 0.6° intervals with a scanning angular rotation of 360°. An automated threshold algorithm segmented the reconstructed dataset. The projected images were reconstructed into three-dimensional images using ReCon Micro-CT software from SkyScan.

### **2.2.21 Histological assessment and immunostaining analysis**

For histological assessment, the defect and surrounding tissues were fixed in 4% paraformaldehyde for 24 h, decalcified with 0.5 M ethylenediaminetetraacetic acid (EDTA) at pH 7.4 for 2 weeks, and embedded in paraffin. Tissues were longitudinally sectioned with a 4- $\mu$ m thickness, deparaffinated with xylene, gradually hydrated, and stained with H&E and MTC for light microscopic analysis. Images were captured in the microscope with a 4X objective lens (Olympus, Japan) and a digital camera (ProgRes C14, Jenoptik, Germany).

### **2.2.22 Nanoindentation analysis**

Nanoindentation method was used to analyze the elastic modulus and contact hardness of mouse bone tissue and implants. Mouse cranial specimens were fixed 24 hours by 4% of paraformaldehyde and embedded with acrylic resin (Ortho-Jet, Lang, Wheeling, IL). After

embedded, resin block is sectioned into 2 mm thickness with a low speed diamond saw (Isomet, Buehler Lake Bluff, IL). Each section was polished using silicon carbide abrasive paper and aluminum oxide paste and glued onto a stainless steel holder and mounted on a nanoindenter (Nano-XP, MTS, Oakridge, TN). All indentations were conducted up to 500 nm depths with loading and unloading displacement rates of 10 nm/s. The indentation force-displacement curves then were used to obtain the contact hardness by dividing the peak indentation force by the projected area at the end of loading, and the elastic modulus using the unloading slope. The distance between indent locations was at least 30  $\mu\text{m}$  to avoid any interruptions from the adjacent indents.

### **2.2.23 Fourier-Transform Infrared Spectroscopy (FTIR) analysis**

FTIR of mineralized cryogel were measured to determine the hydroxy and phosphate groups. Using an attenuated total reflection infrared spectrometer (ATR-FTIR, Bruker Tensor 27) at range of 4000 to 650  $\text{cm}^{-1}$

<sup>1</sup>, all of three groups including control, HAP and WH cryogel spectra were recorded.

#### **2.2.24 Statistical analysis**

All data are presented as the mean  $\pm$  standard deviation (SD). Statistical significance was determined by analysis of variance (ANOVA single factor) with \*  $p < 0.05$ , \*\*  $p < 0.001$ , and \*\*\*  $p < 0.0001$ .

### **2.3 Results**

To mimic the natural components of bone minerals, WH nanoparticles were synthesized by a wet precipitation method in an aqueous system. Additionally, HAP nanoparticles were prepared by a similar precipitation method for comparison. As shown in Figure 2.3a, X-ray diffraction (XRD) patterns of WH and HAP nanoparticles showed that both synthesized nanoparticles were pure without the existence of any heterogeneous phases. Their peaks matched previously known XRD patterns of WH (JCPDS 70-2064) and HAP (JCPDS 84-1998). From

field emission scanning electron microscopy (FESEM) analysis, WH nanoparticles had a rhombohedral-like shape with a homogenous size of approximately 50 nm (Fig. 2.3b). HAP nanoparticles were ellipsoidal with an average size of approximately 80 nm (Fig. 2.3c).

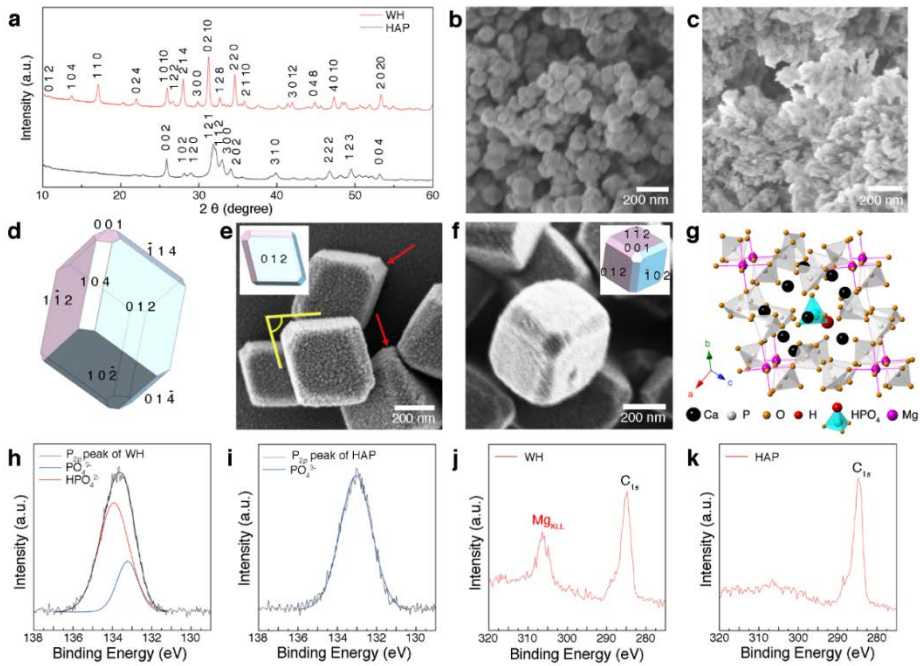


**Figure 2.3** Synthesis and material characterization of the two major biominerals, whitlockite (WH:  $\text{Ca}_{18}\text{Mg}_2(\text{HPO}_4)_2(\text{PO}_4)_{12}$ ) and hydroxyapatite (HAP:  $\text{Ca}_{10}(\text{PO}_4)_6(\text{OH})_2$ ). a, X-ray diffraction (XRD) patterns of synthesized WH (red line) and HAP (grey line) nanoparticles, confirming that both materials have homogeneous phases. b, Field emission scanning electron microscopy (FESEM) image of WH nanoparticles that were approximately 50 nm in size. c, FESEM image of HAP nanoparticles that were approximately 80 nm in length. d, General rhombohedral habit of WH crystal drawn based on  $\{012\}$ ,  $\{001\}$  and  $\{104\}$  planes. e, FESEM image of enlarged WH nanoparticles with approximately 200 nm size.  $(012)$  plane is observed in front with its edge angle  $77.5^\circ$  (angle marked with yellow), which well match with the theoretical angle between  $(\bar{1}02)$  and  $(1\bar{1}2)$ . Additionally, growth of the  $\{104\}$  planes can be observed at the side of WH nanoparticles (marked by red arrows). Crystal habit of WH drawn from the same direction as the FESEM image is presented in the inset for easier understanding. f, FESEM image of the  $(001)$  plane growth in WH nanoparticles. g, Atomic

arrangement in WH chemical structure, depicting  $(10\bar{2})$ ,  $(012)$  and  $(1\bar{1}2)$  planes at the side, front and bottom, respectively. Atomic size in the figure is exaggerated for easier understanding. h-k, X-ray photoelectron spectroscopy (XPS) analysis of WH and HAP nanoparticles.  $P_{2p}$  peaks of WH (h) and HAP (i) and Mg auger peaks of WH (j) and HAP (k) are shown. Based on the shift in the position of the  $P_{2p}$  peak of WH from HAP, the  $P_{2p}$  peak of WH is deconvoluted into  $HPO_4^{2-}$  (red line) and  $PO_4^{3-}$  (blue line) by utilizing CasaXPS software. Additionally, the Mg auger peak only existed in WH nanoparticles.

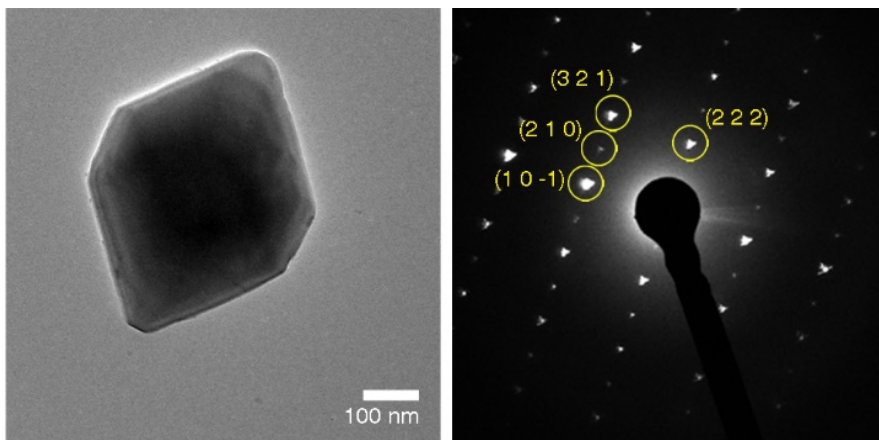


**Figure 2.4** Bright field image and diffraction pattern of a single whitlockite (WH:  $\text{Ca}_{18}\text{Mg}_2(\text{HPO}_4)_2(\text{PO}_4)_{12}$ ) nanoparticle, along the  $[-1\ 2\ -1]$  zone axis. Bright field image clearly demonstrated rhombohedral morphology of WH nanoparticle. Additionally, diffraction spots corresponded well to the previously reported data from JCPDS 70-2064. There was no trace of any secondary phase in a single WH nanoparticle.

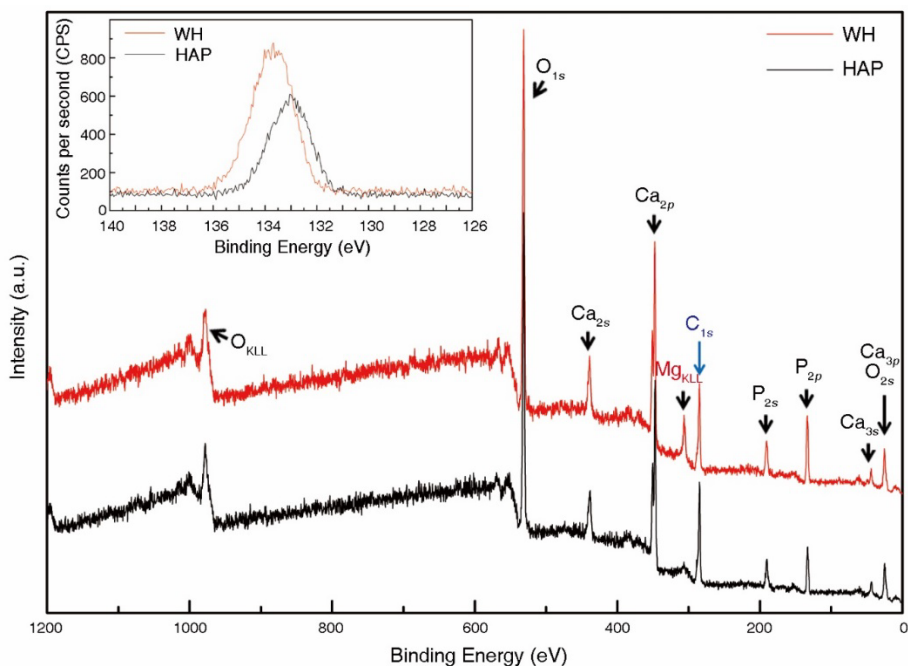


**Figure 2.5** X-ray photoelectron spectroscopy of whitlockite (WH:  $\text{Ca}_{18}\text{Mg}_2(\text{HPO}_4)_2(\text{PO}_4)_{12}$ , red line) and hydroxyapatite (HAP:  $\text{Ca}_{10}(\text{PO}_4)_6(\text{OH})_2$ , black line). Both spectra were calibrated based on the  $\text{C}_{1s}$  peak at 284.8 eV. The inset magnifies  $\text{P}_{2p}$  peaks from WH and HAP, which demonstrated the  $\text{P}_{2p}$  peak shift in WH with higher intensity than HAP.

The direct visualization of a single WH nanoparticle was also performed by high-resolution transmission electron microscopy (TEM). Diffraction pattern analysis of an enlarged single WH nanoparticle was well matched with the crystal information of naturally occurring WH crystals (Fig. 2.4). Based on morphology analysis, the exposed surface plane of the synthesized WH nanoparticle was similar to that of naturally occurring WH crystal (Fig. 2.3d) [217]. In Figure 2.3e, the {012} plane of the enlarged WH nanoparticle has its edge angle at approximately  $77.5^\circ$ , which corresponded well to the theoretical angle between  $(\bar{1}02)$  and  $(1\bar{1}2)$  in a hexagonal setting. Moreover, developments of {104} small planes were distinctly observed. In Figure 2.3f, the growth of the (001) plane among {012} planes and {104} planes was found. Figure 2.3g presents the atomic arrangement in the WH crystal structure, which depicts  $(10\bar{2})$ , (012) and  $(1\bar{1}2)$  planes at the side, front and bottom, respectively.

We further investigated the surface characteristics of WH and HAP nanoparticles by X-ray photoelectron spectroscopy (XPS). Due to the presence of  $\text{HPO}_4^{2-}$  in WH, the position of the P2p peak was shifted with

higher peak intensity compared to that of HAP (Fig. 2.3h, j, and Fig. 2.5). Additionally, while the Mg KLL auger peak was clearly shown in WH (Fig. 2.3j), there was none in HAP (Fig. 2.3k). In addition, the atomic ratios on the surfaces of WH and HAP nanoparticles were calculated from the number of detected electrons in the  $Ca_{2s}$ ,  $Mg_{2s}$  and  $P_{2s}$  peaks. From the XPS analysis results, the ratios between cat- and anions of WH ((Ca+Mg)/P) and HAP (Ca/P) were 1.44 and 1.63, respectively, while their theoretical values were 1.43 and 1.67, respectively. Therefore, for both WH and HAP nanoparticles in this research, we concluded that the surface characteristics were practically indistinguishable to the bulk.

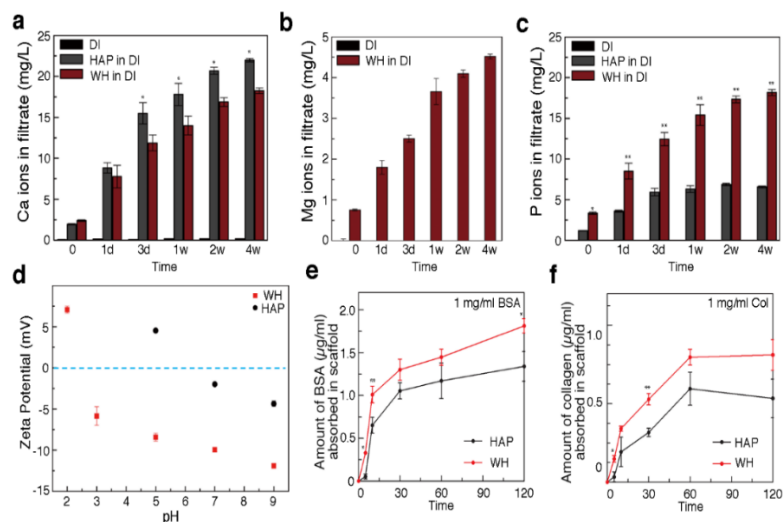


**Figure 2.6** Effect of whitlockite (WH:  $\text{Ca}_{18}\text{Mg}_2(\text{HPO}_4)_2(\text{PO}_4)_{12}$ ) and hydroxyapatite (HAP:  $\text{Ca}_{10}(\text{PO}_4)_6(\text{OH})_2$ ) nanoparticles on the surrounding system, particularly at their near surface. a-c, Ion release amounts of WH and HAP nanoparticles in the aqueous system, depending on different aging time. Released levels of (a) Ca ions, (b) Mg ions, and (c) P ions from the WH-aged and HAP-aged filtrates ( $n=4$ ) after aging for day 0 to four weeks are shown. d, Zeta potential analysis of WH (red square,  $n=3$ ) and HAP (black circle,  $n=3$ ) nanoparticles, dispersed in the distilled water. Isoelectric point (IEP) of WH was located between pH 2 and pH 3, while the IEP of HAP was located at pH 7, demonstrating that WH has a negative surface charge in the neutral condition. e-f, Absorbed protein amounts on the WH and HAP scaffold, depending on different aging time for (e) 1 mg/ml bovine serum albumin (BSA,  $n=5$ ) and (f) 1 mg/ml of type 1 collagen ( $n=5$ ). \*  $p < 0.05$ , \*\*  $p < 0.001$ . \*\*\*  $p < 0.0001$ .

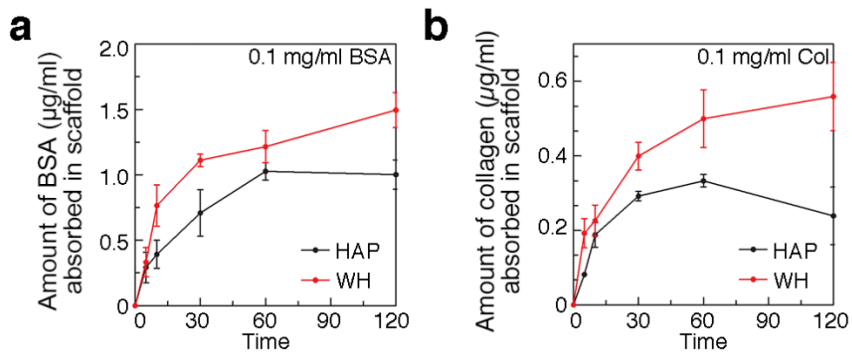


**Figure 2.7** Amount of absorbed protein in the whitlockite and hydroxyapatite scaffold for (a) 0.1 mg/ml bovine serum albumin (BSA, n=5) and (b) 0.1 mg/ml of type 1 collagen (n=5).

For the resorption stability and ion release kinetics, WH and HAP nanoparticles were dispersed in distilled water, filtrates were collected through a membrane with 200 nm-sized pores, and an inductively coupled plasma atomic emission spectrometer (ICP-AES) was used to analyze the amounts of Ca, Mg and P ions. Ions release kinetic from both WH and HAP nanoparticles were evaluated up to 4 weeks in neutral pH condition (Fig. 2.6a-c). WH displayed faster P and Mg ions release kinetics compared to the HAP. However, elevated Ca ions were detected with HAP nanoparticles.

Next, we examined the interaction between the WH and bone-related extracellular matrix (ECM) proteins. Bone ECM proteins play a vital role in facilitating the bone formation by assembling with inorganic subunits [218, 219]. Since the charged surface can strengthen the electrostatic interactions with proteins by changing the protonation state through a charge regulation mechanism [220, 221], we evaluated the surface charge of WH and compared it with HAP in various pH conditions (from pH 2 to 9) by addition of HCl and NaOH. As shown in Figure 2.6d, HAP reached its isoelectric point (IEP) at around pH 7, which corresponded well with the previously reported [222, 223].

Notably, the IEP of WH was located between pH 2 and 3 and thus, the surface charge of WH was highly negative compared to HAP at a neutral pH. To examine whether the WH surface provides a favorable environment for protein binding, we measured the absorbed amount of bovine serum albumin (BSA) and type I collagen on WH nanoparticles (Fig. 2.6e, f and Fig. 2.7). Serum albumin was selected as a general protein because it does not include complex tryptophan, carbohydrates, and prosthetic groups in its structure and thus is involved less in specific biochemical reactions [224, 225]. In addition, type I collagen was chosen, as it is one of the major bone ECM components. The results showed that the adsorbed amount of BSA was higher on WH cylindrical scaffold than HAP throughout the period of 120 minutes. Furthermore, the absorbed amount of type I collagen was also higher in the WH than the HAP cylindrical scaffolds, which were fabricated by pressing in a mold and sintering at 700 °C.

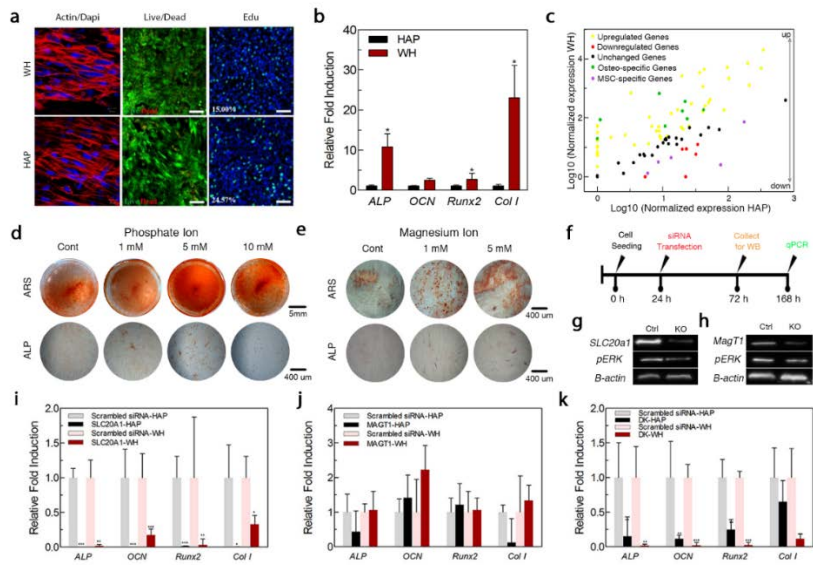


**Figure 2.8** Differentiation of human tonsil-derived mesenchymal stem cells (hTMSCs) on WH and HAP discs by the phosphate and magnesium ion effect. a, hTMSCs morphology, cytotoxicity, and proliferation. b, Osteogenic gene expression markers (*ALP*, *OCN*, *Col I*, and *RunX2*) were tested after two weeks of hTMSCs culture in HAP (n=3) and WH (n=3) 2D cylindrical scaffolds. c, Three days of hTMSC culture on WH 2d scaffolds increased the mRNA expression profile over HAP, as assessed by quantitative RT-PCR using the SA Biosciences Human Mesenchymal Stem Cell PCR Array. The scatter plot shows the number of genes with similar expression levels (within black lines), upregulated (yellow), downregulated (blue), or osteogenic (red) genes. d-e, Alizarin Red S (ARS) and alkaline phosphatase (ALP) staining after seven days osteogenic differentiation in the presence of the indicated concentrations of (d) phosphate ions and (e) magnesium ions. f, Time schedule for siRNA transfection of hTMSCs. 24 hours after seeding (0 h), cells were transfected with siRNA with lipofectamine. Seventy-two hours later, after confirmation by western blot assay, the medium was replaced with differentiation medium (OM) to promote the osteogenic differentiation. qPCR was performed after 168 hours. g-h, Western blot analysis of knocking out the protein channels (g) *SLC20a1*, (h) *MagT1*, and

cytoplasmic (g, h) *pERK* expression in cells.  $\beta$ -actin was used as a loading control. i-k, A quantitative analysis (real time PCR) of the expression of the *ALP*, *OCN*, *RunX2*, and *Col I* of knocking out (i) *SLC20a1*, (j) *MagT1*, and (k) double knockout channel protein conditions. \*  $p < 0.05$ , \*\*  $p < 0.001$ . \*\*\*  $p < 0.0001$ .

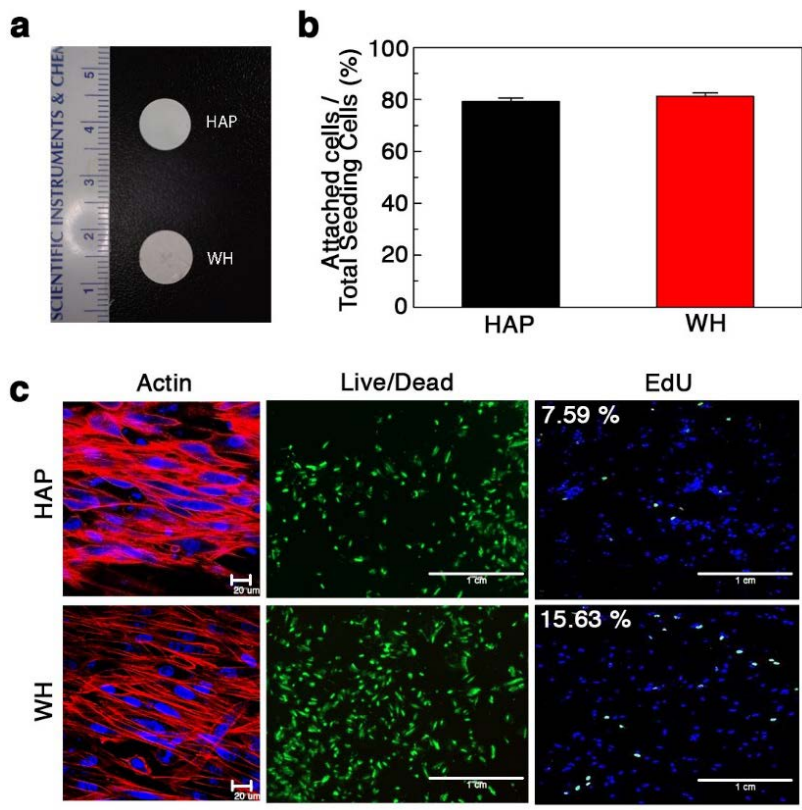


**Figure 2.9** Additional 2D cylindrical scaffolds analysis. **a**, Gross image of synthesized hydroxyapatite (HAP:  $\text{Ca}_{10}(\text{PO}_4)_6(\text{OH})_2$ ) and whitlockite (WH:  $\text{Ca}_{18}\text{Mg}_2(\text{HPO}_4)_2(\text{PO}_4)_{12}$ ) 2D cylindrical scaffolds. **b**, Cellular adhesion on scaffolds was measured by attached hTMSCs over total seeding cells (%). **c**, cellular morphology, cytotoxicity, and EdU staining of hTMSCs on HAP and WH 2D scaffolds. (Scale bars: 20  $\mu\text{m}$  for actin, 1 cm for Live/Dead and EdU staining)

For the *in vitro* cellular response comparisons of WH and HAP, we fabricated cylindrically shaped discs with same roughness by high-temperature press and cellular morphology, cytotoxicity, and proliferation were performed (Fig. 2.8a and 2.9). In addition, we compared the mineral microenvironment-dependent osteogenic differentiation of human tonsil-derived mesenchymal stem cells (hTMSCs). hTMSCs (passage 6) cultured with osteogenic medium (OM) on the surface of WH and HAP subsequently showed osteogenic differentiation behavior. Gene expression analysis of bone-related markers showed that the WH microenvironment particularly activated genes involved in early bone formation. On day 14 of hTMSCs differentiation, quantitative real time-PCR analysis of bone-related genes, such as Alkaline phosphatase (*ALP*), osteocalcin (*OCN*), runt-related transcription factor 2 (*RunX2*), and type I collagen (*Col 1*) demonstrated that cells cultured on WH exhibited significantly increased gene expression compared to HAP cylindrical scaffolds (Fig. 2.8b). The qPCR with protein adsorption test results together clearly indicated that the WH is a material that has a high potential of osteogenicity. Moreover, more pronounced differences in the gene expression of *ALP*,

which participates particularly in the early stage of osteogenic differentiation, in WH was effective in the early stage of the bone formation mechanism.

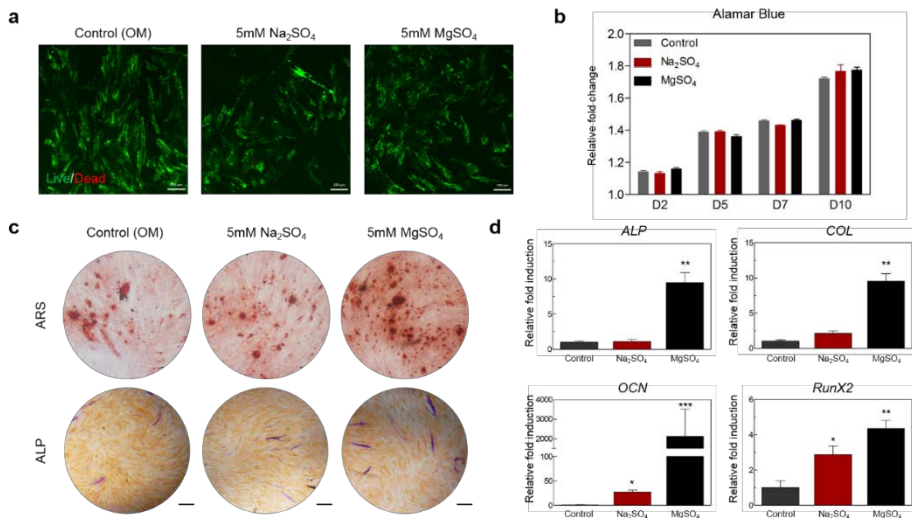


**Figure 2.10** Magnesium influence in osteogenic differentiation. a, Cellular viability of control (OM), 5mM Na<sub>2</sub>SO<sub>4</sub> and 5mM MgSO<sub>4</sub> group by Live/dead<sup>®</sup> assay. b, Proliferation profile of each conditions upto 10 days by Alamar blue assay. c, Alizarin Red S (ARS) and alkaline phosphatase (ALP) staining after fourteen days osteogenic differentiation in the presence of indicated groups. d, A quantitative analysis (real time PCR) of the expression of the *ALP*, *Col I*, *OCN*, and *RunX2*.

To compare the role of WH nanoparticles from HAP in the early mineralization process, the expression levels of 84 specific genes (excluding housekeeping and control genes) related to MSCs were measured (Fig. 2.8c). Many of the osteogenic specific genes, including *BMP2* and *RunX2* (also *SMURF1*, *SMURF2*, *HDAC1*, *PTK2A*, *FGF10*, and *HNF1A*) were upregulated on hTMSCs cultured on WH compared to hTMSCs on HAP cylindrical scaffolds. Moreover, downregulation of a critical number of MSC-specific (*PROM1*, *THY1*) and stemness (*INS*, *POU5F1*, and *TERT*) genes can be interpreted as losing their pluripotency and inducing rapid osteogenic differentiation of hTMSCs on WH scaffolds compared to on HAP scaffolds (Table 2.1). In terms of the osteogenic cascade, WH nanoparticles induced the gene expression levels of *PDGFRB*. *PDGFRB*, which is a receptor of *PDGF*, directly promotes MSC proliferation and osteogenic differentiation via ERK pathway [226]. The duration and magnitude of *ERK* activation is highly critical factors in the determination of osteogenesis of MSCs at the beginning of bone formation.

From observation of the existence of Mg and abundant release of P ions in WH, we further investigated the role of ions in osteogenic

differentiation of hTMSCs. After 14 days of hTMSCs culture in OM with an incremental concentration of phosphorus (0 mM, 1 mM, 5 mM and 10 mM of  $\text{Na}_2\text{HPO}_4$  and  $\text{NaH}_2\text{PO}_4$  mixture), osteogenic differentiation [as indicated by positive Alizarin Red S (ARS) and Alkaline Phosphatase (ALP) staining] was induced in the presence of phosphorus. Both staining results showed that osteogenic differentiation is concentration dependent: higher expression levels of ARS and ALP were observed in 5 mM of  $\text{Na}_2\text{HPO}_4$  and  $\text{NaH}_2\text{PO}_4$ , compared to lower concentrations (Fig. 2.8d). For Mg, the group receiving 5 mM of  $\text{MgSO}_4$  showed the highest ARS and ALP expression levels (Fig. 2.8e) and Mg also induced osteogenic differentiation in a concentration-dependent manner as well as P ions (Fig. 2.9). Similarly, Yosizawa *et al.* suggested that an adequate amount of Mg could enhance *Col X* and *VEGF* expression via *HIF-2 $\alpha$*  production [227]. When an excessive amount of P or Mg ions were applied (sodium phosphates and  $\text{MgSO}_4$ ), cellular viability and differentiation were significantly reduced (Fig. 2.10a, b). These results indicated that biominerals with optimum solubility could continuously provide a proper amount of effective ions to stimulate bone generation.

To elucidate the roles of ions released from WH on the osteogenic commitment, we knocked out two ion-specific protein transporter [ $\text{PO}_4^{3-}$  (*SLC20a1*) and  $\text{Mg}^{2+}$  channels (*MagT1*)] on the cell membrane via siRNA (Fig. 2.8f). When P ions enter cells, they are transported through sodium-dependent phosphate transporter 1, encoded by *SLC20a1* gene, mostly in the form of  $\text{PO}_4^{3-}$  [228]. Silencing of both channels was confirmed by Western blot analysis (Fig. 2.8g, h). Consequently, silencing led to a reduction in the phosphorylation of ERK proteins. Since phosphorylation is directly related to the cellular phosphate level, knocking out the phosphate transporter resulted in a reduced pERK gene level in the cell.[228] Likewise, intracellular  $\text{Mg}^{2+}$  deprivation via knocking out magnesium transporter, encoded by *MagT1* gene, inhibited the pERK cascade [229].

Calcium phosphates have been shown to regulate the osteogenic differentiation pathway of stem cells through the phosphate transporter [228, 230]. Our results also indicated that  $\text{PO}_4^{3-}$  ions released from both WH and HAP were effective in osteogenic differentiation. Interestingly, *SLC20a1* gene knocked out cells cultured on WH cylindrical scaffolds showed higher bone-related gene expressions

compared to *SLC20a1* gene knocked out cells cultured on HAP cylindrical scaffolds (Fig. 2.8i). These results also confirmed that most osteogenic genes were downregulated after knocking out the magnesium transporter (Fig. 2.8j). From the gene expression profile result, disabling the *SLC20a1* gene implicates more favorable changes of osteogenic gene silencing than knocking out the *MagT1* channel. Since both channels participate the osteogenic differentiation, gene expression was dramatically downregulated when the both genes are knocked out simultaneously (Fig. 2.8k). Taken together, a possible explanation for the enhanced osteogenesis of WH nanoparticles is  $\text{PO}_4^{3-}$  and  $\text{Mg}^{2+}$  release, which concurrently stimulate via the *ERK* pathway of the hTMSCs.

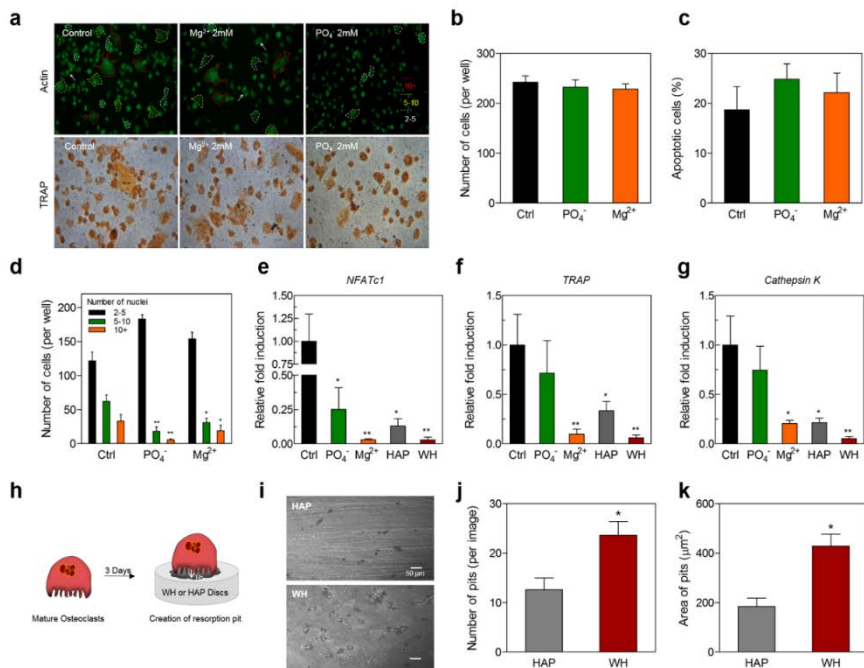


**Figure 2.11** Inhibitory effect of WH on osteoclastic differentiation by phosphate and magnesium ions a-c, The effect of 2mM of Mg<sup>2+</sup> and PO<sub>4</sub><sup>3-</sup> on osteoclast differentiation, proliferation and apoptosis. (a) Raw 264.7 cells were culture with *RANKL* and 10% FBS. Actin-stained cells (top) and *TRAP*-stained cells (bottom) and the number of cells with more than two nuclei are shown. b-c, Live/dead assay. (d) The effect of Mg<sup>2+</sup>, PO<sub>4</sub><sup>3-</sup>, HAP, and WH on osteoclast fusion. An increase in the proportion of multinucleated osteoclasts can be seen. e-f, Quantitative Real-Time PCR analysis. The expression of osteoclast-specific genes (e) *NFATc1*, (f) *TRAP*, and (g) *Cathepsin K*. h, Mature osteoclasts were cultivated on top of HAP and WH discs. i-k, The effect of HAP and WH on bone resorption. (i) A pit formation assays is shown (Top: HAP, Bottom: WH). Total number (j) and surface area of resorption pits were measured (k). \*  $p < 0.05$ , \*\*  $p < 0.001$ . \*\*\*  $p < 0.0001$ .

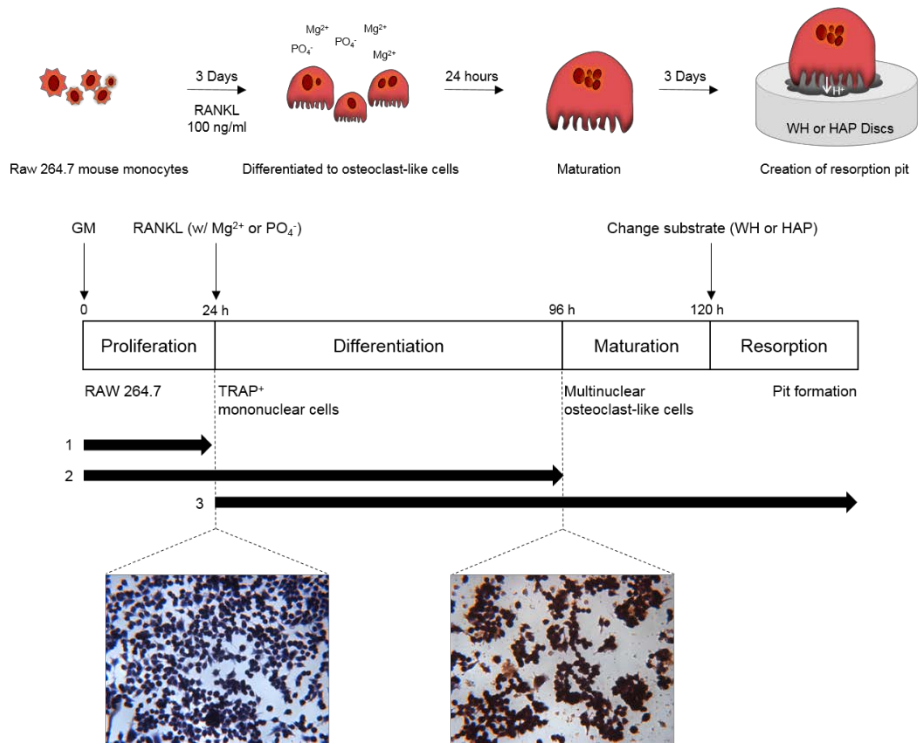


**Figure 2.12** Experimental scheme of the effect of  $Mg^{2+}$ ,  $PO_4^-$ , WH and HAP on osteoclast differentiation. Raw 264.7 cells were cultured with RANKL, and  $Mg^{2+}$  or  $PO_4^-$  was added in the proliferation (1), differentiation (2), maturation and resorption of HAP and WH discs (3 and 4) phase.

Previous studies have demonstrated that the local ionic concentration may influence the osteoclast differentiation [231]. In order to demonstrate WH's inhibitory effect on osteoclast differentiation via local  $\text{PO}_4^{3-}$  and  $\text{Mg}^{2+}$  ions, we have differentiated RAW 264.7 cells to osteoclast under the condition of 2mM of  $\text{PO}_4^{3-}$  and  $\text{Mg}^{2+}$ , each (Fig. 2.11a and Fig. 2.12). There was no notable change or difference between the total number of cells and apoptotic cells (Fig. 2.11b, c), the control group generated a large number of multi-nucleated osteoclasts and a high level of tartrate-resistant acid phosphatase (TRAP) expression. In contrast, we found that treatment of the cells with 2mM of  $\text{PO}_4^{3-}$  and  $\text{Mg}^{2+}$  plus *RANKL* resulted in only a few small osteoclasts with a low number of multi-nuclei (Fig. 2.11a, d). We have confirmed that osteoclast-specific genes such as *NFATc1* (nuclear factor of activated T cells, cytoplasmic, calcineurin-dependent 1), *TRAP*, and *Cathepsin K* gene expression were significantly downregulated in  $\text{PO}_4^{3-}$  and  $\text{Mg}^{2+}$  group (Fig. 2.11e-g). We also have cultured the RAW 264.7 cells on top of cylindrically shaped discs of WH and HAP to see their inhibition of osteoclastic differentiation. Since WH can continuously provide

$\text{PO}_4^{3-}$  and  $\text{Mg}^{2+}$  ions, all of osteoclastic specific-genes were highly repressed by WH.

Since resorption of materials is required prior to the complete osseointegration into the native bone, the resorption pit assay was performed with mature osteoclasts in order to observe the resorption of WH and compared to that with HAP. Mature osteoclasts were cultivated for 3 days, and subsequently removed from the WH and HAP discs by trypsinization (Fig. 2.11h). To verify resorption activity, resorption pits were detected through SEM image analysis (Fig. 2.11i). Numerous pits were formed on the WH discs with an average number of around 20 and surface area of  $400 \mu\text{m}^2$ , twice higher than HAP discs (Fig. 2.11j-k). Active osteoclastic resorption pits confirmed that greater number may be due to increased solubility of WH compared to HAP under certain circumstances [232].

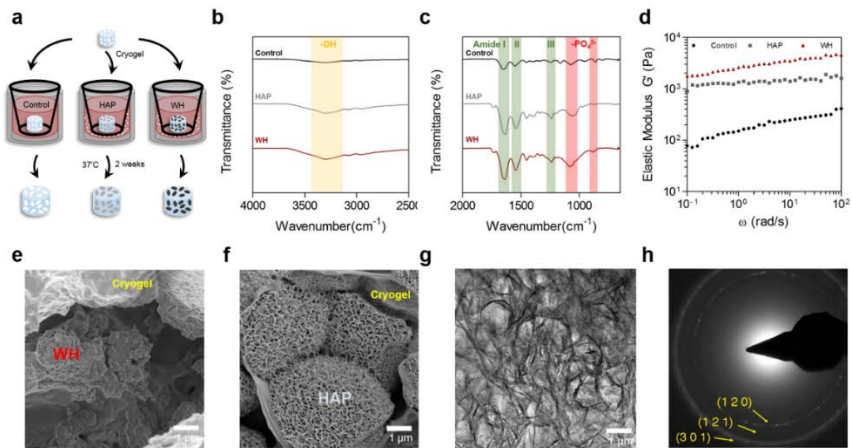


**Figure 2.13** Phase transformation of whitlockite to hydroxyapatite, Simplified scheme of 2 weeks of HAP and WH nanoparticle-mediated cryogel mineralization. b-c, Fourier Transform Infrared Spectroscopy analysis of (b) wave number between 2500-4000  $\text{cm}^{-1}$  and (c) 800-2000  $\text{cm}^{-1}$ . d, Elastic modulus of mineralized cryogel with different range of phase angles. e-h, (e) *In vivo* formation of bone mineral in the whitlockite-incorporated chondroitin sulfate (CS) gel implant, eight weeks after insertion in the *in vivo* mouse system. (f) Phase confirmation of newly precipitated bone mineral as hydroxyapatite. (g) By utilizing a Focused Ion Beam, flower-shaped bone minerals were separated and placed on a TEM grid for TEM observation. (h) The bright field image clearly reflecting ruffle-like morphology of bone mineral. The diffraction pattern of the bone mineral, which matched well with the crystal structure data of hydroxyapatite (JCPDS 84-1998). There was no trace of WH.

To examine the fate of resorbed ions from the mineral matrices, we fabricated a 3-dimensional (3D) cryogel scaffolds based on methacrylated chondroitin sulfate (MeCS) and incubated them in ionic environment created by WH or HAPs. Cryogel scaffolds were incubated with WH and HAP nanoparticles for 2 weeks at 37°C (Fig. 2.13a). Absorption peaks at 3400 and 1300  $\text{cm}^{-1}$  attributable to the stretching of the hydroxy group and  $\text{PO}_4^{3-}$  confirmed the amount of hydroxy and phosphate group were increased in WH nanoparticle incubated group (Fig. 2.13b, c). Furthermore, the elastic component of the cryogel scaffolds by mineralization were determined by rheological studies. WH nanoparticles-incubated cryogels showed greater storage ( $G'$ ) moduli compared to HAP nanoparticle-incubated group (Fig. 2.13d). Control scaffold displayed the least storage modulus.

Since the WH nanoparticles displayed faster resorption followed by the reprecipitation in to mineral crystals, we traced the *in vivo* fate of the WH nanoparticles by electron microscopic analysis. Initially, WH nanoparticles inside the cryogel implant were distinguishable from the surrounding CS gel based on the rhombohedral morphology (Fig. 2.13e). However, after six weeks from the implant insertion, flower-like new

bone minerals were precipitated on the entire surface of the WH-embedded CS gel (Fig. 2.13f). By utilizing a focused ion beam technique, we separated newly precipitated bone and placed in on a TEM copper grid. From the HRTEM diffraction analyses, newly precipitated bone mineral had a HAP crystal structure, indicating that the WH mineral can stimulate HAP deposition (Fig. 2.13g, h).

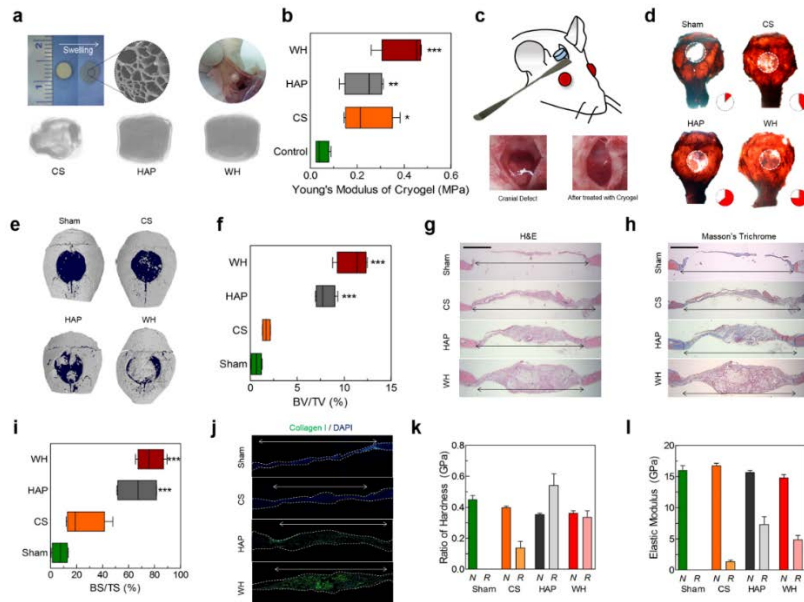


**Figure 2.14** *In vivo* bone regeneration efficacy of whitlockite (WH:  $\text{Ca}_{18}\text{Mg}_2(\text{HPO}_4)_2(\text{PO}_4)_{12}$ ) embedded 3D cryogel implants. a, After 6 weeks of subcutaneous injection, each group of cryogels rendered by the micro-CT program as grey areas indicated the amount of mineralization. b, Young's modulus of subcutaneously injected cryogels for each groups. c, bone formations were examined via subcutaneous implantation and critical sized calvarial defect models. d-h, *In vivo* bone regeneration of the calvarial defects by ARS staining (d) and microCT (e), volume are presented as a percentage calculated from the ratio of newly formed mineralized bone volume over the initial defect volume (BV – Bone Volume, TV – Total Volume), (f) and histomorphometric analysis with H&E (4 and 40X) (g), MTC (4 and 40X) (h). i, Surface area of bone formation (BS – Bone Surface, TV – Total Surface). j, Collagen and DAPI staining of implants and tissue specimens. k-l, Comparing old bone and new generated bone's ratio of hardness (k) and elastic modulus (l) measuring by nanoindentation. In a-d, n=4. In e-f, n=4 and n=5. \*  $p < 0.05$ , \*\*  $p < 0.001$ . \*\*\*  $p < 0.0001$ .

We further evaluated whether WH nanocrystals can stimulate *in situ* bone regeneration. Initially, WH-embedded cryogels were implanted for six weeks in a subcutaneous model, and post-mathematical pixel reconstruction by micro-CT showed that the WH-embedded cryogel had the highest mineral deposition compared to the HAP-embedded cryogel or negative CS control (Fig. 2.14a). The comparative mechanical strength of implants showed that Young's modulus was increased throughout the group. In particular, WH-embedded cryogel's modulus was seven times higher than the sham control and twice higher than control cryogel and HAP-embedded cryogel group (Fig. 2.14b).

We further applied WH-embedded cryogels in a critical sized calvarial defect model (Fig. 2.14c). Enhanced bone regeneration was evident after eight weeks in WH-embedded cryogel group (Fig. 2.14d), as visualized by a full range of ARS on the entire cranium. Furthermore, the WH-embedded cryogel group showed the highest degree of cell recruitment, which further supported our *in vitro* assertion that the negatively charged surface preferentially adsorbs more proteins for enhanced cell attachment [233]. For quantitative analysis, each defect area and implants were analyzed by micro-CT. Among the groups, the

largest volume of the newly generated bone was observed with WH-embedded cryogel (Fig. 2.14e, f).

In addition, histological and immunostaining observation showed that there is increased cellular infiltration (i.e., increased cellularity), protein matrix (i.e., collagen) deposition, and largest regenerated surface in the WH-embedded cryogel group (Fig.2.14g-j). Histological analysis with staining confirmed the micro-CT results and revealed more extensive bone formation in the WH-embedded cryogel group compared to the other conditions. For assessment of regenerated bone quality, each defect area and implants were analyzed by nanoindentation techniques. Native parietal bone displayed elastic modulus of 14.8 GPa with contact ratio hardness of 0.360 GPa. The newly regenerated portion of the cranial with WH-embedded cryogels resulted in elastic modulus of 6.43 GPa with contact ratio hardness of 0.335 GPa (Fig. 2.14k, l). Our *in vitro* and *in vivo* assessment of WH nanoparticles demonstrated that the enhanced bone formation by WH could be modulated by ionic microenvironment which many have attributed to the higher level of inorganic precipitation combined with increased protein adsorption (Figure 2.15).

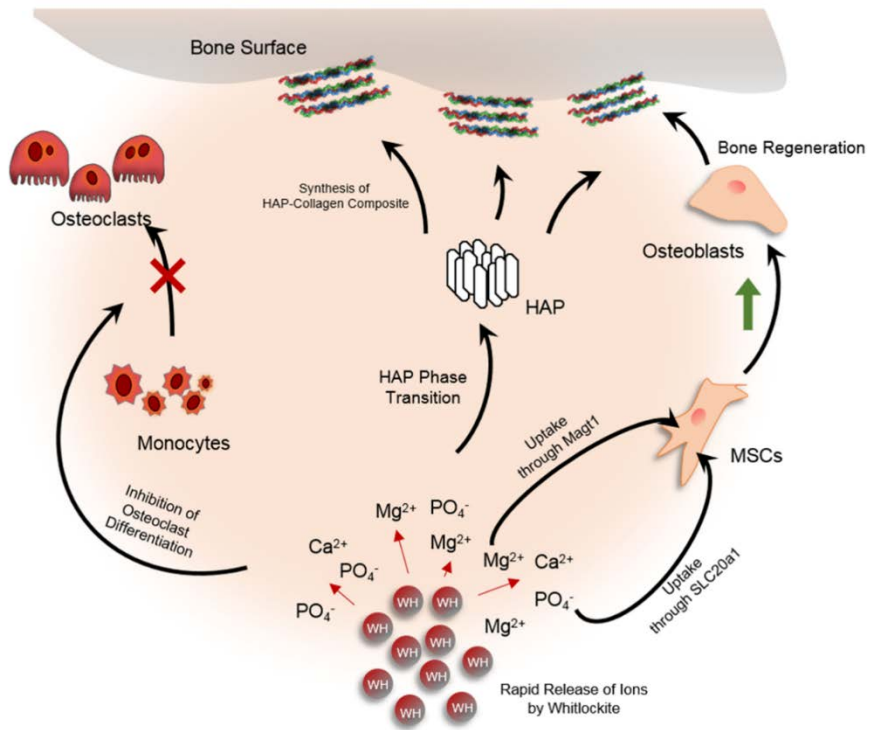


**Figure 2.15** Simplified schematic *in vitro* model of effect of whitlockite nanoparticles on MSCs, osteoclast activity, and HAP phase transformation.

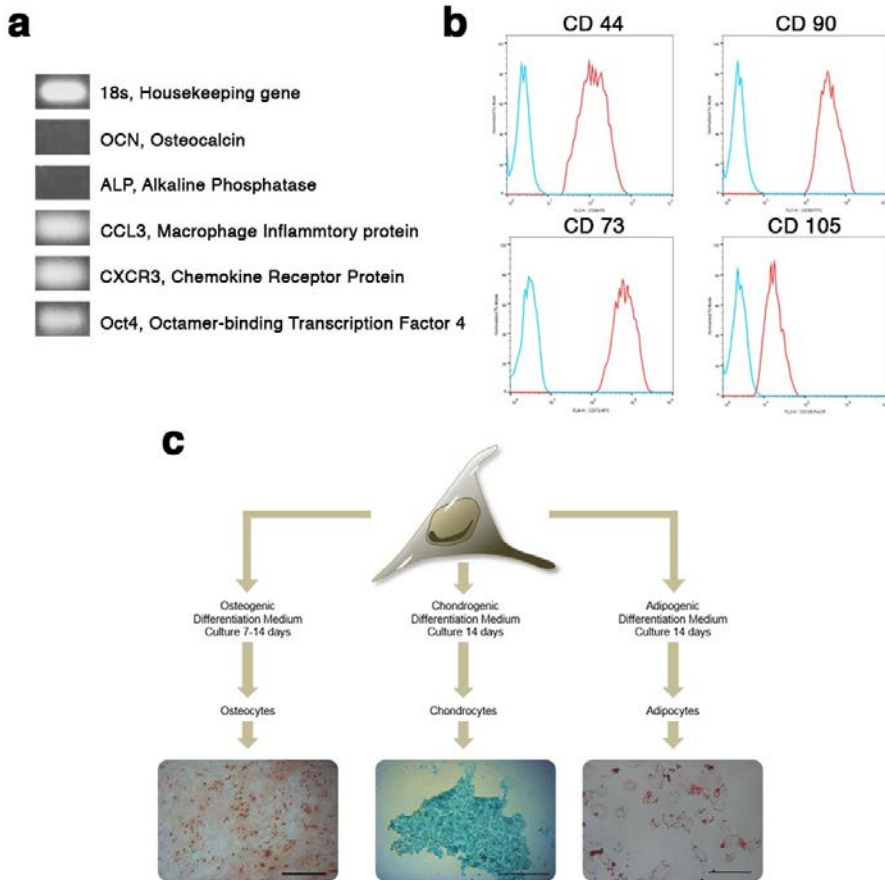


**Figure 2.16** Characterization of human tonsil derived mesenchymal stem cells (hTMSCs). a, Gene expression of hTMSCs on passage 5. As originally belonging to the immune system, hTMSCs expressed two immune-related genes; i.e., *CCL3* and *CXCR3*. Expression of *Oct4* confirmed the potency to differentiate to a certain lineage, while the absence of ALP and OCN showed that hTMSCs did not possess any osteogenic characteristics. b, Flow cytometry analysis of cell surface markers of hTMSCs on passage 5. hTMSCs were further evaluated for their MSC-like characteristics by expressing MSC surface markers: CD44, CD73, CD90 and CD 105. c, *In vitro* human tonsil-derived mesenchymal stem cells (hTMSCs) differentiation to osteogenic, chondrogenic, and adipogenic lineages.

## 2.4 Discussion

In this study, we revealed that the WH-induced bone regeneration was initiated by increased local ion concentration along with increased protein adsorption to its surface. Furthermore, WH is known to have higher stability than HAP in acidic bone remodeling condition, and it is distributed as molecular clusters in short micro-ranged distances [204, 205, 234]. Previously, local ion concentration and protein-inorganic assembly have been shown to play a critical role in bone mineralization [235-241]. In our study, our results demonstrate a potential molecular mechanisms created by resorbed ions from WH, as depicted in Figure 2.15.  $Mg^{2+}$  and  $PO_4^-$  released from WH may enters the hTMSCs respectively through *Magt1* and *SLC20a1* channel proteins to induce osteogenic differentiation. In addition, higher levels of  $Mg^{2+}$  and  $PO_4^-$  ions concentration created by WH may prevent the osteoclast differentiation from monocyte, therefore preventing the number of active osteoclasts.

When the micro-damaged area of bone is being repaired, MSCs are recruited and differentiate as osteoblasts. Since hTMSCs, which were

isolated from tonsil tissues of young toddlers, share many characteristics with bone marrow-derived mesenchymal cells, they have extensive proliferative potential and the mesenchymal ability to differentiate toward adipogenic, osteogenic, and chondrogenic lineages [242, 243], and also they were utilized to mimic early-stage of stem cells (Fig. 2.16). The WH microenvironment resulted in increased cellular proliferation compared to the HAP microenvironment. Our data showed that WH nanoparticles could continuously supply Ca, Mg and P ions in physiological conditions. As Mg ions do not participate in HAP crystals structure due to its small ionic size [204, 244], a small amount of magnesium phosphate compound that is stable in a neutral pH condition, such as newberyite ( $\text{MgHPO}_4 \cdot 3\text{H}_2\text{O}$ ), may have precipitated from excess Mg ions [245, 246]. As a result, elevated residual P ions were detected as free ion in the solution based on the composition ratios of WH, HAP, and newberyite (Ratio of Ca:Mg:P in WH=18:2:14, Ca:P in HAP=10:6, and Mg:P in newberyite=1:1). Our results indicated that WH minerals have the capacity to continuously release elevated level of Mg and P ions compare to HAP in physiologically relevant conditions. Despite the fact that Mg ions compose only small fraction of WH, released amounts

of both Ca ions and P ions were less than their expected amounts based on the released amount of Mg ions, which indicated high possibility of HAP precipitation after dissolution of WH in neutral condition. The excess amount of P in filtrates collected from WH nanoparticles in aqueous solution could be also explained based on the different solubility and different Ca/P composition of WH and HAP nanoparticles at the given pH. It is known that above pH 4.2, HAP is more stable than WH, showing that the solubility of WH gradually increased with an increase in pH [205, 234]. Accordingly, releasing magnesium ions from WH is a great advantage over HAP in terms of efficient osteogenic differentiation. Although knocking out the phosphate channel (*SLC20a1*) mostly disabled the osteogenic cascade, the magnesium channel (*MagT1*) generated an interchangeable route to the differentiation. Hence, high solubility calcium orthophosphate and magnesium alloys have been used for faster bone healing as they induce elevated local ion concentrations [235-237]. As the result of faster and Mg ion release from WH compared to HAP, we confirmed that hTMSC on WH showed enhanced osteogenic differentiation.

Additionally, inorganic biomaterials have been electrically polarized to induce a charged surface for improved protein adsorption [238-241]. When the surface is negatively charged, the pH near the surface is known to decrease and thus the protonation of ionizable functional groups in proteins can be induced, leading to an increase in the electrostatic attraction between proteins and the charged surface [247, 248]. Furthermore, immunostaining for collagen, a protein abundant in bone ECM was also showed significantly higher intensity at the WH group compared to the sham or HAP group (Fig. 2.14j). Since the WH-embedded cryogels are inherently osteoinductive, the accumulated calcification could have resulted from the differentiation of MSCs and build-up of osteoblast-secreted ECM.

## **2.5 Summary**

Based on these findings, we designed a WH-embedded 3D cryogel implant and presented enhanced healing in a critical sized calvarial defect model by mimicking the regeneration mechanism of natural bone tissue. Enhanced protein adsorption on WH minerals was also

corroborated by the *in vivo* test results, which showed higher amounts of organic bone matrix formation in WH-embedded CS gel implants than HAP-embedded CS gel implants. The success of synthetic matrices for bone repair is evaluated based on their ability to support restoration of the bone-related ECM with cellular and mechanical function [249]. From our observation on mechanical aspects, both elastic modulus and hardness of newly generated cranial had comparable value to the previously reported wild type mouse parietal bone [250]. Hence, not only quantitatively, but also qualitatively WH can induce the bone regeneration and all in its original condition through phase transformation. Taken together, these findings suggest that WH minerals have a stimulation effect in bone regeneration and thus can be applied for bone healing.

Our findings suggest that the interaction of inorganic mineral contribution during the bone remodeling process should be considered in addition to proteins, cells and hormones. In particular, inorganic minerals contribution during bone remodeling process is pronounced under acidic pH conditions. Interestingly, increased amounts of WH have been found in the pathological calcification of soft tissues such as

articular cartilage, heart valve, lung, urinary organ, and salivary glands [251]. These insights suggest that the stimulating effect of WH on mineralization should be well controlled, as it may lead to uncontrolled ectopic mineralization. In this regard, revealing the optimum amount, range and proper distribution behavior of WH in hard tissue will lead to better understanding of bone health.

# **3 CHAPTER THREE: CHONDROITIN**

## **SULFATE-BASED BIOMINERALIZING**

### **HYDROGELS FOR BONE TISSUE**

#### **ENGINEERING**

### **3.1 Introduction**

Bone grafts are utilized in a wide array of clinical settings to augment bone regeneration. Bone defect repair utilizing tissue engineering strategies often utilize biodegradable scaffolds that are intended to be gradually replaced by neo bone tissues. Currently, synthetic calcium phosphate (CaP) derivatives, such as hydroxyapatite, whitlockite, and  $\beta$ -TCP, are often incorporated into biodegradable scaffolds in order to provide bioactivity, enhance osseointegration and improve mechanical properties. As calcium and phosphate are critical components for bone inorganic structure [252-254], multiple methods of incorporating both ions in to biodegradable scaffolds have been developed for bone tissue engineering [255-257]. In addition, biomaterials that actively recruit inorganics components and enhance osteogenic differentiation *in vivo*

are utilized as bone scaffolds. Indeed, the strategies to enhance the bioactivity of scaffolds would further improve the integration of bone scaffolds with surrounding bone tissue.

Various approaches have been used to prepare hydrogels for mimicking the bone environment. In addition, recent efforts have begun to explore biomineralization of bone stimulating inorganic apatite through naturally binding ions. Hydrogels with apatite-nucleating monomers, such as ethylene glycol methacrylate phosphate, has been shown to induce faster apatite growth [258, 259]. Furthermore, hydrogels modified to enhance cell–material interactions has been shown to accelerate extracellular matrix (ECM) deposition and biomineralization. Herein, we have utilized chondroitin sulfate (CS) as a backbone polymer for hydrogel formation and their potential application in bone tissue engineering. CS is ubiquitous glycosaminoglycan (GAGs) and part of the non-collagenous ECM in human bone[260]. The major role of CS within bone tissue is to coordinate osteoblastic cell attachment and indirectly involve in bone homeostasis [261]. Furthermore, stem cell lineage commitment and differentiation are regulated by the presence of CS in the niche of bone marrow stem cells [262]. For this

reason CS-based hydrogels with all of these ideal characteristics can serve as an ECM to provide structural support to the newly formed bone.

Previous studies on CS-based hydrogels have been solely focused on its biochemical properties and the role of CS in bone formation has not been elucidated [263-267]. In this study, we evaluated the interaction between CS-based hydrogel and its surrounding environment. In particular, we focused on the interaction between negatively charged molecules within hydrogel with nearby ions for ion recruitment and biomineralization kinetics. Through this study, we sought to elucidate ion recruitment and biomineralization and gain insight into the bone stimulating scaffold design for potential clinical application.

## **3.2 Materials and methods**

### **3.2.1 Preparation of methacrylate-chondroitin sulfate**

Chondroitin sulfate powder (CS; C0335, Tokyo chemical industry Co., Ltd.) was reacted glycidyl methacrylate solution (GMA; 73 mM, Sigma-Aldrich) to conjugate meth acrylate functional groups as previously described [268]. Briefly, CS was dissolved in phosphate-

buffered saline (PBS; pH 7.4, Gibco) with 10% w/v and reacted with GMA (73 mM) for 11 days. Methacrylated CS (MeCS) was then purified by dialysis membrane (3.5K MW; SnakeSkin) for 48 h, followed by free-drying, and then preserved at -20°C for long term storage. After preparation, products were analyzed via <sup>1</sup>H-NMR spectra by dissolving in deuterium oxide for solvent.

### **3.2.2 Preparation of hydrogel by photoencapsulation**

Both poly (ethylene glycol) diacrylate (PEGDA, MW=3,400; SunBio, Inc.) and synthesized MeCS were dissolved in PBS with concentration of 20% w/v separately. Then both solutions were mixed with final concentration of MeCS as 0, 1, 5, and 10% w/v. Cells were gently mixed with the polymer solution and mixture solution is polymerized with photoinitiator (Irgacure 2959, 0.05% w/v) using UV light (3.5 mW/cm<sup>2</sup>) for 5 min (Fig. 3.1a). The constructs were maintained at 37°C with 5% CO<sub>2</sub> with cell culture medium for certain time.

### **3.2.3 Infrared spectroscopy**

Specific chemical bonding structures were investigated by Attenuated Total Reflection-Fourier Transform Infrared (ATR-FTIR, TENSOR27, Bruker Corporation) with the range of 800 to 4000  $\text{cm}^{-1}$  at a 4  $\text{cm}^{-1}$  resolution. Each groups of the dried hydrogel were placed on the diamond plate and measured with 50 scans. IR peaks corresponding to PEGDA and MeCS related chemical structure was analyzed.

### **3.2.4 Zeta potential analysis**

Synthesized hydrogel microparticle samples were dispersed in distilled water by sonication. The pH of the solutions was titrated from pH 2 to 9, using NaOH and HCl solution. The surface charge was measured with a zeta potential analyzer (Otsuka Model ELS-Z, Otsuka Electronics Co.).

### **3.2.5 Swelling and mechanical properties**

For each hydrogel, constructs were swollen and weighted in equilibrium-swollen state by PBS. The constructs were subsequently lyophilized to

remove the retained water to obtain the dry weight. Swelling ratio (Q) was the calculated from the wet weight over dry weight [269] as follows:

$$Q (\%) = \frac{\text{weight of the equilibrated hydrogel in PBS}}{\text{weight of the dried hydrogel}} \times 100$$

For enzymatic degradation profile, each sample (diameter of 6 mm and a height of 4 mm) was fabricated and incubated in enzyme-containing solution (0.5 U/mL, chondroitinase ABC; H3506; Sigma-Aldrich) at 37°C. The weight remained of each sample was measured up to 9 days. Enzyme-containing solution was changed for every 3 days. For mechanical properties, hydrogels were equilibrated in PBS for 24 h and compression tests were performed using Instron (Instron 5966, Instron Corporation) with a 10-kN-load cell. The load, stress and strain values were recorded to calculate the young's modulus.

### **3.2.6 Scanning electron microscopy and calcium accumulation assays**

The porous structure of the hydrogel was characterized by Field Emission Scanning Electron Microscopy (FE-SEM; JSM6701F, JEOL, Japan). After lyophilized, the samples were coated by platinum

sputtering and observed. For identifying each ion deposition on hydrogel, elemental mapping of energy dispersive spectroscopy (EDS) was observed. The samples were fabricated and soaked in 5mM CaCl<sub>2</sub> (dissolved in DI water and medium) solution and detected. To verify the accumulation of calcium and phosphate ions *in vitro* environment, each groups of hydrogels were soaked in 5mM of calcium included osteogenic medium for 21 days, then lyophilized in order to detecting each ions *via* X-ray photoelectron spectroscopy (XPS, K-alpha, Thermo VG Scientific, Massachusetts, USA). Al K $\alpha$  X-ray radiation source (200W, 12kV, KE = 1486.6eV) was used to record the photoelectron spectra under an ultra-high vacuum. XPS spectra were recorded in the 0 – 1100eV range with a resolution of 1.0eV and pass energy of 50eV. XPS high resolution scans of each atom were performed using the Advantage data system (Thermo VG Scientific, Massachusetts, USA).

### **3.2.7 Fluorescence assay for calcium determination**

Indo 1-AM (I3261, Sigma-Aldrich) fluorescence assay was performed to analyze Ca<sup>2+</sup> accumulation on each group of hydrogel under

manufacturer's protocol. Briefly, Indo 1-AM stock solution (1 mM, dissolved in DMSO) was diluted to 10  $\mu$ M (100  $\mu$ L). The each group of hydrogels were incubated in 5 mM CaCl<sub>2</sub> solution for 21 days, then were smashed and reacted with the Indo 1-AM solution at 37°C for 30 min. After centrifuged to settle down the hydrogel fragments, solution was detected with wavelength of excitation ( $\lambda_{ex}$ ) of 330 nm, and emission wavelength ( $\lambda_{em}$ ) was observed in range of 370-390 nm for reacted Ca<sup>2+</sup> ion and 450-470 nm for unreacted Ca<sup>2+</sup> ion, respectively.

### **3.2.8 Ammonium molybdate assay for phosphate determination**

For confirmation of phosphate deposition on the hydrogels, molybdate reagent solution (69888, Sigma-Aldrich) was used as manufacturer's protocol. Standard curve of phosphate was prepared by potassium phosphate dibasic trihydrate (K<sub>2</sub>HPO<sub>4</sub>·3H<sub>2</sub>O, Sigma-Aldrich) with a concentration between 20  $\mu$ M and 2 mM. The MeCS hydrogels (0, 1, 5, and 10% w/v) incubated in 5mM Ca<sup>2+</sup> included medium were smashed. Then molybdate reagent solution, ascorbic acid (Sigma-Aldrich, 10 %),

and distilled water were mixed with a volumetric ratio of 2:1:2 and reacted with hydrogel fragments at 37°C for 90 min. After reaction, absorbance of each sample was measured at 820 nm.

### **3.2.9 *In vitro* apatite forming ability**

The apatite forming ability of the hydrogels was investigated with immersed in Simulated Body Fluid (SBF) solution. The polymeric solution was polymerized within plastic mold with a diameter of 6 mm and a volume of 40  $\mu$ L. These hydrogels were soaked in SBF solution and incubated at 37°C for a week and 2 weeks, followed by washing the hydrogel with D.I. water and lyophilized. The constructs were prepared for characterizing the formed apatite through Electron microscopy and EDS.

### **3.2.10 Cell-encapsulated hydrogel preparation and viability**

Human tonsil-derived mesenchymal stem cells (hTMSCs) were obtained from Ewha Womans University Medical Center, Seoul Korea. The reagents that used for *in vitro* studies were from Gibco if a word otherwise was not mentioned. hTMSCs were cultured in tonsil growth medium (Dulbecco's modified Eagle's medium; DMEM), which contained 10% fetal bovine serum (FBS; 10438-026), 1% penicillin-streptomycin (15140122), 1% L-glutamine (25030-081), 1% anti-anti (15240-062). After trypsinized,  $1 \times 10^6$  cells were suspended in the polymeric solution. 40  $\mu$ L of cell-suspended polymeric solution were pipetted to plastic mold with a diameter of 6 mm and exposed to UV light ( $3.5 \text{ mW/cm}^2$ ) for 5 min. The hydrogel were incubated in tonsil osteogenic medium (OM), which contained DMEM, 10% FBS, 1% penicillin-streptomycin, 1.5 % dexamethasone (100X), 1.5% ascorbic-2-phosphate (100X), and glycerol-2-phosphate (1mM, Sigma-Aldrich), at  $37^\circ\text{C}$  with 5%  $\text{CO}_2$  for *in vitro* and *in vivo* study. For viability test, the samples, which incubated for day 1 and 21, were characterized by Live/Dead assay kit (L3224, Invitrogen) that consist of calcein-AM (green) and ethidium homodimer-1 (EthD-1, red) with used as a concentration of 0.5  $\mu$ L and 2  $\mu$ L per 1 mL PBS, respectively. Images

were obtained using fluorescence microscope (AMF4300, EVOS, Life Technology), and viability was calculated as the number of live cells per the number of total cells.

### **3.2.11 Gene expression analysis**

Cell-laden hydrogel incubated with 5 mM Ca<sup>2+</sup> included osteogenic medium for 21 days were crushed and subsequently total RNAs were extracted by Trizol (n=4). Using the SuperScript Synthesis System (Invitrogen), extracted RNAs were reverse transcribed into cDNA, followed by real-time PCRs through the SYBR<sup>®</sup> Green PCR Master mix and the ABI StepOnePlus<sup>™</sup> Real-Time PCR system (Applied Biosystems). cDNA samples with a concentration of 100 ng per 1 µL for total volume of 20 µL per reaction were used for analyzing genes and *GAPDH* as housekeeping gene. The primers for interested genes were shown in Table 3.1.

Gene	Primer 5'-3'
<i>GAPDH</i>	F: TGT TGT GGA TCT GAC CTG CC R: TTC TTA GTG TGG CGG AGA TG
<i>RunX2</i>	F: ACT GGG CCC TTT TTC AGA R: GCG GAA GCA TTC TGG AA
<i>OCN</i>	F: GCC TTT GTG TCC AAG C R: GGA CCC CAC ATC CAT AG
<i>ALP</i>	F: ACG TGG CTA AGA ATG TCA TC R: CTG GTA GGC GAT GTC CTT A
<i>Col I</i>	F: ACG AGG CCT GAC AGG TCC CA R: GCC CAG CAA ATC CCG CTG GT

**Table 3.1** Primer sets for human genes used in this study. *GAPDH* was used as a housekeeping gene. [Alkaline phosphatase (*ALP*), type 1 collagen (*Col 1*), osteocalcin (*OCN*), and Runt-related transcription factor 2 (*RunX2*)]

### **3.2.12 Ethics statement**

All experiments were maintained and cared in accordance with the Guide for the Care and Use of Laboratory Animals by the Seoul National University. All operations were performed under Zoletil 50 (Virbac) and Rompun<sup>®</sup>inj (Bayer) anesthesia, and all endeavors were established to minimize animal suffering.

### **3.2.13 Calvarial defect procedure and *in vivo* cell-laden hydrogel transplantation**

Female BALB/c mice (OrientBio Co., Republic of Korea) with 6 weeks were used for the animal experiments. After incubated for 1 week *in vitro*, the hTMSCs-laden hydrogels (0, 1, 5, and 10% MeCS) were prepared for *in vivo* implantation. After the mice were anesthetized, skin of surgical site was opened and calvarial defect was made using 4 mm diameter drills. The cell-encapsulated hydrogels were implanted to defect region, followed by suturing the skin. The animals were

monitored and harvested 8 weeks after implantation. Animals were assigned into four groups (0, 1, 5, and 10% MeCS).

### **3.2.14 Micro-CT analysis**

Micro-CT analysis was used to estimate volume of bone regeneration within the cell-laden hydrogel. The animals were sacrificed with a CO<sub>2</sub> after 8 weeks, followed by collecting the defected site. The samples were fixed with 10% buffered formaldehyde for 2 days. The topographies of fixed hydrogels were performed using SkyScan 1172 (SkyScan, Belgium) at 59 kV, 167 μA, and an exposure time of 40 ms through non-filter. Volume and surface area of bone regeneration was estimated as follows:

$$\frac{BV(BS)}{TV(TS)} = \frac{\text{Regenerated Volume (Surface)}}{\text{Total Volume (Surface)}} \times 100$$

### **3.2.15 Statistical analysis**

Quantitative data were expressed as means  $\pm$  standard deviations. Each experiment was conducted with more than 3 samples if a word otherwise was not mentioned. Statistical significance was estimated by paired student's *t*-test and *p* values less than 0.05 were considered statistically significant (\**p*<0.05, \*\**p*<0.01, and \*\*\**p*<0.001).

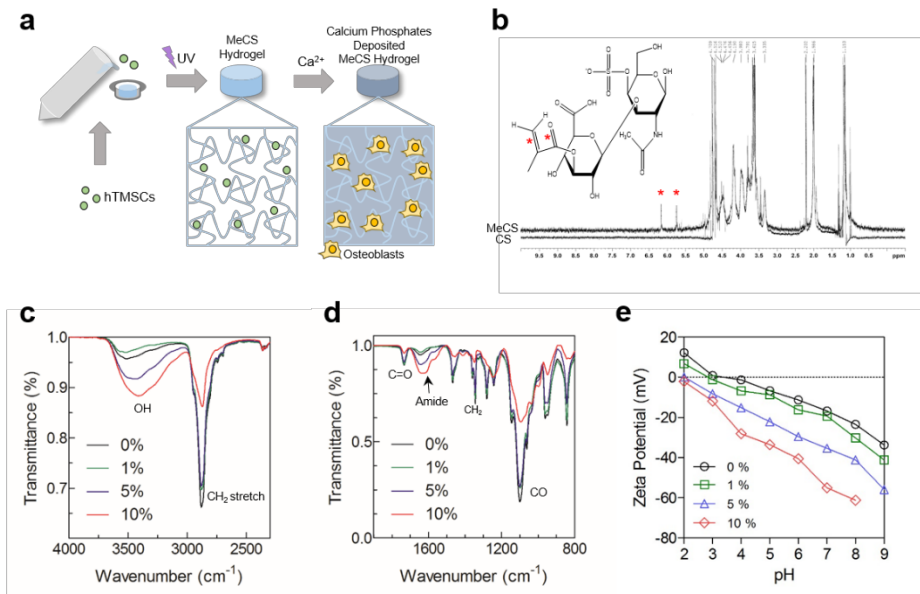


**Figure 3.1** Preparation of PEGDA-MeCS hydrogel used for osteogenic differentiation of hTMSCs. The hTMSCs were encapsulated into negatively charged MeCS hydrogel for osteogenic differentiation (a). The MeCS synthesis was confirmed using <sup>1</sup>H NMR analysis with CS as control (b). As preparing a serial concentration of MeCS with PEGDA (0, 1, 5, and 10 %), chemical bonding structure and its intensity of the hydrogels were estimated using ATR-FTIR at about 2500 to 4000 cm<sup>-1</sup> (c) and 800 to 1800 cm<sup>-1</sup> (d). The higher intensity of peaks corresponding to MeCS was revealed as increasing the MeCS contents, whereas lower intensity of PEGDA-peaks was detected. Surface zeta potential of hydrogel (0, 1, 5, 10 %) was measured that zeta potential become more negative as CS concentration increases (e).

### 3.3 Results

#### 3.3.1 Synthesis and characterization of methacrylated chondroitin sulfate hydrogel

To synthesize a biomineralizing CS-based hydrogel, CS was chemically modified with methacrylate functional group. In figure 3.1b, both peaks at 6.207 and 5.768 ppm corresponding to vinyl protons were observed, indicating that methacrylated CS (MeCS) was successfully synthesized via  $^1\text{H-NMR}$  analysis (Fig 3.1a, b). To further identify the presence of other functional groups, ATR-FTIR analysis was performed on pre-polymerized solution with serial concentrations of MeCS solution (1, 5, and 10 w/v of 1% of MeCS per pre-polymeric 20% PEGDA solution). The transmittance of PEGDA solution alone showed  $-\text{CH}_2$  stretching,  $-\text{C}=\text{O}$  stretching,  $-\text{CH}_2$  bending, and  $-\text{C}-\text{O}-$  stretching, at 2,850, 1,726, 1,342, and 1,098  $\text{cm}^{-1}$ , respectively. Percent transmittance of PEGDA specific peaks was reduced when MeCS solution volume was incremented (Fig 3.1c and d). In response to increased MeCS solution, an overlap of  $-\text{OH}$  and  $-\text{NH}$  bonds at 3,436  $\text{cm}^{-1}$  and an amide peak at 1,636  $\text{cm}^{-1}$  were profoundly observed. After that, the CS-based hydrogel was synthesized by photoinitiator using UV light for 5 min. The

hydrogel constructs were maintained at 37°C with 5% CO<sub>2</sub> in cell culture medium.

We further characterized CS-dependent charge distribution within hydrogel by zeta potential analysis (Figure 3.1e). CS-based hydrogels with varying MeCS concentrations were polymerized with ammonium persulfate (APS) and tetramethylenethylenediamine (TEMED). Prior to measurement, hydrogels were swollen in distilled (DI) water for overnight and lyophilized. Lyophilized hydrogels were chopped by sonication and were re-swollen by DI water. Charge distribution of 10% MeCS-hydrogel presented -2.123 to -61.23 mV and PEGDA hydrogel alone displayed 12.2 to -33.7 mV. Therefore, charge measurement shows higher concentration of CS group within hydrogel results additive negatively surface charge throughout pH 2 to 9 (Fig. 3.1e).

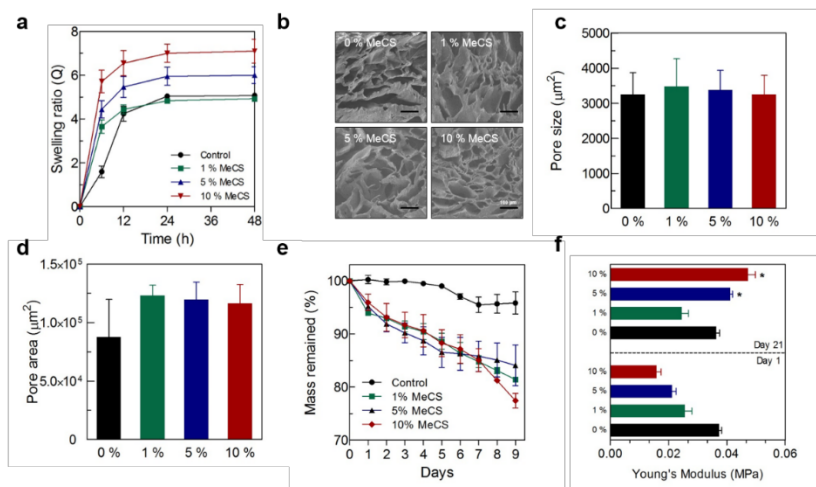


**Figure 3.2** Characterization of prepared PEGDA-MeCS hydrogels. Swelling ratio of hydrogels with a various MeCS concentration was measured and the values were increased in MeCS-rich (5 and 10 %) groups (a). The porous structure of hydrogels was observed using SEM and it revealed the hydrogels in all groups had highly porous structure, which allowed the hTMSCs to be encapsulated (b). Pore size and area were measured throughout the MeCS hydrogel groups (c-d). The hydrogels with higher portion of MeCS showed faster degradation than with lower portion of MeCS in chondroitinase enzyme solution containing (0.5 U/mL) enzymatic solution (e). Young's modulus of the hydrogels was increased significantly after incubated in 5 mM Ca<sup>2+</sup> environment in the case of MeCS-rich groups, which suggested that the negatively charged MeCS bound the Ca<sup>2+</sup> ions, followed by calcification (f). In a-f, n = 4. \**p* < 0.05, \*\**p* < 0.001. \*\*\**p* < 0.0001.

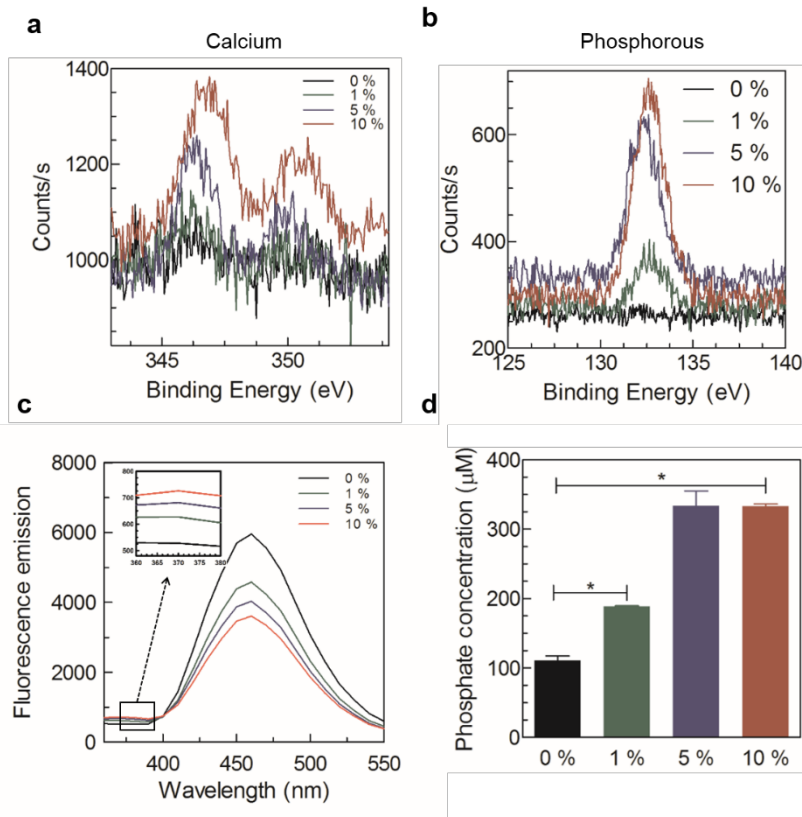


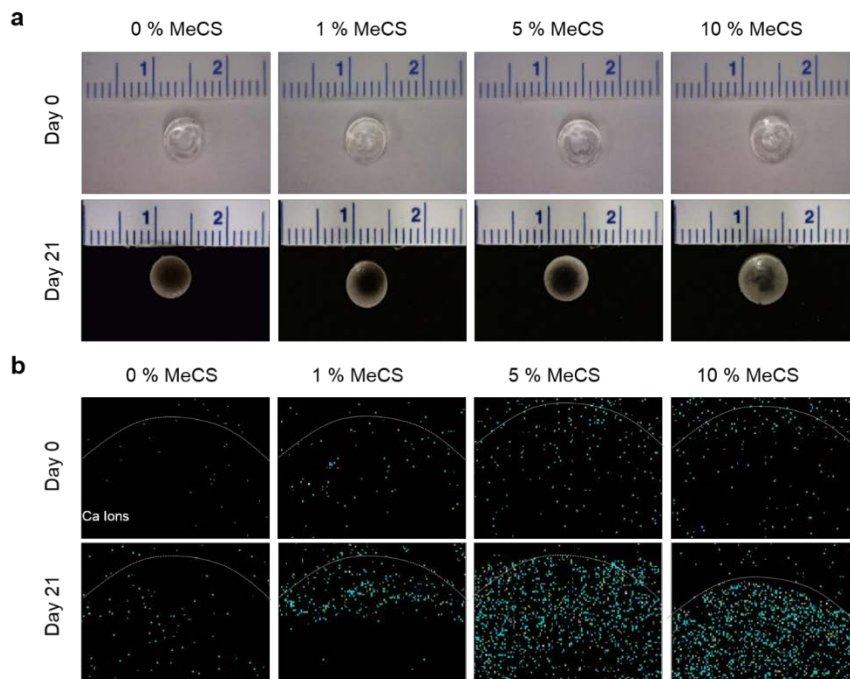
**Figure 3.3** Calcium and Phosphate Ion bound by MeCS Hydrogel. The XPS analysis on MeCS hydrogels indicated that the negatively charged MeCS attracted chemical element Ca (a) and resulted in binding phosphate (b). Indo 1-AM assay also revealed the strong intensity of  $\text{Ca}^{2+}$  binding range in the case of MeCS-rich groups (c). Moreover, the ammonium molybdate assay for detecting phosphate ions suggested that MeCS-rich hydrogels had more P ions as well as Ca ions (d). In d,  $n = 6$ . \* $p < 0.05$ , \*\* $p < 0.001$ . \*\*\* $p < 0.0001$ .

### **3.3.2 Calcium and phosphate ion deposition on CS-based hydrogel**

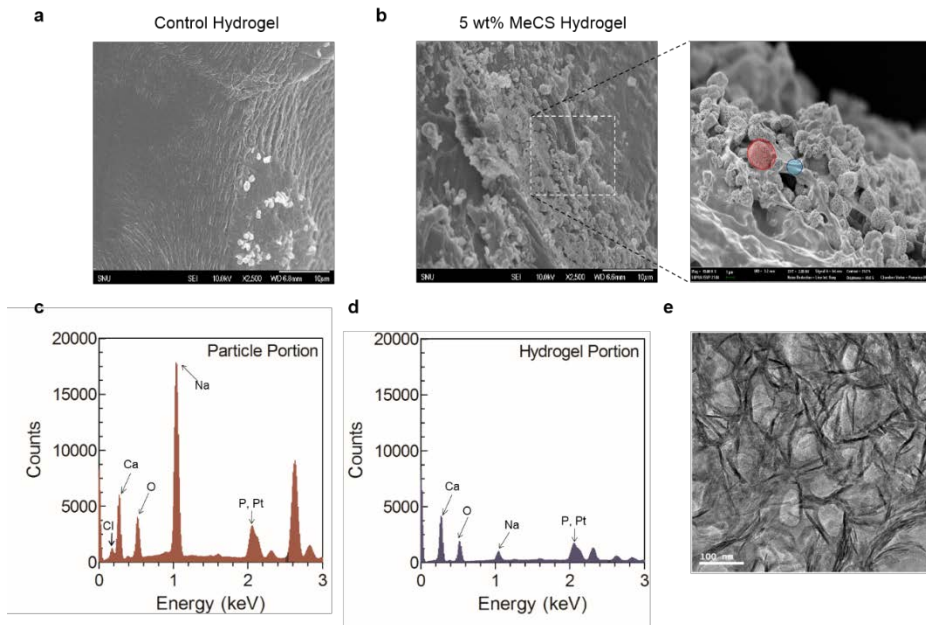
Since sulfate groups create a negative charge, CS is able to bind positive ions and proteins[270]; thus, we quantified calcium and phosphate ion accumulation by placing CS-based hydrogels in PBS with 5 mM  $\text{Ca}^{2+}$  and  $\text{PO}_4^-$ . After incubation up to 21 days, we performed X-ray photoelectron spectroscopy (XPS) analysis to detect binding energy related to calcium and phosphate ions around CS-based hydrogels. Results showed several peaks corresponding to each ion, the intensity of which gradually increased as MeCS concentration increased from 0 to 10% (Fig 3.3a and b).

In addition to XPS analyses, free  $\text{Ca}^{2+}$  concentration in hydrogels was estimated using Indo 1-AM calcium sensitive dye which showed similar trends to XPS in terms of the amount of reacting calcium ions in hydrogels. Indo 1-AM emits fluorescence at 380 nm and 450 nm with and without conjugated calcium ions. Moreover, a relatively high amount of unreacted Indo 1-AM was detected in low concentration of CS-based hydrogels, and vice versa (Fig 3.3c). For the phosphate accumulation analysis, we performed the ammonium

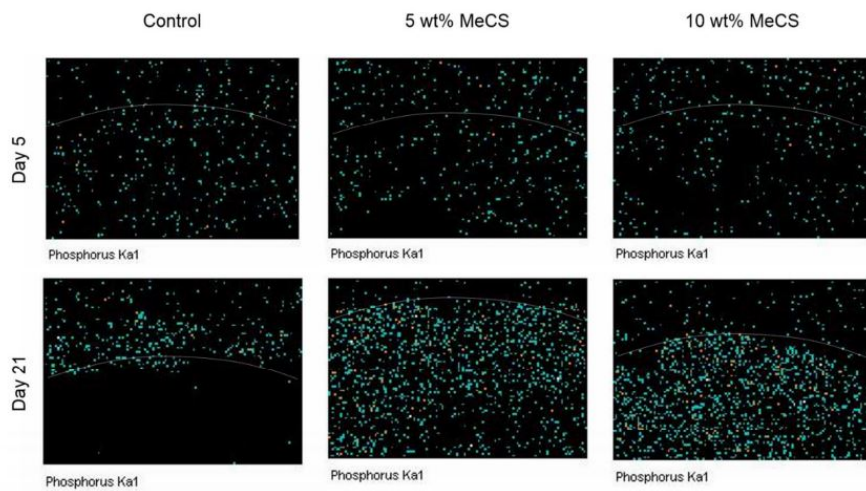
molybdate/ascorbic acid spectrophotometric assay. Since free phosphate ions reacts with ammonium molybdate to give phosphomolybdeum blue, the more phosphate ion synthesizes the more phosphomolybdeum become blue. From the calculation, 5 and 10% CS-based hydrogels have more than 300 $\mu$ M of free phosphate ions, which are three times higher than 0% PEGDA hydrogel only (Fig 3.3d).



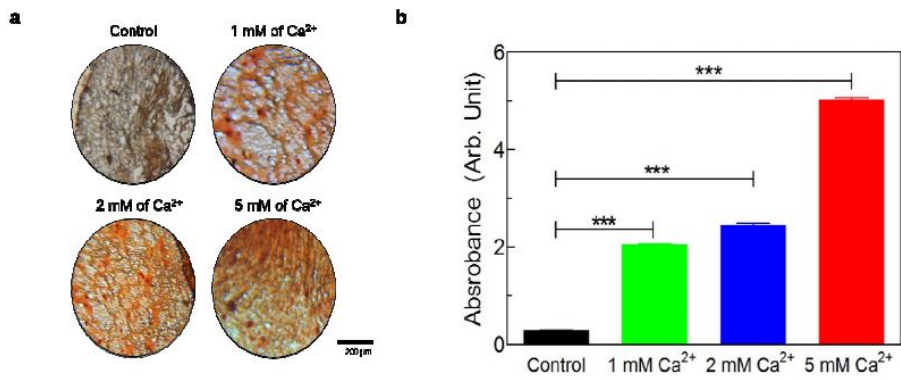
**Figure 3.4 Confirmation of accumulated Ca and Phosphate ions.** The calcified regions on the cell-laden hydrogels were shown when the hydrogel were incubated in 5 mM  $\text{Ca}^{2+}$  included cell culture medium for 21 days (a). The Ca ions were detected in these regions with EDS elemental mapping, and the higher amount of Ca ions were observed in MeCS-rich groups after incubated 21 days (b, dotted line represents the boundary of the hydrogel constructs)



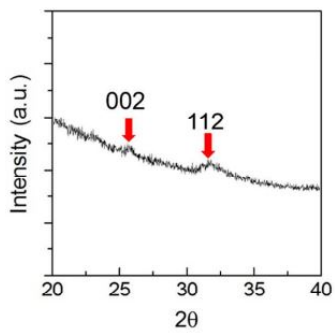
**Figure 3.5** *In vitro* calcium phosphate (CaP) forming ability and differentiation of hTMSCs. Calcium phosphate crystals were hardly formed on control groups (PEGDA, a), whereas a number of apatite particles could be observed in 5% MeCS hydrogels and high magnification of square box (b). Using SEM/EDS spot analysis, the chemical composition of both regions with and without particles was characterized that the particles was mainly composed of Ca and P ions (c-d). TEM analysis confirmed that these calcium phosphate has a hydroxyapatite crystalline structure (e).



**Figure 3.6** Detection of accumulated phosphorous element within MeCS-rich hydrogels via EDS elemental mapping



**Figure 3.7** Detection of accumulated calcium ions on MeCS hydrogels by Alizarlin's staining.

**a****b**

Ca 2s	P 2s	Ca/P
61.93%	38.07%	1.6267

**Figure 3.8** X-ray diffraction pattern of hydroxyapatite accumulated onto the surface of MeCS hydrogel (a), and its calcium/phosphate ratio (b)

### **3.3.3 In situ formation of calcium phosphate derivatives on the surface of CS-based hydrogels**

Not only ion binding to CS-based hydrogel was confirmed, but interestingly, “white particulate coating” also formed on surface of the hydrogel. (Fig 3.4a). We hypothesized this white particulate to be calcium phosphates (CaPs), and to further analyze composition of these particulate coating, boundaries were visualized *via* energy dispersive X-ray spectrometry (EDS) elemental mapping at 5 and 21 days of incubation (Fig 3.4b and 3.6). As MeCS concentration increased, greater amounts of calcium and phosphate ions (green dots) were detected at the peripheries of hydrogels. This phenomena was also confirmed by alizarin red S in which an intense red color was observed in MeCS-rich groups (Fig. 3.7a and b).

To confirm these white depositions are *in vitro* formation of CaP derivatives, 0 and 5% MeCS hydrogel samples were investigated by SEM analyses. 5% MeCS group exhibited rough surfaces compared to 0 % control hydrogel and a large amount of particles were deposited on the surface (Fig 3.5a and b). To characterize these particles, we performed EDS analysis between particles and hydrogel surfaces.

Particles (red circle) contained higher amounts of calcium, oxygen and phosphate ions compared to hydrogel surface (blue circle) (Fig 3.5c and d). From HR-TEM diffraction analyses, newly precipitated CaP had a hydroxyapatite (HAP) crystal structure, indicating that surface of CS-based hydrogel can stimulate HAP formation (Fig 3.5e). Moreover, XRD performed on the hydrogel with CaP particles confirmed the expected Ca/P ratio (~1.63) and typical reflections, (0 0 2) and (1 1 2), for crystalline HAP (Figure 3.8).

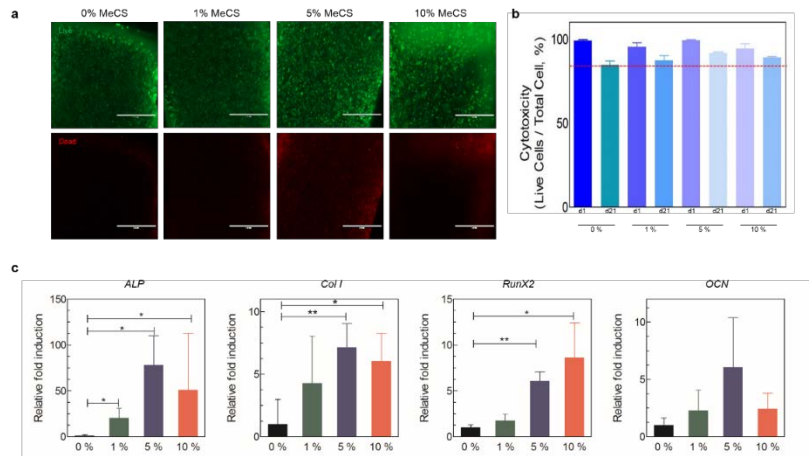


**Figure 3.9** *In vitro* cell studies on MeCS Hydrogel. Encapsulated hTMSCs was identified with Live/Dead fluorescent assay (Green; Live, Red; Dead) (a), and it had moderate viability until 21 days (b). Osteogenic genes were expressed with higher levels within MeCS-rich hydrogels (c). In c, n = 3. \* $p < 0.05$ , \*\* $p < 0.001$ . \*\*\* $p < 0.0001$ .

### **3.3.4 *In vitro* biocompatibility and gene expression profiles of hTMSCs**

For examining cytotoxicity from hydrogels, Live/Dead viability assay was performed with stem cells (Fig 3.9a). All scaffolds supported tonsil mesenchymal stem cells (hTMSCs) viability over 2 days of culture. Quantitative analysis of cell viability showed that 84.8% of encapsulated cells showed moderate viability after 21 days of culture (Fig 3.9b). Since biomaterials containing CaP moieties have been shown to support osteogenic differentiation of stem and progenitor cells and bone tissue formation, we further compared the mineral microenvironment-dependent osteogenic differentiation of hTMSCs. Prior to cell seeding, they hydrogels were mineralized in PBS with 5 mM calcium and phosphate ions. hTMSCs cultured with osteogenic medium on the surface of 4 different groups of hydrogels. On day 14 of hTMSCs differentiation, quantitative Real time-PCR analysis of osteo-specific genes, such as the runt-related transcription factor 2 (*RUNX2*), osteocalcin (*OCN*), alkaline phosphatase (*ALP*) and collagen type I (*COL I*) confirmed that the expression of all four genes were significantly upregulated in hydrogels with higher concentrations of CS (Fig 3.9c).

Specifically, cells grown in 5% and 10% MeCS hydrogels had relatively higher (> 50 times higher) *ALP* and *RUNX2* expression than those grown in 0% and 5 % MeCS hydrogels.

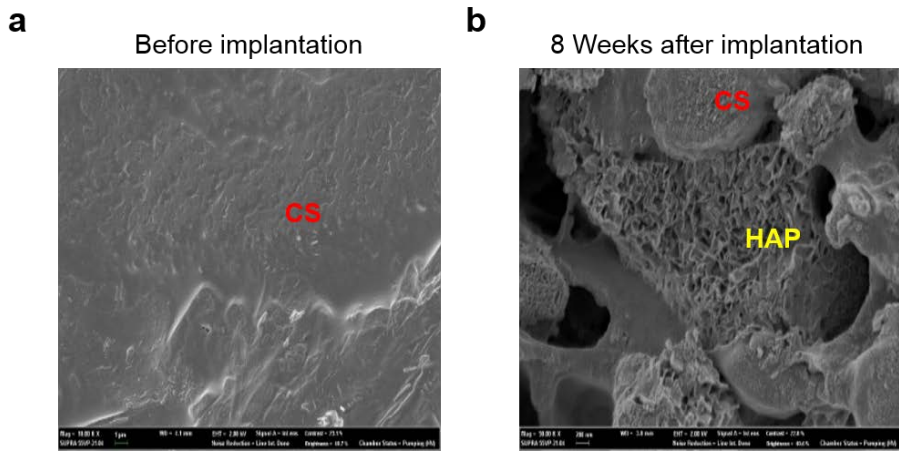


**Figure 3.10** *In vivo* hydroxyapatite forming. (e) *In vivo* formation of bone mineral MeCS gel implant, After 8 weeks, surface morphology of the hydrogels was observed with SEM, which revealed that hydroxyapatites were formed within the collected specimen (b).

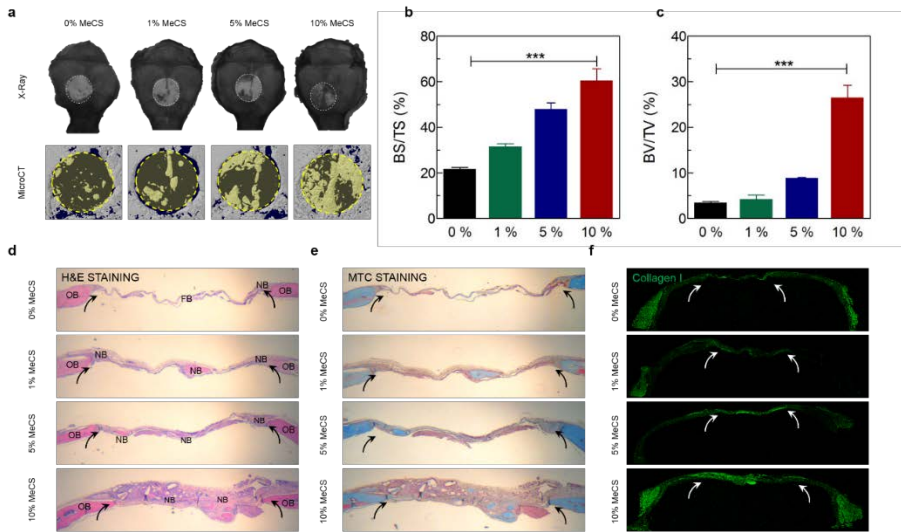


**Figure 3.11** *In vivo* transplantation and bone regeneration. The cell-laden hydrogels were transplanted into mouse cranial defect models, which were created using 4 mm-diameter drill and covered with the hydrogels. Bone regeneration was confirmed with MicroCT images of the cranial tissue after 8 weeks implantation (a) and the regenerative rates in terms of both surface area and volume were calculated (b-c). Histomorphometric analysis with H&E staining (d), MTC (e), and Collagen I staining of implants and tissue specimens. In b-c,  $n = 4$ . \* $p < 0.05$ , \*\* $p < 0.001$ . \*\*\* $p < 0.0001$ .

### **3.3.5 *In vivo* bone tissue regeneration of cell-laden hydrogels**

Next, we examined whether these MeCS hydrogels could serve as a bone scaffold materials *in vivo*. To estimate *in vivo* bone tissue regeneration, a calvarial defect model were prepared using 6-week-old mice, and synthesized acellular MeCS hydrogels were applied to the defect area for 8 weeks as well as subcutaneous injection (Fig 3.10a). After 8 weeks, a rough morphology with bone-like apatite was created on the surface of the MeCS hydrogel (Fig 3.10b). For quantitative analysis, each defect area and scaffolds were analyzed by micro-CT (Fig 3.11a). Among the groups, 5% and 10% hydrogels have two- to threefold higher regenerated volume and area than in the controls by post-mathematical pixel reconstruction (volume  $8.82 \pm 0.26\%$  and  $12.36 \pm 0.87\%$  and area  $20.70 \pm 0.50\%$  and  $29.12 \pm 0.77\%$ , respectively (Fig 3.11b and c).

After removing the hydrogel portion, H&E and Masson's trichrome staining revealed that 10% MeCS hydrogel group had highly integrated with the native bone tissue (OB), and the hydrogel was thoroughly infiltrated by the cells showing osteoconductivity to its material (Fig 3.11d and e). Analysis of the staining images showed

maximum amount of bone formation (NB) in the 10 % MeCS hydrogel group in which the mineralized tissue development and osteocyte cell infiltration could be observed at focal sites in the defect area (between black arrows) with ossification occurring around the material. In the 1 and 5 % MeCS hydrogel groups, the amount of mineralized tissue formed was less than 10 % MeCS group and there is limited amount of cell infiltration and its interconnectivity throughout the scaffold. Mineralization and defect filling were the lowest in the 0 % MeCS hydrogel group where only bone formation, which happened, was at the periphery of the defect site, while rest of the defect was filled with fibrous tissue (FB) only. Moreover, we have performed the immunostaining of defect area for Col-I (Fig 3.11). Staining was homogeneously distributed for 10 % MeCS hydrogel throughout the entire defect area (white arrows) of the mineralized scaffold sections, whereas in 0 and 1 % MeCS hydrogel, with minimum of premineralization, positive staining was mostly restricted to the scaffold surface and detected amount was insignificant compared to the 5 and 10 % MeCS group. MTC and Col-I immunostaining directly indicated an

increase in bone matrix deposition over time for different concentration of MeCS.

### **3.4 Discussion**

During the bone regeneration, biomineralization is an important process to harden or stiffen existing tissues. The most common biominerals are the calcium and phosphate that formed apatite crystals in combining with organic polymer such as collagen fibrils to give structural support to our bones. The collagen can control CaP nucleation with the negatively charged amino acids acting as nucleation sites for apatite formation [271]. In this study, we utilized CS as a nucleation site and describe the development of CS-based hydrogel for application in bone tissue engineering. In addition, we also demonstrate the effective biomineralization by CS-based hydrogels via effective initial recruitment of positive calcium ions. Our study also suggests that the accumulated calcium ions attracted the following negative ions such as phosphate for mineralized calcium phosphates (CaPs) deposition, resulting in accelerated biomineralization process.

Our group previously demonstrated the use of acrylate-based photo-polymerization to modify a methacrylate group onto the CS backbone to synthesize hydrogel scaffold.[272] A major factor that influences hydrogel sensitivity of surroundings is the properties of the polymer [273, 274]. Increasing fraction of MeCS in hydrogel and its hydrophilicity was easily distinguishable by their FTIR peaks, due to greater exposing of hydroxyl and amide groups (Fig 3.2c and d). To evaluate the sensitivity of the hydrogel by surrounding factors, the swelling ratio was measured in a timely manner. The swelling behavior of hydrogels is affected by the hydrophilic group present in the polymer chains. We demonstrated that the swelling ratio increased along with higher MeCS fraction, which indicated that higher fraction of MeCS contains more hydroxyl group within their backbone, providing more hydrogen bonds to the environments, and thereby absorb much more water with greater amount of surrounding ions.

The biomineralization of the hydrogels is also modulated by the electrostatic interactions. Negatively charged sulfate group on MeCS hydrogel selectively attracts positively charged ions such as calcium or sodium from the environment, which eventually allows neutralizing

phosphate and carbonate ions, which the permit further calcium ion binding to the surface (Scheme 1). The driving force is, therefore, the affinity of calcium ions to negatively charged sulfate surface for the neutral nucleation sites [275]. Moreover, when MeCS hydrogels degrade by enzymes such as chondroitinase *in vitro* accelerate the immobilization of minerals via the *in situ* formation of insoluble CaP by free CS polymer reaction with free calcium ion present because, in the normal physiological condition, phosphate exists in a state of metastable equilibrium. This equilibrium may shift phosphate on contact with the surface of hydrogel, resulting in local CaP precipitation [276, 277]. Higher concentrations of MeCS also triggered much faster degradation of hydrogel in enzymatic solution, which can expect their better degradability *in vivo* (Fig 3.3e).

Furthermore, the degradation of hydrogel helps physically anchor the CaP by replacing the site and prevents the biomineral from being extracted out of the hydrogel [277]. According to our data, after incubating hydrogels for 3 weeks in culture media, the compressive modulus was significantly increased in higher concentration of MeCS hydrogel by the accumulation of CaP layer around the edges (Figure 3.3f

and 4). An increased CaP derivatives are associated with increased mechanical abilities, such as the ratio of hardness and modulus[278]. Even though, the local strain varied along the long axis of the hydrogel scaffold, the modulus of the scaffold theoretically matched that of mineralized bone tissue.[279]

According to other research groups, the scaffolds were alternately soaked in SBF solution, which are containing calcium and phosphate-based to accelerate and mimic biomineralization.[280, 281] In our study, the effect of negatively charged hydrogels *in vitro* on apatite formation was successful without SBF solution treatment. Small CaP particles comprising from little amount of calcium and phosphate in medium accumulated on the surfaces of hydrogels with high MeCS concentrations (Fig 3.5b). The calcium and phosphorus peak intensities were comparable when deposited particles and hydrogel portions were determined by EDS analysis (Fig 3.5c and d).

Our XRD, EDS and TEM analysis indicate that these accumulated CaP biomineral display as a form of hydroxyapatite crystalline structure. From previous studies, it is known that the morphology of particles was dissimilar from naturally existed apatite

created on the surface of metals and/or ceramic-containing materials[282, 283]. However, interestingly, hydroxyapatite, naturally occurring mineral form of CaP, was formed on the surface of MeCS hydrogels *in vivo* following implantation (Fig 3.5e and Fig 3.8), which interprets that MeCS hydrogel attracted the ionic species relevant to naturally existed apatite formation and resulted in osteo-friendly environment.

This biomineralized matrix can provide high ion concentration niche to help osteogenic differentiation of stem cells and progenitor cells through SLC20a1 and Magt1 ion channel protein along with prevention of osteoclast activation [19]. This is accordance with our data that have implicated the role of CaP, in particular, upregulation of *ALP* and *RUNX2* gene expression as well as *Col I* and *OCN*, on osteogenic differentiation markers of MSCs. Recently, CS-dependent bone homeostasis has been elucidated where CS mediates estrogen-induced osteoanabolic process in osteoporosis model[284]. These findings led to the idea that CS-based scaffold can provide not only the osteo-friendly environment but also optimal osteoanabolic milieu for estrogen-cadherin pathways[285]. Bone integration is another important criterion for biomineralizing scaffolds. Based on this findings, we transplanted MeCS hydrogels into

calvarial defect model, full integration of murine cranium was observed after 8 weeks. Micro-CT analysis indicated smooth contour and integration with surrounding native tissues, and BMD with histological analysis also confirmed that biomineralized hydrogel showed higher bone regeneration (Fig 3.11).

### **3.5 Summary**

The overall concept of this research is that negatively charged biomaterial, chondroitin sulfate, has potential to accumulate of ions, including calcium and phosphate to induce biomineralization process as well as osteogenic differentiation of hTMSCs *in vitro* and *in vivo*. MeCS hydrogel have potential as bone formation biomaterials and may useful for bone tissue engineering.

## **4 CHAPTER FOUR: CONCLUDING**

### **REMARKS**

#### **4.1 Summary**

In this thesis, in order to comprehend formation mechanism and function of the bone in living system, we investigated new types of calcium phosphate based on multi-disciplinary efforts that imparts the concept of material science engineering, chemistry, physics and biology. We tried to provide our foundation mechanism with detailed biological cascade in order to inspire and induce subsequent studies of other researchers to further reveal unknown mechanism in our bone regeneration system.

In the first part of this dissertation, we have presented current technologies and types of biomimetic materials and reviewed fabrication approaches that are currently being utilized for biomimetic scaffold design. For successful bone tissue regeneration, a variety of materials has been investigated to fabricate the optimal scaffolds. A lot of biocompatible and biodegradable polymers have been explored to make bone scaffold frame, and osteoinductive materials such as metal ions, growth factors have been incorporated to bone scaffolds. Furthermore,

various techniques have been developed to construct the three dimensional porous bone scaffolds like natural bone tissue. Those traditional strategies have been innovated for years, and various cell sources optimized for osteogenesis have been applied to bone tissue engineering. In this way, we expected to overcome current challenges and critical-sized bone defects from accidents and diseases.

In the second part of the thesis, we have demonstrated that synthetic whitlockite (WH:  $\text{Ca}_{18}\text{Mg}_2(\text{HPO}_4)_2(\text{PO}_4)_{12}$ ) nanoparticles can recapitulate early-stage of bone regeneration through stimulating osteogenic differentiation, prohibiting osteoclastic activity, and transforming into mechanically enhanced hydroxyapatite (HAP)-neo bone tissues by continuous supply of  $\text{PO}_4^{3-}$  and  $\text{Mg}^{2+}$  under physiological conditions. In addition, based on their structural analysis, the dynamic phase transformation from WH into HAP contributed as a key factor for rapid bone regeneration with denser hierarchical neo-bone structure. Our findings suggest a groundbreaking concept of 'living bone minerals' that actively communicate with the surrounding system to induce self-healing, while previous notions about bone minerals have been limited to passive products of cellular mineralization.

In the last part of the thesis, we have fabricated methacrylated PEGDA/CS-based hydrogels with varying CS concentration and investigated them as biomineralizing three-dimensional scaffolds for charged ion binding and depositions. Due to its negative charge from the sulfate group, CS exhibited an osteogenically favorable microenvironment by binding charged ions such as calcium and phosphate. Particularly, ion binding and distribution within negatively charged hydrogel was dependent on CS concentration. Furthermore, CS dependent biomineralizing microenvironment induced osteogenic differentiation of human tonsil-derived mesenchymal stem cells *in vitro*. This PEGDA/CS-based biomineralizing hydrogel platform can be utilized for in situ bone formation in addition to being an investigational tool for *in vivo* bone mineralization and resorption mechanisms.

Biomimetic scaffold-mediated in situ bone remodeling and rapid bone regeneration in this thesis will be useful to understand the mechanism and the role of biomineral and biopolymer in the bone regeneration system. We believe that this study will directly contribute to make more bone-like scaffold or implants and provide inspiration and foundation knowledge to the other various research fields.

## **4.2 Further suggested research ideas**

In future study, we will follow up the previous researches by introducing a new calcium phosphate-based material, whitlockite (WH), in fabricating the scaffolds for bone tissue engineering through various additive materials [42, 43]. While a mineralized microenvironment around stem cells was confirmed by using WH nanoparticles, we are developing extra steps of bone formation by introducing a neovasculargenesis environment in order to enable blood vessel formation inside of bone scaffold, eventually supply continuous amount of nutrients, oxygen and growth factors since the building of new blood vessels during the bone formation process could facilitate to form an intact natural bone near scaffold [303-306]. Among various strategies to induce blood vessel formation, a well-known growth factor (VEGF) of both angiogenesis and vasculogenesis was preferred to derive neovascularization inducing blood friendly microenvironment [307-309]. This future work will aim to demonstrate the effect of vascularization on bone regeneration and the synergistic enhancement of osteogenesis on

hTMSCs by both vascularized and mineralized environment in our body system. Consequently, the microenvironment composed of these factors will propose possible clinical applications in bone tissue engineering and regenerative medicine for critical-sized bone defects.

## REFERENCE

- [1] A.D. Woolf, B. Pfleger, Burden of major musculoskeletal conditions, *B World Health Organ* 81(9) (2003) 646-656.
- [2] S. Robbins, C. Lauryssen, M.N. Songer, Use of Nanocrystalline Hydroxyapatite With Autologous BMA and Local Bone in the Lumbar Spine A Retrospective CT Analysis of Posterolateral Fusion Results, *Clin Spine Surg* 30(3) (2017) E192-E197.
- [3] A. Jamjoom, R.E. Cohen, Grafts for Ridge Preservation, *J Funct Biomater* 6(3) (2015) 833-48.
- [4] S. Bose, G. Fielding, S. Tarafder, A. Bandyopadhyay, Understanding of dopant-induced osteogenesis and angiogenesis in calcium phosphate ceramics, *Trends in biotechnology* 31(10) (2013) 594-605.
- [5] Y.R. Shih, Y. Hwang, A. Phadke, H. Kang, N.S. Hwang, E.J. Caro, S. Nguyen, M. Siu, E.A. Theodorakis, N.C. Gianneschi, K.S. Vecchio, S. Chien, O.K. Lee, S. Varghese, Calcium phosphate-bearing matrices induce osteogenic differentiation of stem cells through adenosine signaling, *Proceedings of the National Academy of Sciences of the United States of America* 111(3) (2014) 990-5.

- [6] P. Muller, U. Bulnheim, A. Diener, F. Luthen, M. Teller, E.D. Klinkenberg, H.G. Neumann, B. Nebe, A. Liebold, G. Steinhoff, J. Rychly, Calcium phosphate surfaces promote osteogenic differentiation of mesenchymal stem cells, *Journal of cellular and molecular medicine* 12(1) (2008) 281-91.
- [7] A. Dawidowicz, S. Pielka, D. Paluch, J. Kuryszko, J. Staniszevska-Kus, L. Solski, [Application of elemental microanalysis for estimation of osteoinduction and osteoconduction of hydroxyapatite bone implants], *Polimery w medycynie* 35(1) (2005) 3-14.
- [8] U. Ripamonti, L.C. Roden, L.F. Renton, Osteoinductive hydroxyapatite-coated titanium implants, *Biomaterials* 33(15) (2012) 3813-23.
- [9] J.R. Woodard, A.J. Hilldore, S.K. Lan, C.J. Park, A.W. Morgan, J.A. Eurell, S.G. Clark, M.B. Wheeler, R.D. Jamison, A.J. Wagoner Johnson, The mechanical properties and osteoconductivity of hydroxyapatite bone scaffolds with multi-scale porosity, *Biomaterials* 28(1) (2007) 45-54.
- [10] R. Family, M. Solati-Hashjin, S. Namjoy Nik, A. Nemati, Surface modification for titanium implants by hydroxyapatite nanocomposite, *Caspian J Intern Med* 3(3) (2012) 460-5.

- [11] C. Ohman, M. Baleani, C. Pani, F. Taddei, M. Alberghini, M. Viceconti, M. Manfrini, Compressive behaviour of child and adult cortical bone, *Bone* 49(4) (2011) 769-76.
- [12] C. Maes, T. Kobayashi, M.K. Selig, S. Torrekens, S.I. Roth, S. Mackem, G. Carmeliet, H.M. Kronenberg, Osteoblast precursors, but not mature osteoblasts, move into developing and fractured bones along with invading blood vessels, *Developmental cell* 19(2) (2010) 329-44.
- [13] B. Sacchetti, A. Funari, S. Michienzi, S. Di Cesare, S. Piersanti, I. Saggio, E. Tagliafico, S. Ferrari, P.G. Robey, M. Riminucci, P. Bianco, Self-renewing osteoprogenitors in bone marrow sinusoids can organize a hematopoietic microenvironment, *Cell* 131(2) (2007) 324-36.
- [14] V. Karageorgiou, D. Kaplan, Porosity of 3D biomaterial scaffolds and osteogenesis, *Biomaterials* 26(27) (2005) 5474-91.
- [15] New restorative material launched, *Br Dent J* 195(9) (2003) 525-525.
- [16] Biomaterials for tissue regeneration, *Br Dent J* 220(11) (2016) 607-607.

- [17] R. Bettach, B. Guillaume, S. Taschieri, M. Del Fabbro, Clinical Performance of a Highly Porous Beta-TCP as the Grafting Material for Maxillary Sinus Augmentation, *Implant Dent* 23(3) (2014) 357-364.
- [18] P. Gao, H.Q. Zhang, Y. Liu, B. Fan, X.K. Li, X. Xiao, P.H. Lan, M.H. Li, L. Geng, D. Liu, Y.L. Yuan, Q. Lian, J.X. Lu, Z. Guo, Z. Wang, Beta-tricalcium phosphate granules improve osteogenesis in vitro and establish innovative osteo-regenerators for bone tissue engineering in vivo, *Sci Rep-Uk* 6 (2016).
- [19] H.D. Kim, H.L. Jang, H.Y. Ahn, H.K. Lee, J. Park, E.S. Lee, E.A. Lee, Y.H. Jeong, D.G. Kim, K.T. Nam, N.S. Hwang, Biomimetic whitlockite inorganic nanoparticles-mediated in situ remodeling and rapid bone regeneration, *Biomaterials* 112 (2017) 31-43.
- [20] H.L. Jang, G.B. Zheng, J. Park, H.D. Kim, H.R. Baek, H.K. Lee, K. Lee, H.N. Han, C.K. Lee, N.S. Hwang, J.H. Lee, K.T. Nam, In Vitro and In Vivo Evaluation of Whitlockite Biocompatibility: Comparative Study with Hydroxyapatite and beta-Tricalcium Phosphate, *Adv Healthc Mater* 5(1) (2016) 128-36.

- [21] R. Gmeiner, U. Deisinger, J. Schonherr, B. Lechner, R. Detsch, A.R. Boccaccini, J. Stampfl, Additive Manufacturing of Bioactive Glasses and Silicate Bioceramics, *J Ceram Sci Technol* 6(2) (2015) 75-86.
- [22] X.D. Zhang, D.L. Zeng, N. Li, J. Wen, X.Q. Jiang, C.S. Liu, Y.S. Li, Functionalized mesoporous bioactive glass scaffolds for enhanced bone tissue regeneration, *Sci Rep-Uk* 6 (2016).
- [23] H. Kim, R.P. Camata, Y.K. Vohra, W.R. Lacefield, Control of phase composition in hydroxyapatite/tetracalcium phosphate biphasic thin coatings for biomedical applications, *J Mater Sci Mater Med* 16(10) (2005) 961-6.
- [24] T. Kitsugi, T. Yamamuro, T. Nakamura, M. Oka, Transmission electron microscopy observations at the interface of bone and four types of calcium phosphate ceramics with different calcium/phosphorus molar ratios, *Biomaterials* 16(14) (1995) 1101-7.
- [25] C. Niedhart, U. Maus, E. Redmann, C.H. Siebert, In vivo testing of a new in situ setting beta-tricalcium phosphate cement for osseous reconstruction, *Journal of biomedical materials research* 55(4) (2001) 530-7.

- [26] H.H. Horch, R. Sader, C. Pautke, A. Neff, H. Deppe, A. Kolk, Synthetic, pure-phase beta-tricalcium phosphate ceramic granules (Cerasorb) for bone regeneration in the reconstructive surgery of the jaws, *Int J Oral Maxillofac Surg* 35(8) (2006) 708-13.
- [27] A. Ogose, T. Hotta, H. Kawashima, N. Kondo, W. Gu, T. Kamura, N. Endo, Comparison of hydroxyapatite and beta tricalcium phosphate as bone substitutes after excision of bone tumors, *J Biomed Mater Res B Appl Biomater* 72(1) (2005) 94-101.
- [28] P. Ducheyne, S. Radin, L. King, The effect of calcium phosphate ceramic composition and structure on in vitro behavior. I. Dissolution, *J Biomed Mater Res* 27(1) (1993) 25-34.
- [29] G. Daculsi, R.Z. LeGeros, E. Nery, K. Lynch, B. Kerebel, Transformation of biphasic calcium phosphate ceramics in vivo: ultrastructural and physicochemical characterization, *J Biomed Mater Res* 23(8) (1989) 883-94.
- [30] G. Daculsi, Biphasic calcium phosphate concept applied to artificial bone, implant coating and injectable bone substitute, *Biomaterials* 19(16) (1998) 1473-8.

- [31] M. Neo, T. Nakamura, C. Ohtsuki, T. Kokubo, T. Yamamuro, Apatite Formation on 3 Kinds of Bioactive Material at an Early-Stage in-Vivo - a Comparative-Study by Transmission Electron-Microscopy, *J Biomed Mater Res* 27(8) (1993) 999-1006.
- [32] N. Kotobuki, D. Kawagoe, D. Nomura, Y. Katou, K. Muraki, H. Fujimori, S. Goto, K. Ioku, H. Ohgushi, Observation and quantitative analysis of rat bone marrow stromal cells cultured in vitro on newly formed transparent beta-tricalcium phosphate, *J Mater Sci Mater Med* 17(1) (2006) 33-41.
- [33] M.R. Urist, O. Nilsson, J. Rasmussen, W. Hirota, T. Lovell, T. Schmalzreid, G.A. Finerman, Bone regeneration under the influence of a bone morphogenetic protein (BMP) beta tricalcium phosphate (TCP) composite in skull trephine defects in dogs, *Clin Orthop Relat Res* (214) (1987) 295-304.
- [34] H. Yokozeki, T. Hayashi, T. Nakagawa, H. Kurosawa, K. Shibuya, K. Ioku, Influence of surface microstructure on the reaction of the active ceramics in vivo, *J Mater Sci Mater Med* 9(7) (1998) 381-4.

- [35] M. Kamitakahara, C. Ohtsuki, T. Miyazaki, Review Paper: Behavior of Ceramic Biomaterials Derived from Tricalcium Phosphate in Physiological Condition, *J Biomater Appl* 23(3) (2008) 197-212.
- [36] G. Daculsi, R.Z. LeGeros, A. Jean, B. Kerebel, Possible physico-chemical processes in human dentin caries, *Journal of dental research* 66(8) (1987) 1356-9.
- [37] C.A. Scotchford, M. Vickers, S.Y. Ali, The isolation and characterization of magnesium whitlockite crystals from human articular cartilage, *Osteoarthritis and cartilage / OARS, Osteoarthritis Research Society* 3(2) (1995) 79-94.
- [38] Y. Hayashi, High-Resolution Electron Microscopy of Mineral Deposits on a Thin Layer of Pellicle Adhering to Intact Enamel Surface, *Journal of electron microscopy* 45(6) (1996) 501-504.
- [39] J. Palamara, P.P. Phakey, W.A. Rachinger, H.J. Orams, Electron microscopy of surface enamel of human unerupted and erupted teeth, *Archives of oral biology* 25(11-12) (1980) 715-25.
- [40] J.C. Elliott, Structure and chemistry of the apatites and other calcium orthophosphates, Elsevier, Amsterdam New York ;, 1994.

- [41] P.T. Cheng, J.J. Grabher, R.Z. Legeros, Effects of Magnesium on Calcium-Phosphate Formation, *Magnesium* 7(3) (1988) 123-132.
- [42] H.L. Jang, K. Jin, J. Lee, Y. Kim, S.H. Nahm, K.S. Hong, K.T. Nam, Revisiting whitlockite, the second most abundant biomineral in bone: nanocrystal synthesis in physiologically relevant conditions and biocompatibility evaluation, *ACS Nano* 8(1) (2014) 634-41.
- [43] H.L. Jang, G.B. Zheng, J. Park, H.D. Kim, H.R. Baek, H.K. Lee, K. Lee, H.N. Han, C.K. Lee, N.S. Hwang, J.H. Lee, K.T. Nam, In Vitro and In Vivo Evaluation of Whitlockite Biocompatibility: Comparative Study with Hydroxyapatite and beta-Tricalcium Phosphate, *Advanced healthcare materials* (2015).
- [44] A. Piattelli, A. Scarano, M. Piattelli, F. Coraggio, S. Matarasso, Bone regeneration using Bioglass: an experimental study in rabbit tibia, *The Journal of oral implantology* 26(4) (2000) 257-61.
- [45] J. Yang, T. Long, N.-F. He, Y.-P. Guo, Z.-A. Zhu, Q.-F. Ke, Fabrication of a chitosan/bioglass three-dimensional porous scaffold for bone tissue engineering applications, *J. Mater. Chem. B* 2(38) (2014) 6611-6618.

- [46] J.R. Jones, Review of bioactive glass: from Hench to hybrids, *Acta Biomater* 9(1) (2013) 4457-86.
- [47] L.L. Hench, The story of Bioglass, *J Mater Sci Mater Med* 17(11) (2006) 967-78.
- [48] G. Piotrowski, L.L. Hench, W.C. Allen, G.J. Miller, Mechanical studies of the bone bioglass interfacial bond, *J Biomed Mater Res* 9(4) (1975) 47-61.
- [49] R. Hill, An alternative view of the degradation of bioglass, *J Mater Sci Lett* 15(13) (1996) 1122-1125.
- [50] M.R. Filgueiras, G. Latorre, L.L. Hench, Solution Effects on the Surface-Reactions of a Bioactive Glass, *J Biomed Mater Res* 27(4) (1993) 445-453.
- [51] H. Pirayesh, J.A. Nychka, Sol-Gel Synthesis of Bioactive Glass-Ceramic 45S5 and its in vitro Dissolution and Mineralization Behavior, *J Am Ceram Soc* 96(5) (2013) 1643-1650.
- [52] R. Li, A.E. Clark, L.L. Hench, An investigation of bioactive glass powders by sol-gel processing, *J Appl Biomater* 2(4) (1991) 231-9.

- [53] C. Stahli, M. James-Bhasin, A. Hoppe, A.R. Boccaccini, S.N. Nazhat, Effect of ion release from Cu-doped 45S5 Bioglass(R) on 3D endothelial cell morphogenesis, *Acta Biomater* 19 (2015) 15-22.
- [54] J. Isaac, J. Nohra, J. Lao, E. Jallot, J.M. Nedelec, A. Berdal, J.M. Sautier, Effects of strontium-doped bioactive glass on the differentiation of cultured osteogenic cells, *Eur Cell Mater* 21 (2011) 130-43.
- [55] W.C. Vrouwenvelder, C.G. Groot, K. de Groot, Better histology and biochemistry for osteoblasts cultured on titanium-doped bioactive glass: bioglass 45S5 compared with iron-, titanium-, fluorine- and boron-containing bioactive glasses, *Biomaterials* 15(2) (1994) 97-106.
- [56] A.A. Gorustovich, J.M. Lopez, M.B. Guglielmotti, R.L. Cabrini, Biological performance of boron-modified bioactive glass particles implanted in rat tibia bone marrow, *Biomed Mater* 1(3) (2006) 100-5.
- [57] E.M. Erbe, T.D. Clineff, C.S. Bagga, G.M. Nagvajara, A. Koblish, Biocompatible bone graft material, Google Patents, 2007.
- [58] E.M. Erbe, J.G. Marx, T.D. Clineff, L.D. Bellincampi, Potential of an ultraporous beta-tricalcium phosphate synthetic cancellous bone void filler and bone marrow aspirate composite graft, *European spine journal* : official publication of the European Spine Society, the European Spinal

Deformity Society, and the European Section of the Cervical Spine Research Society 10 Suppl 2 (2001) S141-6.

[59] N.S. Hwang, S. Varghese, H.J. Lee, Z. Zhang, J. Elisseeff, Biomaterials directed in vivo osteogenic differentiation of mesenchymal cells derived from human embryonic stem cells, Tissue engineering. Part A 19(15-16) (2013) 1723-32.

[60] I.G. Kim, M.P. Hwang, P. Du, J. Ko, C.W. Ha, S.H. Do, K. Park, Bioactive cell-derived matrices combined with polymer mesh scaffold for osteogenesis and bone healing, Biomaterials 50 (2015) 75-86.

[61] T.J.N. Smith, H. Jason, P. Sydney, S. Reginald, Porous ceramic composite bone grafts, Google Patents, 2011.

[62] S. Langstaff, M. Sayer, T.J. Smith, S.M. Pugh, Resorbable bioceramics based on stabilized calcium phosphates. Part II: evaluation of biological response, Biomaterials 22(2) (2001) 135-50.

[63] S. Langstaff, M. Sayer, T.J. Smith, S.M. Pugh, S.A. Hesp, W.T. Thompson, Resorbable bioceramics based on stabilized calcium phosphates. Part I: rational design, sample preparation and material characterization, Biomaterials 20(18) (1999) 1727-41.

- [64] J. Nyemscek, V. Kunjachan, A. Adams, Bioactive Bone Graft Substitutes, Google Patents, 2013.
- [65] M. Kikuchi, S. Itoh, S. Ichinose, K. Shinomiya, J. Tanaka, Self-organization mechanism in a bone-like hydroxyapatite/collagen nanocomposite synthesized in vitro and its biological reaction in vivo, *Biomaterials* 22(13) (2001) 1705-11.
- [66] S. Levenberg, N.F. Huang, E. Lavik, A.B. Rogers, J. Itskovitz-Eldor, R. Langer, Differentiation of human embryonic stem cells on three-dimensional polymer scaffolds, *Proceedings of the National Academy of Sciences of the United States of America* 100(22) (2003) 12741-6.
- [67] H. Yoshimoto, Y.M. Shin, H. Terai, J.P. Vacanti, A biodegradable nanofiber scaffold by electrospinning and its potential for bone tissue engineering, *Biomaterials* 24(12) (2003) 2077-82.
- [68] Z. Shao, X. Zhang, Y. Pi, L. Yin, L. Li, H. Chen, C. Zhou, Y. Ao, Surface modification on polycaprolactone electrospun mesh and human decalcified bone scaffold with synovium-derived mesenchymal stem cells-affinity peptide for tissue engineering, *Journal of biomedical materials research. Part A* 103(1) (2015) 318-29.

- [69] M. Yazdimamaghani, M. Razavi, D. Vashae, L. Tayebi, Surface modification of biodegradable porous Mg bone scaffold using polycaprolactone/bioactive glass composite, *Materials science & engineering. C, Materials for biological applications* 49 (2015) 436-44.
- [70] M.M. Villa, L. Wang, J. Huang, D.W. Rowe, M. Wei, Bone tissue engineering with a collagen-hydroxyapatite scaffold and culture expanded bone marrow stromal cells, *Journal of biomedical materials research. Part B, Applied biomaterials* 103(2) (2015) 243-53.
- [71] Y. Li, R. Joao, H. Tomas, Injectable and biodegradable hydrogels : gelation , biodegradation and, *Chem Soc Rev* 41 (2012) 2193-2221.
- [72] A. Sivashanmugam, R. Arun Kumar, M. Vishnu Priya, S.V. Nair, R. Jayakumar, An overview of injectable polymeric hydrogels for tissue engineering, *European Polymer Journal* 72 (2015) 543-565.
- [73] A.M. Rosales, K.S. Anseth, The design of reversible hydrogels to capture extracellular matrix dynamics, *Nature Reviews Materials* 1 (2016) 15012.
- [74] A.J. Engler, S. Sen, H.L. Sweeney, D.E. Discher, Matrix Elasticity Directs Stem Cell Lineage Specification, *Cell* 126 (2006) 677-689.

- [75] J.J. Green, J.H. Elisseeff, Mimicking biological functionality with polymers for biomedical applications, *Nature* 540 (2016) 386-394.
- [76] M. Guvendiren, H.D. Lu, J.A. Burdick, I.C. Kwon, S.Y. Jeong, T. Ooya, W.K. Lee, S. Sasaki, N. Yui, R.J. Schwartz, L. Wei, C. Zoja, G. Remuzzi, Shear-thinning hydrogels for biomedical applications, *Soft Matter* 8 (2012) 260-272.
- [77] M. Liu, X. Zeng, C. Ma, H. Yi, Z. Ali, X. Mou, S. Li, Y. Deng, N. He, Injectable hydrogels for cartilage and bone tissue engineering, *Bone Research* 5 (2017) 17014.
- [78] J.A. Yang, J. Yeom, B.W. Hwang, A.S. Hoffman, S.K. Hahn, In situ-forming injectable hydrogels for regenerative medicine, *Progress in Polymer Science* 39 (2014) 1973-1986.
- [79] R.K. Avery, H. Albadawi, M. Akbari, Y.S. Zhang, M.J. Duggan, D.V. Sahani, B.D. Olsen, A. Khademhosseini, R. Oklu, An injectable shear-thinning biomaterial for endovascular embolization, *Science Translational Medicine* 8 (2016) 365ra156 LP - 365ra156.
- [80] B.D. Olsen, J.A. Kornfield, D.A. Tirrell, Yielding behavior in injectable hydrogels from telechelic proteins, *Macromolecules* 43 (2010) 9094-9099.

- [81] M. Dessi, A. Borzacchiello, T.H.A. Mohamed, W.I. Abdel-Fattah, L. Ambrosio, Novel biomimetic thermosensitive  $\beta$ -tricalcium phosphate/chitosan-based hydrogels for bone tissue engineering, *Journal of Biomedical Materials Research - Part A* 101 (2013) 2984-2993.
- [82] S. Dhivya, S. Saravanan, T.P. Sastry, N. Selvamurugan, Nanohydroxyapatite-reinforced chitosan composite hydrogel for bone tissue repair in vitro and in vivo., *Journal of nanobiotechnology* 13 (2015) 40.
- [83] J.A. Burdick, K.S. Anseth, Photoencapsulation of osteoblasts in injectable RGD-modified PEG hydrogels for bone tissue engineering, *Biomaterials* 23 (2002) 4315-4323.
- [84] S. Fu, P. Ni, B. Wang, B. Chu, L. Zheng, F. Luo, J. Luo, Z. Qian, Injectable and thermo-sensitive PEG-PCL-PEG copolymer/collagen/n-HA hydrogel composite for guided bone regeneration, *Biomaterials* 33 (2012) 4801-4809.
- [85] A.A. Thorpe, S. Creasey, C. Sammon, C.L. Le Maitre, Hydroxyapatite nanoparticle injectable hydrogel scaffold to support osteogenic differentiation of human mesenchymal stem cells, *European Cells and Materials* 32 (2016) 1-23.

- [86] C. Xie, D. Reynolds, H. Awad, P.T. Rubery, G. Pelled, D. Gazit, R.E. Guldberg, E.M. Schwarz, R.J. O'Keefe, X. Zhang, Structural bone allograft combined with genetically engineered mesenchymal stem cells as a novel platform for bone tissue engineering., *Tissue engineering* 13 (2007) 435-45.
- [87] E. Davies, K.H. Müller, W.C. Wong, C.J. Pickard, D.G. Reid, J.N. Skepper, M.J. Duer, Citrate bridges between mineral platelets in bone., *Proceedings of the National Academy of Sciences of the United States of America* 111 (2014) E1354-63.
- [88] P.J. Kondiah, Y.E. Choonara, P.P.D. Kondiah, T. Marimuthu, P. Kumar, L.C. Du Toit, V. Pillay, A review of injectable polymeric hydrogel systems for application in bone tissue engineering, *Molecules* 21 (2016).
- [89] D. Dyondi, T.J. Webster, R. Banerjee, A nanoparticulate injectable hydrogel as a tissue engineering scaffold for multiple growth factor delivery for bone regeneration, *International Journal of Nanomedicine* 8 (2012) 47-59.
- [90] Y.M. Kolambkar, K.M. Dupont, J.D. Boerckel, N. Huebsch, D.J. Mooney, D.W. Hutmacher, R.E. Guldberg, An alginate-based hybrid

system for growth factor delivery in the functional repair of large bone defects, *Biomaterials* 32 (2011) 65-74.

[91] T.N. Vo, F.K. Kasper, A.G. Mikos, Strategies for controlled delivery of growth factors and cells for bone regeneration, *Advanced Drug Delivery Reviews* 64 (2012) 1292-1309.

[92] D. Suárez-González, J.S. Lee, A. Diggs, Y. Lu, B. Nemke, M. Markel, S.J. Hollister, W.L. Murphy, Controlled multiple growth factor delivery from bone tissue engineering scaffolds via designed affinity., *Tissue engineering. Part A* 20 (2014) 2077-87.

[93] G. Hulsart-Billström, Q. Hu, K. Bergman, K.B. Jonsson, J. Åberg, R. Tang, S. Larsson, J. Hilborn, Calcium phosphates compounds in conjunction with hydrogel as carrier for BMP-2: A study on ectopic bone formation in rats, *Acta Biomaterialia* 7 (2011) 3042-3049.

[94] R.E. Jung, F.E. Weber, D.S. Thoma, M. Ehrbar, D.L. Cochran, C.H.F. Hämmerle, Bone morphogenetic protein-2 enhances bone formation when delivered by a synthetic matrix containing hydroxyapatite/tricalciumphosphate, *Clinical Oral Implants Research* 19 (2008) 188-195.

- [95] P. Hänseler, U.W. Jung, R.E. Jung, K.H. Choi, K.S. Cho, C.H.F. Hämmerle, F.E. Weber, Analysis of hydrolyzable polyethylene glycol hydrogels and deproteinized bone mineral as delivery systems for glycosylated and non-glycosylated bone morphogenetic protein-2, *Acta Biomaterialia* 8 (2012) 116-123.
- [96] A.-C. Docherty-Skogh, K. Bergman, M.J. Waern, S. Ekman, K. Hultenby, D. Ossipov, J. Hilborn, T. Bowden, T. Engstrand, Bone morphogenetic protein-2 delivered by hyaluronan-based hydrogel induces massive bone formation and healing of cranial defects in minipigs., *Plastic and reconstructive surgery* 125 (2010) 1383-92.
- [97] G.A. Silva, C. Czeisler, K.L. Niece, E. Beniash, D.A. Harrington, J.A. Kessler, S.I. Stupp, Selective Differentiation of Neural Progenitor Cells by High – Epitope Density Nanofibers, *Science* 303 (2004) 1352-1355.
- [98] H. Wang, O.C. Boerman, K. Sariibrahimoglu, Y. Li, J.A. Jansen, S.C.G. Leeuwenburgh, Comparison of micro- vs. nanostructured colloidal gelatin gels for sustained delivery of osteogenic proteins: Bone morphogenetic protein-2 and alkaline phosphatase, *Biomaterials* 33 (2012) 8695-8703.

- [99] R. Arun Kumar, A. Sivashanmugam, S. Deepthi, S. Iseki, K.P. Chennazhi, S.V. Nair, R. Jayakumar, Injectable chitin-poly( $\epsilon$ -caprolactone)/nanohydroxyapatite composite microgels prepared by simple regeneration technique for bone tissue engineering, *ACS Applied Materials and Interfaces*, 2015, pp. 9399-9409.
- [100] V.W. van Hinsbergh, a. Collen, P. Koolwijk, Role of fibrin matrix in angiogenesis., *Annals of the New York Academy of Sciences* 936 (2001) 426-437.
- [101] E. Hadjipanayi, P.H. Kuhn, P. Moog, A.T. Bauer, H. Kuekrek, L. Mirzoyan, A. Hummel, K. Kirchhoff, B. Salgin, S. Isenburg, U. Dornseifer, M. Ninkovic, H.G. Machens, A.F. Schilling, The fibrin matrix regulates angiogenic responses within the hemostatic microenvironment through biochemical control, *PLoS ONE* 10 (2015) 1-20.
- [102] Y.I. Yang, D.L. Seol, H.I. Kim, M.H. Cho, S.J. Lee, Composite fibrin and collagen scaffold to enhance tissue regeneration and angiogenesis, *Current Applied Physics* 7 (2007) 103-107.
- [103] R. Arun Kumar, A. Sivashanmugam, S. Deepthi, J.D. Bumgardner, S.V. Nair, R. Jayakumar, Nano-fibrin stabilized CaSO<sub>4</sub> crystals

incorporated injectable chitin composite hydrogel for enhanced angiogenesis & osteogenesis, *Carbohydrate Polymers* 140 (2016) 144-153.

[104] M.V. Priya, A. Sivshanmugam, A.R. Boccaccini, O.M. Goudouri, W. Sun, N. Hwang, Y. Lin, W. Xiao, X. Liu, B.S. Bal, L.F. Bonewald, M.N. Rahaman, J.M. Kanczler, R.O.C. Oreffo, Injectable osteogenic and angiogenic nanocomposite hydrogels for irregular bone defects, *Biomedical Materials* 035017 (2016) 35017.

[105] S.C. Dennis, J. Whitlow, M.S. Detamore, S.L. Kieweg, C.J. Berkland, Hyaluronic-Acid-Hydroxyapatite Colloidal Gels Combined with Micronized Native ECM as Potential Bone Defect Fillers, *Langmuir* 33 (2017) 206-218.

[106] A.K. Miri, N. Muja, N.O. Kamranpour, W.C. Lepry, A.R. Boccaccini, S.A. Clarke, S.N. Nazhat, Ectopic bone formation in rapidly fabricated acellular injectable dense collagen-Bioglass hybrid scaffolds via gel aspiration-ejection, *Biomaterials* 85 (2016) 128-141.

[107] J. Ma, M. Thompson, N. Zhao, D. Zhu, Similarities and differences in coatings for magnesium-based stents and orthopaedic implants, *J Orthop Translat* 2(3) (2014) 118-130.

- [108] S. Yoshizawa, A. Brown, A. Barchowsky, C. Sfeir, Role of magnesium ions on osteogenic response in bone marrow stromal cells, *Connect Tissue Res* 55 Suppl 1 (2014) 155-9.
- [109] Y.F. Zhang, J.K. Xu, Y.C. Ruan, M.K. Yu, M. O'Laughlin, H. Wise, D. Chen, L. Tian, D.F. Shi, J.L. Wang, S.H. Chen, J.Q. Feng, D.H.K. Chow, X.H. Xie, L.Z. Zheng, L. Huang, S. Huang, K. Leung, N. Lu, L. Zhao, H.F. Li, D.W. Zhao, X. Guo, K.M. Chan, F. Witte, H.C. Chan, Y.F. Zheng, L. Qin, Implant-derived magnesium induces local neuronal production of CGRP to improve bone-fracture healing in rats, *Nat Med* 22(10) (2016) 1160-1169.
- [110] Y. Kuboki, H. Takita, D. Kobayashi, E. Tsuruga, M. Inoue, M. Murata, N. Nagai, Y. Dohi, H. Ohgushi, BMP-Induced osteogenesis on the surface of hydroxyapatite with geometrically feasible and nonfeasible structures: Topology of osteogenesis, *Journal of Biomedical Materials Research Part A* 39 (1998) 190-199.
- [111] A.R. Amini, D.J. Adams, C.T. Laurencin, S.P. Nukavarapu, Optimally porous and biomechanically compatible scaffolds for large-area bone regeneration, *Tissue engineering. Part A* 18(13-14) (2012) 1376-88.

- [112] M.Q. Cheng, T. Wahafu, G.F. Jiang, W. Liu, Y.Q. Qiao, X.C. Peng, T. Cheng, X.L. Zhang, G. He, X.Y. Liu, A novel open-porous magnesium scaffold with controllable microstructures and properties for bone regeneration, *Scientific reports* 6 (2016) 24134.
- [113] G. Hannink, J.J. Arts, Bioresorbability, porosity and mechanical strength of bone substitutes: what is optimal for bone regeneration?, *Injury* 42 Suppl 2 (2011) S22-5.
- [114] X. Xiao, W. Wang, D. Liu, H. Zhang, P. Gao, L. Geng, Y. Yuan, J. Lu, Z. Wang, The promotion of angiogenesis induced by three-dimensional porous beta-tricalcium phosphate scaffold with different interconnection sizes via activation of PI3K/Akt pathways, *Scientific reports* 5(1) (2015).
- [115] M. Mastrogiacomo, S. Scaglione, R. Martinetti, L. Dolcini, F. Beltrame, R. Cancedda, R. Quarto, Role of scaffold internal structure on in vivo bone formation in macroporous calcium phosphate bioceramics, *Biomaterials* 27(17) (2006) 3230-7.
- [116] N. Thadavirul, P. Pavasant, P. Supaphol, Development of polycaprolactone porous scaffolds by combining solvent casting, particulate leaching, and polymer leaching techniques for bone tissue

engineering, *Journal of Biomedical Materials Research Part A* 102(10) (2014) 3379-3392.

[117] B. Nasri-Nasrabadi, M. Mehrasa, M. Rafienia, S. Bonakdar, T. Behzad, S. Gavanji, Porous starch/cellulose nanofibers composite prepared by salt leaching technique for tissue engineering, *Carbohydrate polymers* 108 (2014) 232-8.

[118] S.A. Poursamar, J. Hatami, A.N. Lehner, C.L. da Silva, F.C. Ferreira, A.P. Antunes, Gelatin porous scaffolds fabricated using a modified gas foaming technique: characterisation and cytotoxicity assessment, *Materials science & engineering. C, Materials for biological applications* 48 (2015) 63-70.

[119] B.-Y. Chen, X. Jing, H.-Y. Mi, H. Zhao, W.-H. Zhang, X.-F. Peng, L.-S. Turng, Fabrication of polylactic acid/polyethylene glycol (PLA/PEG) porous scaffold by supercritical CO<sub>2</sub>foaming and particle leaching, *Polymer Engineering & Science* 55(6) (2015) 1339-1348.

[120] S. Pina, J.M. Oliveira, R.L. Reis, Natural-based nanocomposites for bone tissue engineering and regenerative medicine: a review, *Advanced materials* 27(7) (2015) 1143-69.

- [121] R. Nazarov, H.J. Jin, D.L. Kaplan, Porous 3-D scaffolds from regenerated silk fibroin, *Biomacromolecules* 5(3) (2004) 718-26.
- [122] Y.S. Nam, J.J. Yoon, T.G. Park, A novel fabrication method of macroporous biodegradable polymer scaffolds using gas foaming salt as a porogen additive, *Journal of biomedical materials research* 53(1) (2000) 1-7.
- [123] F.J. Martinez-Vazquez, M.V. Cabanas, J.L. Paris, D. Lozano, M. Vallet-Regi, Fabrication of novel Si-doped hydroxyapatite/gelatin scaffolds by rapid prototyping for drug delivery and bone regeneration, *Acta biomaterialia* 15 (2015) 200-9.
- [124] K.S. Kang, S.I. Lee, J.M. Hong, J.W. Lee, H.Y. Cho, J.H. Son, S.H. Paek, D.W. Cho, Hybrid scaffold composed of hydrogel/3D-framework and its application as a dopamine delivery system, *J Control Release* 175 (2014) 10-6.
- [125] W.-c. Lee, C.-c. Wei, S.-C. Chung, Development of a hybrid rapid prototyping system using low-cost fused deposition modeling and five-axis machining, *Journal of Materials Processing Technology* 214(11) (2014) 2366-2374.

- [126] S. Bustamante, S. Bose, P. Bishop, R. Klatte, F. Norris, Novel application of rapid prototyping for simulation of bronchoscopic anatomy, *Journal of cardiothoracic and vascular anesthesia* 28(4) (2014) 1122-5.
- [127] C.B. Highley, C.B. Rodell, J.A. Burdick, Direct 3D Printing of Shear-Thinning Hydrogels into Self-Healing Hydrogels, *Advanced materials* 27(34) (2015) 5075-9.
- [128] A.E. Jakus, A.L. Rutz, S.W. Jordan, A. Kannan, S.M. Mitchell, C. Yun, K.D. Koube, S.C. Yoo, H.E. Whiteley, C.P. Richter, R.D. Galiano, W.K. Hsu, S.R. Stock, E.L. Hsu, R.N. Shah, Hyperelastic "bone": A highly versatile, growth factor-free, osteoregenerative, scalable, and surgically friendly biomaterial, *Sci Transl Med* 8(358) (2016) 358ra127.
- [129] M. Floren, S. Spilimbergo, A. Motta, C. Migliaresi, Porous poly(D,L-lactic acid) foams with tunable structure and mechanical anisotropy prepared by supercritical carbon dioxide, *J Biomed Mater Res B Appl Biomater* 99(2) (2011) 338-49.
- [130] B.C. Gross, J.L. Erkal, S.Y. Lockwood, C. Chen, D.M. Spence, Evaluation of 3D printing and its potential impact on biotechnology and the chemical sciences, *Analytical chemistry* 86(7) (2014) 3240-53.

- [131] J.S. Miller, K.R. Stevens, M.T. Yang, B.M. Baker, D.-H.T. Nguyen, D.M. Cohen, E. Toro, A.a. Chen, P.a. Galie, X. Yu, R. Chaturvedi, S.N. Bhatia, C.S. Chen, Rapid casting of patterned vascular networks for perfusable engineered three-dimensional tissues, *Nature Materials* 11 (2012) 768-774.
- [132] A. Kantaros, N. Chatzidai, D. Karalekas, 3D printing-assisted design of scaffold structures, *The International Journal of Advanced Manufacturing Technology* (2015).
- [133] C.T. Kao, C.C. Lin, Y.W. Chen, C.H. Yeh, H.Y. Fang, M.Y. Shie, Poly(dopamine) coating of 3D printed poly(lactic acid) scaffolds for bone tissue engineering, *Materials science & engineering. C, Materials for biological applications* 56 (2015) 165-73.
- [134] C.H. Chen, M.Y. Lee, V.B. Shyu, Y.C. Chen, C.T. Chen, J.P. Chen, Surface modification of polycaprolactone scaffolds fabricated via selective laser sintering for cartilage tissue engineering, *Materials science & engineering. C, Materials for biological applications* 40 (2014) 389-97.

- [135] S.K. Tiwari, S. Pande, S. Agrawal, S.M. Bobade, Selection of selective laser sintering materials for different applications, *Rapid Prototyping Journal* 21(6) (2015) 630-648.
- [136] E.O. Olakanmi, R.F. Cochrane, K.W. Dalgarno, A review on selective laser sintering/melting (SLS/SLM) of aluminium alloy powders: Processing, microstructure, and properties, *Progress in Materials Science* 74 (2015) 401-477.
- [137] A. Mazzoli, C. Ferretti, A. Gigante, E. Salvolini, M. Mattioli-Belmonte, Selective laser sintering manufacturing of polycaprolactone bone scaffolds for applications in bone tissue engineering, *Rapid Prototyping Journal* 21(4) (2015) 386-392.
- [138] Y. Du, H. Liu, J. Shuang, J. Wang, J. Ma, S. Zhang, Microsphere-based selective laser sintering for building macroporous bone scaffolds with controlled microstructure and excellent biocompatibility, *Colloids and surfaces. B, Biointerfaces* 135 (2015) 81-89.
- [139] I. Zein, D.W. Hutmacher, K.C. Tan, S.H. Teoh, Fused deposition modeling of novel scaffold architectures for tissue engineering applications, *Biomaterials* 23(4) (2002) 1169-85.

- [140] F. Ning, W. Cong, J. Qiu, J. Wei, S. Wang, Additive manufacturing of carbon fiber reinforced thermoplastic composites using fused deposition modeling, *Composites Part B: Engineering* 80 (2015) 369-378.
- [141] S.J. Kalita, S. Bose, H.L. Hosick, A. Bandyopadhyay, Development of controlled porosity polymer-ceramic composite scaffolds via fused deposition modeling, *Materials Science and Engineering: C* 23(5) (2003) 611-620.
- [142] J. Chen, C. Peng, J. Nie, J.F. Kennedy, G. Ma, Lyophilization as a novel approach for preparation of water resistant HA fiber membranes by crosslinked with EDC, *Carbohydrate polymers* 102 (2014) 8-11.
- [143] T.R. Cuadros, A.A. Erices, J.M. Aguilera, Porous matrix of calcium alginate/gelatin with enhanced properties as scaffold for cell culture, *Journal of the mechanical behavior of biomedical materials* 46 (2015) 331-42.
- [144] H.W. Kim, J.C. Knowles, H.E. Kim, Hydroxyapatite and gelatin composite foams processed via novel freeze-drying and crosslinking for use as temporary hard tissue scaffolds, *Journal of biomedical materials research. Part A* 72(2) (2005) 136-45.

- [145] B. Sun, Y.Z. Long, H.D. Zhang, M.M. Li, J.L. Duvail, X.Y. Jiang, H.L. Yin, Advances in three-dimensional nanofibrous macrostructures via electrospinning, *Progress in Polymer Science* 39(5) (2014) 862-890.
- [146] M.K. Joshi, H.R. Pant, A.P. Tiwari, H.J. kim, C.H. Park, C.S. Kim, Multi-layered macroporous three-dimensional nanofibrous scaffold via a novel gas foaming technique, *Chemical Engineering Journal* 275 (2015) 79-88.
- [147] D.Z. Yang, A.Z. Chen, S.B. Wang, Y. Li, X.L. Tang, Y.J. Wu, Preparation of poly(L-lactic acid) nanofiber scaffolds with a rough surface by phase inversion using supercritical carbon dioxide, *Biomedical materials* 10(3) (2015) 035015.
- [148] E.J. Chong, T.T. Phan, I.J. Lim, Y.Z. Zhang, B.H. Bay, S. Ramakrishna, C.T. Lim, Evaluation of electrospun PCL/gelatin nanofibrous scaffold for wound healing and layered dermal reconstitution, *Acta biomaterialia* 3(3) (2007) 321-30.
- [149] S.W.a.L. Addadi, Design strategies in mineralized biological materials, *Journal Material Chemistry* 7(5) (1997) 689-702.
- [150] A.L. Boskey, Biomineralization: An Overview, *Connective Tissue Research* 44(1) (2009) 5-9.

- [151] M.T.a.T. Matsuda, Surface functional group dependence on apatite formation on self-assembled monolayers in a simulated body fluid, *Journal of Biomedical Materials Research* 34 (1997) 305-315.
- [152] D.S. Benoit, M.P. Schwartz, A.R. Durney, K.S. Anseth, Small functional groups for controlled differentiation of hydrogel-encapsulated human mesenchymal stem cells, *Nat Mater* 7(10) (2008) 816-23.
- [153] S. Deepthi, K.T. Shalumon, K.P. Chennazhi, D. Menon, R. Jayakumar, Surface plasma treatment of poly(caprolactone) micro, nano, and multiscale fibrous scaffolds for enhanced osteoconductivity, *Tissue Eng Part A* 20(11-12) (2014) 1689-702.
- [154] H.D. Kim, E.A. Lee, Y.H. An, S.L. Kim, S.S. Lee, S.J. Yu, H.L. Jang, K.T. Nam, S.G. Im, N.S. Hwang, Chondroitin Sulfate-Based Biomaterializing Surface Hydrogels for Bone Tissue Engineering, *ACS Appl Mater Interfaces* 9(26) (2017) 21639-21650.
- [155] A.M. Phillips, Overview of the fracture healing cascade, *Injury* 36 Suppl 3 (2005) S5-7.
- [156] R. Dimitriou, E. Tsiridis, P.V. Giannoudis, Current concepts of molecular aspects of bone healing, *Injury* 36(12) (2005) 1392-404.

- [157] T.A. Einhorn, L.C. Gerstenfeld, Fracture healing: mechanisms and interventions, *Nature Reviews Rheumatology* 11(1) (2014) 45-54.
- [158] H. Lu, R. Landesberg, J. Vo, R. Tsay, H.I. Peng, Growth factor encapsulation system for enhancing bone formation, Google Patents, 2006.
- [159] M.N. Woszczyzna, A.A. Biswas, C.A. Cogswell, D.J. Goldhamer, Multipotent progenitors resident in the skeletal muscle interstitium exhibit robust BMP-dependent osteogenic activity and mediate heterotopic ossification, *Journal of bone and mineral research : the official journal of the American Society for Bone and Mineral Research* 27(5) (2012) 1004-17.
- [160] K. Miyazawa, M. Shinozaki, T. Hara, T. Furuya, K. Miyazono, Two major Smad pathways in TGF-beta superfamily signalling, *Genes to cells : devoted to molecular & cellular mechanisms* 7(12) (2002) 1191-204.
- [161] Y. Fujimori, T. Nakamura, S. Ijiri, K. Shimizu, T. Yamamuro, Heterotopic bone formation induced by bone morphogenetic protein in mice with collagen-induced arthritis, *Biochemical and biophysical research communications* 186(3) (1992) 1362-7.

- [162] M.E. Oest, K.M. Dupont, H.J. Kong, D.J. Mooney, R.E. Guldborg, Quantitative assessment of scaffold and growth factor-mediated repair of critically sized bone defects, *Journal of orthopaedic research : official publication of the Orthopaedic Research Society* 25(7) (2007) 941-50.
- [163] T. Yoshida, H. Miyaji, K. Otani, K. Inoue, K. Nakane, H. Nishimura, A. Ibara, A. Shimada, K. Ogawa, E. Nishida, T. Sugaya, L. Sun, B. Fugetsu, M. Kawanami, Bone augmentation using a highly porous PLGA/beta-TCP scaffold containing fibroblast growth factor-2, *Journal of periodontal research* 50(2) (2015) 265-73.
- [164] M. Dadsetan, T. Guda, M.B. Runge, D. Mijares, R.Z. LeGeros, J.P. LeGeros, D.T. Silliman, L. Lu, J.C. Wenke, P.R. Brown Baer, M.J. Yaszemski, Effect of calcium phosphate coating and rhBMP-2 on bone regeneration in rabbit calvaria using poly(propylene fumarate) scaffolds, *Acta biomaterialia* 18 (2015) 9-20.
- [165] S. Suliman, Z. Xing, X. Wu, Y. Xue, T.O. Pedersen, Y. Sun, A.P. Døskeland, J. Nickel, T. Waag, H. Lygre, A. Finne-Wistrand, D. Steinmüller-Nethl, A. Krueger, K. Mustafa, Release and bioactivity of bone morphogenetic protein-2 are affected by scaffold binding

techniques in vitro and in vivo, *Journal of controlled release : official journal of the Controlled Release Society* 197 (2015) 148-57.

[166] N.S. Hwang, S. Varghese, J. Elisseeff, Controlled differentiation of stem cells, *Adv Drug Deliver Rev* 60(2) (2008) 199-214.

[167] R. Subbiah, M.P. Hwang, S.Y. Van, S.H. Do, H. Park, K. Lee, S.H. Kim, K. Yun, K. Park, Osteogenic/angiogenic dual growth factor delivery microcapsules for regeneration of vascularized bone tissue, *Adv Healthc Mater* 4(13) (2015) 1982-92.

[168] L. Cao, J. Wang, J. Hou, W. Xing, C. Liu, Vascularization and bone regeneration in a critical sized defect using 2-N,6-O-sulfated chitosan nanoparticles incorporating BMP-2, *Biomaterials* 35(2) (2014) 684-98.

[169] J.Y. Park, J.-H. Shim, S.-A. Choi, J. Jang, M. Kim, S.H. Lee, D.-W. Cho, 3D printing technology to control BMP-2 and VEGF delivery spatially and temporally to promote large-volume bone regeneration, *J. Mater. Chem. B* 3(27) (2015) 5415-5425.

[170] D.H. Kempen, L. Lu, A. Heijink, T.E. Hefferan, L.B. Creemers, A. Maran, M.J. Yaszemski, W.J. Dhert, Effect of local sequential VEGF and BMP-2 delivery on ectopic and orthotopic bone regeneration, *Biomaterials* 30(14) (2009) 2816-25.

- [171] Simon Young, Zarana S. Patel, James D. Kretlow, Matthew B. Murphy, Paschalia M. Mountziaris, H.U. L. Scott Baggett, Yasuhiko Tabata, John A. Jansen, Mark Wong, A.G. Mikos., Dose Effect of Dual Delivery of Vascular Endothelial Growth Factor and Bone Morphogenetic Protein-2 on Bone Regeneration in a Rat Critical-Size Defect Model, *Tissue Engineering Part A* 15(9) (2009) 2347-2362.
- [172] Z.S. Patel, S. Young, Y. Tabata, J.A. Jansen, M.E. Wong, A.G. Mikos, Dual delivery of an angiogenic and an osteogenic growth factor for bone regeneration in a critical size defect model, *Bone* 43(5) (2008) 931-40.
- [173] I.A. Rodriguez, E.A. Growney Kalaf, G.L. Bowlin, S.A. Sell, Platelet-rich plasma in bone regeneration: engineering the delivery for improved clinical efficacy, *BioMed research international* 2014 (2014) 392398.
- [174] C.A. Heath, Cells for tissue engineering, *Trends in biotechnology* 18(1) (2000) 17-9.
- [175] K.G. Sylvester, M.T. Longaker, Stem cells: review and update, *Arch Surg* 139(1) (2004) 93-9.

- [176] A.I. Caplan, Mesenchymal stem cells, *Journal of orthopaedic research : official publication of the Orthopaedic Research Society* 9(5) (1991) 641-50.
- [177] A.J. Friedenstein, J.F. Gorskaja, N.N. Kulagina, Fibroblast precursors in normal and irradiated mouse hematopoietic organs, *Exp Hematol* 4(5) (1976) 267-74.
- [178] E.J. Caterson, L.J. Nesti, K.G. Danielson, R.S. Tuan, Human marrow-derived mesenchymal progenitor cells: isolation, culture expansion, and analysis of differentiation, *Mol Biotechnol* 20(3) (2002) 245-56.
- [179] S. Gronthos, A.C. Zannettino, S.J. Hay, S. Shi, S.E. Graves, A. Kortesidis, P.J. Simmons, Molecular and cellular characterisation of highly purified stromal stem cells derived from human bone marrow, *J Cell Sci* 116(Pt 9) (2003) 1827-35.
- [180] G.O. Stewart, D.H. Gutteridge, R.I. Price, L. Ward, R.W. Retallack, R.L. Prince, B.G. Stuckey, G.N. Kent, C.I. Bhagat, S.S. Dhaliwal, Prevention of appendicular bone loss in Paget's disease following treatment with intravenous pamidronate disodium, *Bone* 24(2) (1999) 139-44.

- [181] S.P. Bruder, N.S. Ricalton, R.E. Boynton, T.J. Connolly, N. Jaiswal, J. Zaia, F.P. Barry, Mesenchymal stem cell surface antigen SB-10 corresponds to activated leukocyte cell adhesion molecule and is involved in osteogenic differentiation, *J Bone Miner Res* 13(4) (1998) 655-63.
- [182] M. Dominici, K. Le Blanc, I. Mueller, I. Slaper-Cortenbach, F. Marini, D. Krause, R. Deans, A. Keating, D. Prockop, E. Horwitz, Minimal criteria for defining multipotent mesenchymal stromal cells. The International Society for Cellular Therapy position statement, *Cytotherapy* 8(4) (2006) 315-7.
- [183] M.F. Pittenger, A.M. Mackay, S.C. Beck, R.K. Jaiswal, R. Douglas, J.D. Mosca, M.A. Moorman, D.W. Simonetti, S. Craig, D.R. Marshak, Multilineage potential of adult human mesenchymal stem cells, *Science* 284(5411) (1999) 143-7.
- [184] S.P. Bruder, N. Jaiswal, S.E. Haynesworth, Growth kinetics, self-renewal, and the osteogenic potential of purified human mesenchymal stem cells during extensive subcultivation and following cryopreservation, *Journal of cellular biochemistry* 64(2) (1997) 278-94.

- [185] C.G. Bellows, J.N. Heersche, J.E. Aubin, Determination of the capacity for proliferation and differentiation of osteoprogenitor cells in the presence and absence of dexamethasone, *Dev Biol* 140(1) (1990) 132-8.
- [186] C.G. Bellows, J.E. Aubin, J.N. Heersche, Initiation and progression of mineralization of bone nodules formed in vitro: the role of alkaline phosphatase and organic phosphate, *Bone Miner* 14(1) (1991) 27-40.
- [187] M.J. Coelho, M.H. Fernandes, Human bone cell cultures in biocompatibility testing. Part II: effect of ascorbic acid, beta-glycerophosphate and dexamethasone on osteoblastic differentiation, *Biomaterials* 21(11) (2000) 1095-102.
- [188] R.T. Franceschi, The role of ascorbic acid in mesenchymal differentiation, *Nutr Rev* 50(3) (1992) 65-70.
- [189] R. Hata, H. Senoo, L-ascorbic acid 2-phosphate stimulates collagen accumulation, cell proliferation, and formation of a three-dimensional tissuelike substance by skin fibroblasts, *Journal of cellular physiology* 138(1) (1989) 8-16.

- [190] Z. Huang, E.R. Nelson, R.L. Smith, S.B. Goodman, The sequential expression profiles of growth factors from osteoprogenitors [correction of osteoprogenitors] to osteoblasts in vitro, *Tissue Eng* 13(9) (2007) 2311-20.
- [191] M. Centrella, T.L. McCarthy, E. Canalis, Transforming growth factor beta is a bifunctional regulator of replication and collagen synthesis in osteoblast-enriched cell cultures from fetal rat bone, *The Journal of biological chemistry* 262(6) (1987) 2869-74.
- [192] M. Ishii, J. Kikuta, Y. Shimazu, M. Meier-Schellersheim, R.N. Germain, Chemorepulsion by blood S1P regulates osteoclast precursor mobilization and bone remodeling in vivo, *J Exp Med* 207(13) (2010) 2793-8.
- [193] N.A. Sims, T.J. Martin, Coupling the activities of bone formation and resorption: a multitude of signals within the basic multicellular unit, *BoneKEy Rep* 3 (2014).
- [194] S.L. Teitelbaum, Bone resorption by osteoclasts, *Science* 289(5484) (2000) 1504-8.
- [195] V. Everts, W. Korper, K.A. Hoeben, I.D. Jansen, D. Bromme, K.B. Cleutjens, S. Heeneman, C. Peters, T. Reinheckel, P. Saftig, W. Beertsen,

Osteoclastic bone degradation and the role of different cysteine proteinases and matrix metalloproteinases: differences between calvaria and long bone, *J Bone Miner Res* 21(9) (2006) 1399-408.

[196] L. Xian, X. Wu, L. Pang, M. Lou, C.J. Rosen, T. Qiu, J. Crane, F. Frassica, L. Zhang, J.P. Rodriguez, J. Xiaofeng, Y. Shoshana, X. Shouhong, E. Argiris, W. Mei, C. Xu, Matrix IGF-1 maintains bone mass by activation of mTOR in mesenchymal stem cells, *Nat Med* 18(7) (2012) 1095-101.

[197] E.C. Walker, N.E. McGregor, I.J. Poulton, S. Pompolo, E.H. Allan, J.M. Quinn, M.T. Gillespie, T.J. Martin, N.A. Sims, Cardiotrophin-1 is an osteoclast-derived stimulus of bone formation required for normal bone remodeling, *J Bone Miner Res* 23(12) (2008) 2025-32.

[198] Y. Tang, X. Wu, W. Lei, L. Pang, C. Wan, Z. Shi, L. Zhao, T.R. Nagy, X. Peng, J. Hu, X. Feng, W. Van Hul, M. Wan, X. Cao, TGF-beta1-induced migration of bone mesenchymal stem cells couples bone resorption with formation, *Nat Med* 15(7) (2009) 757-65.

[199] E.J. Mackie, Osteoblasts: novel roles in orchestration of skeletal architecture, *Int J Biochem Cell Biol* 35(9) (2003) 1301-5.

- [200] H.C. Blair, S.L. Teitelbaum, R. Ghiselli, S. Gluck, Osteoclastic bone resorption by a polarized vacuolar proton pump, *Science* 245(4920) (1989) 855-7.
- [201] I. Silver, R. Murrills, D. Etherington, Microelectrode studies on the acid microenvironment beneath adherent macrophages and osteoclasts, *Experimental cell research* 175(2) (1988) 266-276.
- [202] P. Saftig, E. Hunziker, O. Wehmeyer, S. Jones, A. Boyde, W. Rommerskirch, J.D. Moritz, P. Schu, K. von Figura, Impaired osteoclastic bone resorption leads to osteopetrosis in cathepsin-K-deficient mice, *Proc Natl Acad Sci U S A* 95(23) (1998) 13453-8.
- [203] M. Gowen, F. Lazner, R. Dodds, R. Kapadia, J. Feild, M. Tavarria, I. Bertonecello, F. Drake, S. Zavarsek, I. Tellis, P. Hertzog, C. Debouck, I. Kola, Cathepsin K knockout mice develop osteopetrosis due to a deficit in matrix degradation but not demineralization, *J Bone Miner Res* 14(10) (1999) 1654-63.
- [204] F.C. Driessens, R. Verbeeck, *Biominerals*, CRC Press 1990.
- [205] H.L. Jang, K. Jin, J. Lee, Y. Kim, S.H. Nahm, K.S. Hong, K.T. Nam, Revisiting Whitlockite, the Second Most Abundant Biomineral in

Bone: Nanocrystal Synthesis in Physiologically Relevant Conditions and Biocompatibility Evaluation, ACS nano 8(1) (2013) 634-641.

[206] R. Gopal, C. Calvo, Structural relationship of whitlockite and  $\beta\text{Ca}_3(\text{PO}_4)_2$ , Nature 237(71) (1972) 30-32.

[207] D. Meinke, H. Skinner, K. Thomson, X-ray diffraction of the calcified tissues in *Polypterus*, Calcified tissue international 28(1) (1979) 37-42.

[208] P. Quint, J. Althoff, H. Höhling, A. Boyde, W. Laabs, Characteristic molar ratios of magnesium, carbon dioxide, calcium and phosphorus in the mineralizing fracture callus and pre-dentine, Calcified tissue international 32(1) (1980) 257-261.

[209] D. Briggs, M. Seah, H. Bubern, Practical Surface Analysis. Vol. 1: Auger and X-ray Photoelectron Spectroscopy, Angewandte Chemie-German Edition 107(11) (1995) 1367-1367.

[210] W. Kaminsky, From CIF to virtual morphology using the WinXMorph program, J Appl Crystallogr 40 (2007) 382-385.

[211] W. Kaminsky, WinXMorph: a computer program to draw crystal morphology, growth sectors and cross sections with export files in

VRML V2.0 utf8-virtual reality format, J Appl Crystallogr 38 (2005) 566-567.

[212] C. Calvo, R. Gopal, Crystal-Structure of Whitlockite from Palermo Quarry, Am Mineral 60(1-2) (1975) 120-133.

[213] L.S. KAPLOW, A histochemical procedure for localizing and evaluating leukocyte alkaline phosphatase activity in smears of blood and marrow, Blood 10(10) (1955) 1023-1029.

[214] G. Ackerman, Substituted naphthol AS phosphate derivatives for the localization of leukocyte alkaline phosphatase activity, Laboratory investigation; a journal of technical methods and pathology 11 (1962) 563-567.

[215] K.J. Livak, T.D. Schmittgen, Analysis of relative gene expression data using real-time quantitative PCR and the  $2^{-\Delta\Delta CT}$  method, methods 25(4) (2001) 402-408.

[216] S.J. Bryant, K.S. Anseth, Hydrogel properties influence ECM production by chondrocytes photoencapsulated in poly (ethylene glycol) hydrogels, Journal of biomedical materials research 59(1) (2002) 63-72.

[217] C. Frondel, Whitlockite a new calcium phosphate,  $\text{Ca}_3(\text{PO}_4)_2$ , Am Mineral 26(3) (1941) 145-152.

- [218] M. Sarikaya, C. Tamerler, A.K. Jen, K. Schulten, F. Baneyx, Molecular biomimetics: nanotechnology through biology, *Nat Mater* 2(9) (2003) 577-85.
- [219] T.A. Taton, Nanotechnology. Boning up on biology, *Nature* 412(6846) (2001) 491-2.
- [220] I. Gitlin, J.D. Carbeck, G.M. Whitesides, Why are proteins charged? Networks of charge–charge interactions in proteins measured by charge ladders and capillary electrophoresis, *Angewandte Chemie International Edition* 45(19) (2006) 3022-3060.
- [221] M. Lund, T. Åkesson, B. Jönsson, Enhanced protein adsorption due to charge regulation, *Langmuir* 21(18) (2005) 8385-8388.
- [222] L.M. Rodriguez-Lorenzo, M. Vallet-Regi, J.M. Ferreira, Colloidal processing of hydroxyapatite, *Biomaterials* 22(13) (2001) 1847-52.
- [223] C.R. Kothapalli, M. Wei, M.T. Shaw, Solvent-specific gel-like transition via complexation of polyelectrolyte and hydroxyapatite nanoparticles suspended in water-glycerin mixtures: a rheological study, *Soft Matter* 4(3) (2008) 600-605.
- [224] M.A. Rothschild, M. Oratz, S.S. Schreiber, Serum albumin, *Hepatology* 8(2) (1988) 385-401.

- [225] T. Peters, The biosynthesis of rat serum albumin I. Properties of rat albumin and its occurrence in liver cell fractions, *Journal of Biological Chemistry* 237(4) (1962) 1181-1185.
- [226] Y. Jin, W. Zhang, Y. Liu, M. Zhang, L. Xu, Q. Wu, X. Zhang, Z. Zhu, Q. Huang, X. Jiang, rhPDGF-BB Via ERK Pathway Osteogenesis and Adipogenesis Balancing in ADSCs for Critical-Sized Calvarial Defect Repair, *Tissue Engineering Part A* 20(23-24) (2014) 3303-3313.
- [227] S. Yoshizawa, A. Brown, A. Barchowsky, C. Sfeir, Role of magnesium ions on osteogenic response in bone marrow stromal cells, *Connective tissue research* 55(S1) (2014) 155-159.
- [228] Y.-R.V. Shih, Y. Hwang, A. Phadke, H. Kang, N.S. Hwang, E.J. Caro, S. Nguyen, M. Siu, E.A. Theodorakis, N.C. Gianneschi, Calcium phosphate-bearing matrices induce osteogenic differentiation of stem cells through adenosine signaling, *Proceedings of the National Academy of Sciences* 111(3) (2014) 990-995.
- [229] A. Ikari, K. Atomi, K. Kinjo, Y. Sasaki, J. Sugatani, Magnesium deprivation inhibits a MEK–ERK cascade and cell proliferation in renal epithelial Madin-Darby canine kidney cells, *Life sciences* 86(19) (2010) 766-773.

- [230] H. Kang, Y.-R.V. Shih, S. Varghese, Biomaterialized matrices dominate soluble cues to direct osteogenic differentiation of human mesenchymal stem cells through adenosine signaling, *Biomacromolecules* (2015).
- [231] S. Patntirapong, P. Habibovic, P.V. Hauschka, Effects of soluble cobalt and cobalt incorporated into calcium phosphate layers on osteoclast differentiation and activation, *Biomaterials* 30(4) (2009) 548-555.
- [232] J. Kanehisa, J.N. Heersche, Osteoclastic bone resorption: in vitro analysis of the rate of resorption and migration of individual osteoclasts, *Bone* 9(2) (1988) 73-9.
- [233] M. Ohgaki, T. Kizuki, M. Katsura, K. Yamashita, Manipulation of selective cell adhesion and growth by surface charges of electrically polarized hydroxyapatite, *Journal of biomedical materials research* 57(3) (2001) 366-373.
- [234] H.L. Jang, H.K. Lee, K. Jin, H.-Y. Ahn, H.-E. Lee, K.T. Nam, Phase transformation from hydroxyapatite to the secondary bone mineral, whitlockite, *Journal of Materials Chemistry B* (2014).

- [235] P. Habibovic, J.E. Barralet, *Bioinorganics and biomaterials: bone repair*, *Acta Biomater* 7(8) (2011) 3013-26.
- [236] J.C. Le Huec, D. Clement, B. Brouillaud, N. Barthe, B. Dupuy, B. Foliguet, B. Basse-Cathalinat, *Evolution of the local calcium content around irradiated beta-tricalcium phosphate ceramic implants: in vivo study in the rabbit*, *Biomaterials* 19(7-9) (1998) 733-8.
- [237] M.P. Staiger, A.M. Pietak, J. Huadmai, G. Dias, *Magnesium and its alloys as orthopedic biomaterials: A review*, *Biomaterials* 27(9) (2006) 1728-1734.
- [238] D. Kumar, J.P. Gittings, I.G. Turner, C.R. Bowen, A. Bastida-Hidalgo, S.H. Cartmell, *Polarization of hydroxyapatite: Influence on osteoblast cell proliferation*, *Acta Biomaterialia* 6(4) (2010) 1549-1554.
- [239] S. Nakamura, T. Kobayashi, K. Yamashita, *Numerical osteobonding evaluation of electrically polarized hydroxyapatite ceramics*, *J Biomed Mater Res A* 68(1) (2004) 90-4.
- [240] S. Itoh, S. Nakamura, T. Kobayashi, K. Shinomiya, K. Yamashita, S. Itoh, *Effect of electrical polarization of hydroxyapatite ceramics on new bone formation*, *Calcif Tissue Int* 78(3) (2006) 133-42.

[241] P. Calvert, S. Mann, Crystallography - The negative side of crystal growth, *Nature* 386(6621) (1997) 127-&.

[242] M. Park, Y.H. Kim, S.Y. Woo, H.J. Lee, Y. Yu, H.S. Kim, Y.S. Park, I. Jo, J.W. Park, S.C. Jung, H. Lee, B. Jeong, K.H. Ryu, Tonsil-derived Mesenchymal Stem Cells Ameliorate CCl4-induced Liver Fibrosis in Mice via Autophagy Activation, *Sci Rep-Uk* 5 (2015).

[243] Y.S. Lim, J.C. Lee, Y.S. Lee, B.J. Lee, S.G. Wang, Growth Inhibitory Effect of Palatine Tonsil-derived Mesenchymal Stem Cells on Head and Neck Squamous Cell Carcinoma Cells, *Clin Exp Otorhinolar* 5(2) (2012) 86-93.

[244] R. Terpstra, F. Driessens, Magnesium in tooth enamel and synthetic apatites, *Calcified tissue international* 39(5) (1986) 348-354.

[245] F. Abbona, H.E.L. Madsen, R. Boistelle, The final phases of calcium and magnesium phosphates precipitated from solutions of high to medium concentration, *Journal of crystal growth* 89(4) (1988) 592-602.

[246] F. Tamimi, D. Le Nihouannen, D.C. Bassett, S. Ibasco, U. Gbureck, J. Knowles, A. Wright, A. Flynn, S.V. Komarova, J.E. Barralet, Biocompatibility of magnesium phosphate minerals and their stability

under physiological conditions, *Acta biomaterialia* 7(6) (2011) 2678-2685.

[247] R.A. Hartvig, M. van de Weert, J. Østergaard, L. Jorgensen, H. Jensen, Formation of dielectric layers and charge regulation in protein adsorption at biomimetic interfaces, *Langmuir* 28(3) (2012) 1804-1815.

[248] R.A. Hartvig, M. van de Weert, J. Østergaard, L. Jorgensen, H. Jensen, Protein adsorption at charged surfaces: the role of electrostatic interactions and interfacial charge regulation, *Langmuir* 27(6) (2011) 2634-2643.

[249] B. Levi, J.S. Hyun, D.T. Montoro, D.D. Lo, C.K. Chan, S. Hu, N. Sun, M. Lee, M. Grova, A.J. Connolly, J.C. Wu, G.C. Gurtner, I.L. Weissman, D.C. Wan, M.T. Longaker, In vivo directed differentiation of pluripotent stem cells for skeletal regeneration, *Proc Natl Acad Sci U S A* 109(50) (2012) 20379-84.

[250] M. Moazen, E. Peskett, C. Babbs, E. Pauws, M.J. Fagan, Mechanical Properties of Calvarial Bones in a Mouse Model for Craniosynostosis, *Plos One* 10(5) (2015).

- [251] R. Lagier, C.A. Baud, Magnesium whitlockite, a calcium phosphate crystal of special interest in pathology, *Pathol Res Pract* 199(5) (2003) 329-335.
- [252] P. Muller, U. Bulnheim, A. Diener, F. Luthen, M. Teller, E.D. Klinkenberg, H.G. Neumann, B. Nebe, A. Liebold, G. Steinhoff, J. Rychly, Calcium phosphate surfaces promote osteogenic differentiation of mesenchymal stem cells, *J Cell Mol Med* 12(1) (2008) 281-291.
- [253] Y.R.V. Shih, Y. Hwang, A. Phadke, H. Kang, N.S. Hwang, E.J. Caro, S. Nguyen, M. Siu, E.A. Theodorakis, N.C. Gianneschi, K.S. Vecchio, S. Chien, O.K. Lee, S. Varghese, Calcium phosphate-bearing matrices induce osteogenic differentiation of stem cells through adenosine signaling, *P Natl Acad Sci USA* 111(3) (2014) 990-995.
- [254] S. Boonrungsiman, E. Gentleman, R. Carzaniga, N.D. Evans, D.W. McComb, A.E. Porter, M.M. Stevens, The role of intracellular calcium phosphate in osteoblast-mediated bone apatite formation, *P Natl Acad Sci USA* 109(35) (2012) 14170-14175.
- [255] S.H. Jun, E.J. Lee, T.S. Jang, H.E. Kim, J.H. Jang, Y.H. Koh, Bone morphogenic protein-2 (BMP-2) loaded hybrid coating on porous

hydroxyapatite scaffolds for bone tissue engineering, *J Mater Sci-Mater M* 24(3) (2013) 773-782.

[256] L. Xiang, D.C. Li, B.H. Lu, Y.P. Tang, L. Wang, Z. Wang, Design and fabrication of CAP scaffolds by indirect solid free form fabrication, *Rapid Prototyping Journal* 11(5) (2005) 312-318.

[257] S.H. Li, J.R. de Wijn, J.P. Li, P. Layrolle, K. de Groot, Macroporous biphasic calcium phosphate scaffold with high permeability/porosity ratio, *Tissue Eng* 9(3) (2003) 535-548.

[258] C.R. Nuttelman, D.S.W. Benoit, M.C. Tripodi, K.S. Anseth, The effect of ethylene glycol methacrylate phosphate in PEG hydrogels on mineralization and viability of encapsulated hMSCs, *Biomaterials* 27(8) (2006) 1377-1386.

[259] C.W. Kim, S.E. Kim, Y.W. Kim, H.J. Lee, H.W. Choi, J.H. Chang, J. Choi, K.J. Kim, K.B. Shim, Y.K. Jeong, S.C. Lee, Fabrication of hybrid composites based on biomineralization of phosphorylated poly(ethylene glycol) hydrogels, *J Mater Res* 24(1) (2009) 50-57.

[260] N. Specchia, A. Pagnotta, M. Cappella, A. Tampieri, F. Greco, Effect of hydroxyapatite porosity on growth and differentiation of human osteoblast-like cells, *J Mater Sci* 37(3) (2002) 577-584.

- [261] C.M. Stanford, M. Solursh, J.C. Keller, Significant role of adhesion properties of primary osteoblast-like cells in early adhesion events for chondroitin sulfate and dermatan sulfate surface molecules, *J Biomed Mater Res* 47(3) (1999) 345-352.
- [262] U. Hempel, C. Matthaus, C. Preissler, S. Moller, V. Hintze, P. Dieter, Artificial matrices with high-sulfated glycosaminoglycans and collagen are anti-inflammatory and pro-osteogenic for human mesenchymal stromal cells, *J Cell Biochem* 115(9) (2014) 1561-71.
- [263] S. Varghese, N.S. Hwang, A.C. Canver, P. Theprungsirikul, D.W. Lin, J. Elisseeff, Chondroitin sulfate based niches for chondrogenic differentiation of mesenchymal stem cells, *Matrix Biology* 27(1) (2008) 12-21.
- [264] T. Izumikawa, B. Sato, H. Kitagawa, Chondroitin Sulfate Is Indispensable for Pluripotency and Differentiation of Mouse Embryonic Stem Cells, *Sci Rep-Uk* 4 (2014).
- [265] H.K. Cheung, T.T.Y. Han, D.M. Marecak, J.F. Watkins, B.G. Amsden, L.E. Flynn, Composite hydrogel scaffolds incorporating decellularized adipose tissue for soft tissue engineering with adipose-derived stem cells, *Biomaterials* 35(6) (2014) 1914-1923.

- [266] W. Schneiders, C. Rentsch, S. Rehberg, S. Rein, H. Zwipp, S. Rammelt, Effect of chondroitin sulfate on osteogenetic differentiation of human mesenchymal stem cells, *Mat Sci Eng C-Mater* 32(7) (2012) 1926-1930.
- [267] J.J. Lim, J.S. Temenoff, The effect of desulfation of chondroitin sulfate on interactions with positively charged growth factors and upregulation of cartilaginous markers in encapsulated MSCs, *Biomaterials* 34(21) (2013) 5007-5018.
- [268] H.D. Kim, J. Heo, Y. Hwang, S.Y. Kwak, O.K. Park, H. Kim, S. Varghese, N.S. Hwang, Extracellular-matrix-based and Arg-Gly-Asp-modified photopolymerizing hydrogels for cartilage tissue engineering, *Tissue Eng Part A* 21(3-4) (2015) 757-66.
- [269] S.J. Bryant, K.S. Anseth, Hydrogel properties influence ECM production by chondrocytes photoencapsulated in poly(ethylene glycol) hydrogels, *J Biomed Mater Res* 59(1) (2002) 63-72.
- [270] U. Lindahl, M. Hook, Glycosaminoglycans and Their Binding to Biological Macromolecules, *Annual Review of Biochemistry* 47 (1978) 385-417.

- [271] F. Nudelman, K. Pieterse, A. George, P.H.H. Bomans, H. Friedrich, L.J. Brylka, P.A.J. Hilbers, G. de With, N.A.J.M. Sommerdijk, The role of collagen in bone apatite formation in the presence of hydroxyapatite nucleation inhibitors, *Nat Mater* 9(12) (2010) 1004-1009.
- [272] H.D. Kim, J. Heo, Y. Hwang, S.Y. Kwak, O.K. Park, H. Kim, S. Varghese, N.S. Hwang, Extracellular-Matrix-Based and Arg-Gly-Asp-Modified Photopolymerizing Hydrogels for Cartilage Tissue Engineering, *Tissue Eng Pt A* 21(3-4) (2015) 757-766.
- [273] G.M. Eichenbaum, P.F. Kiser, A.V. Dobrynin, S.A. Simon, D. Needham, Investigation of the swelling response and loading of ionic microgels with drugs and proteins: The dependence on cross-link density (vol 32, pg 4867, 1999), *Macromolecules* 34(18) (2001) 6526-6526.
- [274] C.T. Lee, P.H. Kung, Y.D. Lee, Preparation of poly(vinyl alcohol)-chondroitin sulfate hydrogel as matrices in tissue engineering, *Carbohydr Polym* 61(3) (2005) 348-354.
- [275] D.W. Urry, Neutral sites for calcium ion binding to elastin and collagen: a charge neutralization theory for calcification and its relationship to atherosclerosis, *Proc Natl Acad Sci U S A* 68(4) (1971) 810-4.

- [276] S.F. Hossainy, J.A. Hubbell, Molecular weight dependence of calcification of polyethylene glycol hydrogels, *Biomaterials* 15(11) (1994) 921-5.
- [277] D.A. Wang, C.G. Williams, F. Yang, N. Cher, H. Lee, J.H. Elisseeff, Bioresponsive phosphoester hydrogels for bone tissue engineering, *Tissue Eng* 11(1-2) (2005) 201-13.
- [278] S. Bentov, E.D. Aflalo, J. Tynyakov, L. Glazer, A. Sagi, Calcium phosphate mineralization is widely applied in crustacean mandibles, *Sci Rep-Uk* 6 (2016).
- [279] K. Gkioni, S.C.G. Leeuwenburgh, T.E.L. Douglas, A.G. Mikos, J.A. Jansen, Mineralization of Hydrogels for Bone Regeneration, *Tissue Eng Part B-Re* 16(6) (2010) 577-585.
- [280] T. Taguchi, A. Kishida, M. Akashi, Apatite formation on/in hydrogel matrices using an alternate soaking process: II. Effect of swelling ratios of poly(vinyl alcohol) hydrogel matrices on apatite formation, *J Biomat Sci-Polym E* 10(3) (1999) 331-339.
- [281] A. Oyane, M. Uchida, C. Choong, J. Triffitt, J. Jones, A. Ito, Simple surface modification of poly(epsilon-caprolactone) for apatite

deposition from simulated body fluid, *Biomaterials* 26(15) (2005) 2407-2413.

[282] P. Li, C. Ohtsuki, T. Kokubo, K. Nakanishi, N. Soga, T. Nakamura, T. Yamamuro, Process of Formation of Bone-Like Apatite Layer on Silica-Gel, *J Mater Sci-Mater M* 4(2) (1993) 127-131.

[283] T. Kokubo, F. Miyaji, H.M. Kim, T. Nakamura, Spontaneous formation of bonelike apatite layer on chemically treated titanium metals, *J Am Ceram Soc* 79(4) (1996) 1127-1129.

[284] T. Koike, T. Mikami, M. Shida, O. Habuchi, H. Kitagawa, Chondroitin sulfate-E mediates estrogen-induced osteoanabolism, *Sci Rep-Uk* 5 (2015).

[285] T. Koike, T. Izumikawa, J. Tamura, H. Kitagawa, Chondroitin sulfate-E fine-tunes osteoblast differentiation via ERK1/2, Smad3 and Smad1/5/8 signaling by binding to N-cadherin and cadherin-11, *Biochem Bioph Res Co* 420(3) (2012) 523-529.

[286] Q. Li, G. Zhou, X. Yu, T. Wang, Y. Xi, Z. Tang, Porous deproteinized bovine bone scaffold with three-dimensional localized drug delivery system using chitosan microspheres, *Biomedical engineering online* 14 (2015) 33.

- [287] D. Nadeem, C.A. Smith, M.J. Dalby, R.M. Meek, S. Lin, G. Li, B. Su, Three-dimensional CaP/gelatin lattice scaffolds with integrated osteoinductive surface topographies for bone tissue engineering, *Biofabrication* 7(1) (2015) 015005.
- [288] M. Kucharska, K. Walenko, M. Lewandowska-Szumiel, T. Brynk, J. Jaroszewicz, T. Ciach, Chitosan and composite microsphere-based scaffold for bone tissue engineering: evaluation of tricalcium phosphate content influence on physical and biological properties, *Journal of materials science. Materials in medicine* 26(3) (2015) 143.
- [289] S. Minardi, B. Corradetti, F. Taraballi, M. Sandri, J. Van Eps, F.J. Cabrera, B.K. Weiner, A. Tampieri, E. Tasciotti, Evaluation of the osteoinductive potential of a bio-inspired scaffold mimicking the osteogenic niche for bone augmentation, *Biomaterials* 62 (2015) 128-37.
- [290] C.M. Curtin, E.G. Tierney, K. McSorley, S.A. Cryan, G.P. Duffy, F.J. O'Brien, Combinatorial gene therapy accelerates bone regeneration: non-viral dual delivery of VEGF and BMP2 in a collagen-nanohydroxyapatite scaffold, *Advanced healthcare materials* 4(2) (2015) 223-7.

- [291] X. Xiao, W. Wang, D. Liu, H. Zhang, P. Gao, L. Geng, Y. Yuan, J. Lu, Z. Wang, The promotion of angiogenesis induced by three-dimensional porous beta-tricalcium phosphate scaffold with different interconnection sizes via activation of PI3K/Akt pathways, *Scientific reports* 5 (2015) 9409.
- [292] Z. Chen, X. Mao, L. Tan, T. Friis, C. Wu, R. Crawford, Y. Xiao, Osteoimmunomodulatory properties of magnesium scaffolds coated with beta-tricalcium phosphate, *Biomaterials* 35(30) (2014) 8553-65.
- [293] H.T. Liao, M.Y. Lee, W.W. Tsai, H.C. Wang, W.C. Lu, Osteogenesis of adipose-derived stem cells on polycaprolactone-beta-tricalcium phosphate scaffold fabricated via selective laser sintering and surface coating with collagen type I, *Journal of tissue engineering and regenerative medicine* (2013).
- [294] M. Wang, X. Cheng, W. Zhu, B. Holmes, M. Keidar, L.G. Zhang, Design of biomimetic and bioactive cold plasma-modified nanostructured scaffolds for enhanced osteogenic differentiation of bone marrow-derived mesenchymal stem cells, *Tissue engineering. Part A* 20(5-6) (2014) 1060-71.

- [295] H.Y. He, J.Y. Zhang, X. Mi, Y. Hu, X.Y. Gu, Rapid prototyping for tissue-engineered bone scaffold by 3D printing and biocompatibility study, *International journal of clinical and experimental medicine* 8(7) (2015) 11777-85.
- [296] H.J. Park, O.J. Lee, M.C. Lee, B.M. Moon, H.W. Ju, J. Lee, J.H. Kim, D.W. Kim, C.H. Park, Fabrication of 3D porous silk scaffolds by particulate (salt/sucrose) leaching for bone tissue reconstruction, *International journal of biological macromolecules* 78 (2015) 215-23.
- [297] P. Tesavibul, S. Chantaweroad, A. Laohaprapanon, S. Channasanon, P. Uppanan, S. Tanodekaew, P. Chalermkarnnon, K. Sitthiseripratip, Biocompatibility of hydroxyapatite scaffolds processed by lithography-based additive manufacturing, *Bio-medical materials and engineering* 26(1-2) (2015) 31-8.
- [298] J. Pasuri, J. Holopainen, H. Kokkonen, M. Persson, K. Kauppinen, P. Lehenkari, E. Santala, M. Ritala, J. Tuukkanen, Osteoclasts in the interface with electrospun hydroxyapatite, *Colloids and surfaces. B, Biointerfaces* 135 (2015) 774-783.
- [299] J. Yuan, B. Wang, C. Han, X. Lu, W. Sun, D. Wang, J. Lu, J. Zhao, C. Zhang, Y. Xie, In vitro comparison of three rifampicin loading

methods in a reinforced porous beta-tricalcium phosphate scaffold, *Journal of materials science. Materials in medicine* 26(4) (2015) 174.

[300] J. Yang, Y. Kang, C. Browne, T. Jiang, Y. Yang, Graded porous beta-tricalcium phosphate scaffolds enhance bone regeneration in mandible augmentation, *The Journal of craniofacial surgery* 26(2) (2015) e148-53.

[301] K.H. Ryu, K.A. Cho, H.S. Park, J.Y. Kim, S.Y. Woo, I. Jo, Y.H. Choi, Y.M. Park, S.C. Jung, S.M. Chung, B.O. Choi, H.S. Kim, Tonsil-derived mesenchymal stromal cells: evaluation of biologic, immunologic and genetic factors for successful banking, *Cytotherapy* 14(10) (2012) 1193-202.

[302] H. Ro, J. Park, K. Yang, J. Kim, H.G. Yim, G. Jung, H. Lee, S.W. Cho, N.S. Hwang, Osteogenic priming of mesenchymal stem cells by chondrocyte-conditioned factors and mineralized matrix, *Cell and tissue research* 362(1) (2015) 115-26.

[303] K. Joensuu, L. Uusitalo, J.J. Alm, H.T. Aro, T.A. Hentunen, T.J. Heino, Enhanced osteoblastic differentiation and bone formation in co-culture of human bone marrow mesenchymal stromal cells and peripheral blood mononuclear cells with exogenous VEGF,

Orthopaedics & traumatology, surgery & research : OTSR 101(3) (2015) 381-6.

[304] J.H. Lee, S. Um, J.H. Jang, B.M. Seo, Effects of VEGF and FGF-2 on proliferation and differentiation of human periodontal ligament stem cells, Cell and tissue research 348(3) (2012) 475-84.

[305] J.R. Garcia, A.J. Garcia, Biomaterial-mediated strategies targeting vascularization for bone repair, Drug delivery and translational research (2015).

[306] B. Behr, C. Tang, G. Germann, M.T. Longaker, N. Quarto, Locally applied vascular endothelial growth factor A increases the osteogenic healing capacity of human adipose-derived stem cells by promoting osteogenic and endothelial differentiation, Stem cells 29(2) (2011) 286-96.

[307] M. Lee, J. Keener, J. Xiao, X. Long Zheng, G.M. Rodgers, ADAMTS13 and its variants promote angiogenesis via upregulation of VEGF and VEGFR2, Cellular and molecular life sciences : CMLS 72(2) (2015) 349-56.

[308] X. Li, K. Gan, G. Song, C. Wang, VEGF gene transfected umbilical cord mesenchymal stem cells transplantation improve the

lower limb vascular lesions of diabetic rats, *Journal of diabetes and its complications* 29(7) (2015) 872-81.

[309] X. Jiang, Q. Xiong, G. Xu, H. Lin, X. Fang, D. Cui, M. Xu, F. Chen, H. Geng, VEGF-Loaded Nanoparticle-Modified BAMAs Enhance Angiogenesis and Inhibit Graft Shrinkage in Tissue-Engineered Bladder, *Annals of biomedical engineering* 43(10) (2015) 2577-86.

[310] K.J. Livak, T.D. Schmittgen, Analysis of relative gene expression data using real-time quantitative PCR and the  $2^{-\Delta\Delta C(T)}$  Method, *Methods* 25(4) (2001) 402-8.

[311] K. Maji, S. Dasgupta, B. Kundu, A. Bissoyi, Development of gelatin-chitosan-hydroxyapatite based bioactive bone scaffold with controlled pore size and mechanical strength, *Journal of biomaterials science. Polymer edition* 26(16) (2015) 1190-209.

[312] E. Tayton, M. Purcell, J.O. Smith, S. Lanham, S.M. Howdle, K.M. Shakesheff, A. Goodship, G. Blunn, D. Fowler, D.G. Dunlop, R.O. Oreffo, The scale-up of a tissue engineered porous hydroxyapatite polymer composite scaffold for use in bone repair: an ovine femoral condyle defect study, *Journal of biomedical materials research. Part A* 103(4) (2015) 1346-56.

[313] Lester L Smith, Paul J Niziolek, Karen M Haberstroh, E.A. Nauman, T.J. Webster, Decreased fibroblast and increased osteoblast adhesion on nanostructured NaOH-etched PLGA scaffolds, *International Journal of Nanomedicine* 2(3) (2007) 383-388.

[314] A. Thapa, D.C. Miller, T.J. Webster, K.M. Haberstroh, Nanostructured polymers enhance bladder smooth muscle cell function, *Biomaterials* 24(17) (2003) 2915-2926.

[315] N. Ferrara, H.P. Gerber, J. LeCouter, The biology of VEGF and its receptors, *Nature medicine* 9(6) (2003) 669-76.

요약(국문초록)

## 골 리모델링 및 급속 골 재생을 위한 Whitlockite

### 나노물질과 고분자 기반 생체모사 지지체에 관한 연구

생체 모사 지지체를 이용한 골 조직공학 한계점을 극복하기 위한 전 세계 연구자들의 노력이 계속 되고 있다. 이전부터 생체 모사 지지체는 인체 내에서 조직생성을 위한 줄기세포의 안정적인 정착과 분화에 크게 도움을 주는 플랫폼으로 인식 되어 왔다. 최근에 들어서는, 골 유도성을 증가 시키는 무기물질을 첨가하여 줄기세포의 골 재생에 적합한 미세환경을 만들어 주는 연구가 지속되고 있다. 또한 마이크로 사이즈의 구조를 가지는 지지체를 개발하여 성공적인 골 재생을 유도하는 연구도 더불어 발전하고 있다. 이러한 연구들의 연속으로, 지지체 개발의 많은 방법들이 개발되고 많은 연구자들이 시간을 투자해 왔다. 그 결과물로, 3D 프린팅과 같은 혁신적인 기술들을 사용하여 속주 줄기세포의

재료 투과성을 향상 시키고, 영양분의 공급을 용이하게 하며, 주변 환경에 혈관생성 과 세포 분화에 영향을 주는 방향으로 나아가고 있다. 이 논문의 첫 번째 챕터에서는 골 생체모사를 위한 재료 및 제작 방법에 대하여 소개하였다. 성공적인 골 재생을 위하여 많은 재료들이 최적화를 거쳐왔다. 생체친화적인 재료와, 생체분해 성이 용이한 고분자들이 골 형성을 위한 지지체의 기초 뼈대를 형성하고 골 유도 성을 위한 금속 이온들이나 단백질들을 이 지지체 뼈대 위에 증착 시킨다. 이것뿐만 아니라, 3 차원적 多공성 골 지지체의 구조물로 만들어 실제 뼈와 같은 형태를 유지하게 하는 연구가 진행 중이다. 전통적인 방법들은 계속 혁신을 겪어 왔고, 많은 세포 종류도 골 재생에 최적화 되어가고 있다. 이런 방법을 통하여 우리는 골 질환을 치료하는데 큰 도움을 줄 것이라고 예상된다.

이 논문의 두번째 챕터에서는 인공적으로 개발된 Whitlockite 나노입자를 이용하여 골재생의 초기단계에 개입하여 골 재생을 촉진 시키고 파골 세포의 활동을

중지시키며, 많은 양의 이온공급을 통한 무기물질의 재생을 도와주는 형태의 연구를 진행하였다. 게다가 많은 구조적 분석을 통하여 Whitlockite 나노입자가 Hydroxyapatite 형태로 상 변화를 일으킨다는 것을 밝혀 내고 이것이 빠른 골 재생에 주요한 메커니즘이라는 사실을 밝혀 내었다. 우리의 발견이 ‘살아있는 골 미네랄’을 이해하는 최초의 지식이 될 것이며 이것으로 말미암아 주변환경과 상호작용하는 세포와 재료의 관계를 이해하는 데에도 크게 도움이 될 것이라고 생각한다.

마지막 챕터에서는, 생체고분자인 콘드로이틴 황산의 전하를 이용하여 이온들의 바인딩과 증착을 유도, 재료의 미네랄화를 촉진시키는 실험을 진행하였다. 황산 그룹에 음성 전하가 칼슘과 포스페이트와 같은 이온들의 리쿠르팅을 발생시키고, 이 리쿠르팅 된 이온들에서부터 무기물질이 생성되며 미네랄화가 진행되는 것이다. 또한 콘드로이틴 황산에 의한 미네랄화는 줄기세포의 골분화를 촉진시키는 매개체로 사용된다. 이 생체고분자 기반의 하이드로겔

지지체는 생체 내에서도 골 재생을 유도하는 데에 큰 도움을 주었다.

본 논문에서 제시한 생체모사 기반의 지지체를 통한 골 리모델링과 급속적인 골 재생에 관한 연구는 자연계에 존재하는 무기물질이 여러 메커니즘을 통하여 세포간의 상호작용을 이해하는 데에 큰 도움이 되리라 본다. 그리고 앞으로 보다 생체 골과 유사한 재료를 구현하는 데 직접적으로 이바지 할 것으로 전망하며, 생체재료 분야 이외에도 다양한 연구 분야에 기반이 되리라 기대된다.\

**주요어: Hydrogel, Whitlockite, Hydroxyapatite, Chondroitin Sulfate, Bone Tissue Engineering**

**학번: 2014-31087**